1-1-2012

Fabrication Of Nanofibers Reinforced Polymer Microstructures Using Femtosecond Laser Material Processing

Mohammed-Amin Alubaidy
Ryerson University

FABRICATION OF NANOFIBERS REINFORCED POLYMER MICROSTRUCTURES USING FEMTOSECOND LASER MATERIAL PROCESSING

by

Mohammed-Amin Alubaidy

Master of Science, Mechanical Engineering

Alnahrain University, 1995

A dissertation

Presented to Ryerson University

in partial fulfillment of the requirement for the degree of

Doctor of Philosophy

in the program of

Mechanical Engineering

Toronto, Ontario, Canada

© Mohammed-Amin Alubaidy 2012

AUTHOR'S DECLARATION

AUTHOR'S DECLARATION FOR ELECTRONIC SUBMISSION OF A DISSERTATION

I hereby declare that I am the sole author of this dissertation. This is a true copy of the dissertation, including any required final revisions, as accepted by my examiners.

I authorize Ryerson University to lend this dissertation to other institutions or individuals for the purpose of scholarly research

I further authorize Ryerson University to reproduce this dissertation by photocopying or by other means, in total or in part, at the request of other institutions or individuals for the purpose of scholarly research.

I understand that my dissertation may be made electronically available to the public.

ABSTRACT

FABRICATION OF NANOFIBERS REINFORCED POLYMER MICROSTRUCTURES USING

FEMTOSECOND LASER MATERIAL PROCESSING

Doctor of Philosophy, 2012, Mohammed-Amin Alubaidy, Mechanical Engineering

Yeates School of Graduate Studies, Ryerson University

A new method has been introduced for the formation of microfeatures made of nanofibers reinforced polymer, using femtosecond laser material processing. The Femtosecond laser is used for the generation of three-dimensional interweaved nanofibers and the construction of microfeatures, like microchannels and voxels, through multi photon polymerization of nanofiber dispersed polymer resin. A new phenomenon of multiphoton polymerization induced by dual wavelength irradiation was reported for the first time. A significant improvement in the spatial resolution, compared to the two photon absorption (2PA) and the three photon absorption (3PA) processes has been achieved. Conductive polymer microstructures and magnetic polymer microstructures have been fabricated through this method. The mechanical properties of nanofiber reinforced polymer microstructures has been investigated by means of nanoindentation and the volume fraction of the generated nanofibers in the nanocomposite was calculated by using nanoindentation analysis. The results showed significant improvement in strength of the material. The electrical conductivity of the two photon polymerization (TPP) generated microfeatures was measured by a two-probe system at room temperature and the conductivity-temperature relationship was measured at a certain temperature range. The results suggest that the conductive polymer microstructure is reproducible and has a consistent conductivity-temperature relation. The magnetic strength has been characterized using Guassmeter. To

demonstrate the potential application of the new fabrication method, a novel class of DNA-functionalized three-dimensional (3D), stand-free, and nanostructured electrodes were fabricated. The developed nanofibrous DNA biosensor has been characterized by cyclic voltammetry with the use of ferrocyanide as an electrochemical redox indicator. Results showed that the probe–target recognition has been improved. This research demonstrated that femtosecond laser materials processing is a viable tool of the construction of naomaterial- reinforced polymer microfeatures with tailored properties.

PUBLICATIONS

REFEREED JOURNAL PUBLICATIONS

1. Alubaidy M., L. Soleymani, Venkatakrishnan K. and Tan B. (2012) femtosecond laser nanofibrous ultrasensitive biosensor for DNA direct detection, *Biosensors and Bioelectronics*, 33(1), pp. 82–87.

2. Alubaidy M., Venkatakrishnan K. and Tan B. (2011) Synthesis of magnetic nanofibers using femtosecond laser material processing in air, *Nanoscale Research Letters*, 6:375,

3. Alubaidy M., Venkatakrishnan K. and Tan B. (2011) On the formation of Titanium/Titanium oxide nanofiberous structures and nanospheres using femtosecond laser in air, *NANO*, Vol 6, issue 2.

4. Alubaidy M., Venkatakrishnan K. and Tan B. (2011) Fabrication of a reinforced polymer microstructure using femtosecond laser material processing. *Journal of Micromechanics and Microengineering*, Volume 20, Number 5.

5. Alubaidy M., Venkatakrishnan K. and Tan B. (2010) Femtosecond laser material processing of electrically conductive reinforced polymer, *Journal of Nanostructured Polymers and Nanocomposites*, 6/4 122-127,

6. Alubaidy M., Venkatakrishnan K. and Tan B. (2010) Mechanical Property Enhancement of Nanocomposite Microstructures Generated by Two Photon Polymerization. ASME, *Journal of Nanotechnology in Engineering and Medicine*, Volume 1, Issue 4, 041016.

7. Alubaidy M., Venkatakrishnan K. and Tan B. (2010) Nanofibers Plasmon enhancement of two photon polymerization induced by femtosecond laser. ASME, *Journal of Nanotechnology in Engineering and Medicine*, Volume 1, Issue 4, 041015.

CONFERENCE PRESENTATIONS

Alubaidy M., Venkatakrishnan K. and Tan B (2010) Synthesis of Titanium nafibers, nanospheres and nanodiscs using femtosecond laser material processing, International conference in Naostructured materials, International conference in Nanostructured materials *NANO 2010*, Italy, pp 225.

ACKNOWLEDGMENTS

I would like to thank my research supervisors Dr. K. Venkatakrishnan and Dr. Bo Tan, for their outstanding supervision and guidance. Their unconditional support, advice and constructive criticism throughout my research study have been invaluable. I would like to thank Dr. Ahmad Ghasempoor, Director of the Mechanical Engineering Graduate program, all the faculty members, the technical officers and the administrative staff members for their kind support and cooperation throughout all the time during my stay at Ryerson University. I am so grateful to the committee members, Dr. Ziad Saghir and Dr. Ravi Ravindran for their constructive comments and suggestions. I am also very grateful to my family for their continued support, prayers and love. My deepest gratitude to my parents who had to sacrifice their time and needs to support me in successfully finishing my studies. Finally, I would like to thank Mr. Robert Price for reviewing and proofreading my dissertation.

DEDICATION

The author hereby would like to dedicate this dissertation to his mother and the soul of

his father as a token of humble and sincere appreciation for their invaluable love and support.

TABLES OF CONTENTS

LIST OF TABLES

LIST OF FIGURES

xv

NOMENCLATURE

ps	picosecond (10^{-12} s)
fs	femtosecond (10^{-12} s)
μm	micrometer (10^{-6} m)
MHz	megahertz (10^{6-} Hz)
nm	nanometer (10^{-9} m)
W	watt
mW	milli-Watt (10^{-3} W)
μJ	micro-Joule (10^{-6} J)
mJ	milli-Joule (10^{-3} J)
T_g	transition temperature of substrate
E_g	energy bandgap
$h\nu$	photon energy
R	free radicals
I	photoinitiators; intensity of excitation source
k_{i1}	first reaction rate constant
k_{i2}	second reaction rate constant
k_p	propagation rate constant
k_t	termination rate constant
M	monomer molecules
P_1	active, growing free-radical polymer
P_N	free-radicals polymer attach to form macroradical
S	photosensitizer molecule
$n^{(1)}$	number of molecules excited by SPA
$n^{(2)}$	number of molecules excited by TPA
N_g	density of molecules in the ground state
$\sigma(\nu)$	cross section of absorption process at frequency ν
$\delta(\nu)$	TPA cross section at frequency ν
z	distance from the focal plane

ρ_0	primary particle density
$\rho(r, t)$	locally generated density of radicals
ρ_{th}	minimum density of radicals
$N(r, t)$	photon flux
N_0	Constant photon flux
σ_2	effective two photon cross section
σ^a_2	Ordinary two photon absorption cross section
η	efficiency of the initiation process
d	voxel diameter
l	voxel length
t	total irradiation time
τ_L	laser pulse width
n	number of pulses
z_R	Rayleigh length
f	effective focal length; laser repetition rate
λ_0	laser wavelength
D	laser beam diameter
$2\omega_0$	theoretical laser spot size
DOF	depth of focus
Φ_0	maximum laser fluence
Φ_{th}	threshold laser fluence
$\Phi(N_{eff})$	laser fluence at N_{eff}
E_{pulse}	measured laser pulse energy
N_{eff}	effective number of pulses
v	scan speed
R	scanning resolution
%Overlap	Spot-overlap as a percentage of focal spot diameter
$C_p(T)$	specific heat
$q(r)$	input heat flux

LIST OF ACRONYMS

PC   polycarbonate

PECVD   plasma enhanced chemical vapour deposition

SEM   scanning electron microscope

SPA   single photon absorption

TPA   two photon absorption

UV   ultraviolet

XRL   X-ray lithography

µTAS   micro total analysis system

MEMS   micro-electro-mechanical system

MPA   multi photon absorption

MPP   Multi photon polymerization

CHAPTER 1

INTRODUCTION

1.1 NANOCOMPOSITES

Nanocomposites are commonly defined as the combination of multiphase materials where at least one of the constituents has one dimension in the nanometer range [1-3]. The nanoscale constituent can be one dimensional (examples include nanofibre and nanowires), two-dimensional (layered mineral like nanoclay) or three-dimensional (spherical particles in nanoscale range) [2, 3]. The multifunctionality of nanocomposites can be attributed to the combination of the constituent materials. Desired properties can be obtained from a nanocomposite through the selection of the constituent materials and the size of the nanoparticles based on the required application. Current research has focused in the areas of manufacturing techniques and material combination for the manufacturing of the nanocomposites.

Nanocomposites are progressing with the use of a combination of atomic scale characterization and detailed modeling [1]. In the early 1990s, Toyota Central Research Laboratories in Japan reported working on a Nylon-6 nanocomposite [4], which a very small amount of nano filler loaded, resulted in a pronounced improvement of thermal and mechanical properties. The properties of nanocomposite materials depend not only on the properties of their individual parents (nano filler and nylon, in this case), but also on their morphology and interfacial characteristics [3].

The transition from microparticles to nanoparticles yields dramatic changes in physical properties. Nanoscale materials have a large surface area for a given volume [6]. Since many important chemical and physical interactions are governed by surfaces and surface properties [1], a nanostructured material can have substantially different properties from a larger-dimensional material of the same composition. In the case of particles and fibers, the surface area per unit volume is inversely proportional to the material's diameter. Thus, the smaller the diameter, the greater is the surface area per unit volume [6]. Common particle geometries and their respective surface area-to-volume ratios are shown in Figure 1.1. For the fiber and layered material, the surface area/volume is dominated, especially for nanomaterials, by the first term in the equation. The second term ($2/l$ and $4/l$) has a very small influence (and is often omitted) compared to the first term. Therefore, logically, a change in particle diameter, layer thickness, or fibrous material diameter from the micrometer to nanometer range, will affect the surface area-to-volume ratio by three orders of magnitude [7].
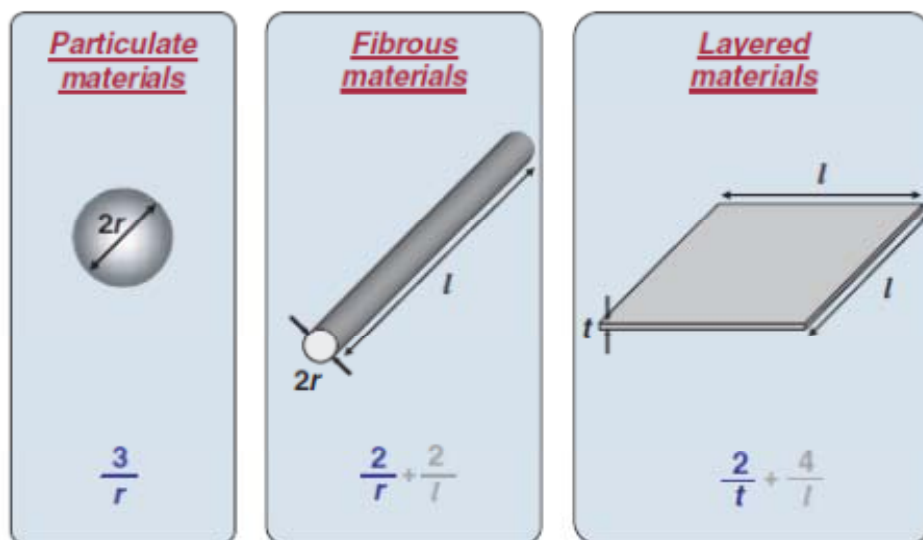
Figure 1.1 Common particle reinforcements/geometries and their respective surface area-to-volume ratios.[7].

Typical nanomaterials currently under investigation include nanoparticles, nanotubes, nanofibers, fullerenes, and nanowires. In general, these materials are broadly classified by their geometries [8]: particle, layered, and fibrous nanomaterials [7,8]. Carbon black, silica nanoparticle, polyhedral oligomeric sislesquioxanes (POSS), can be classified as nanoparticle reinforcing agents, while nanofibers and carbon nanotubes are examples of fibrous materials [8]. When the filler has a nanometer thickness and a high aspect ratio (30–1000) plate-like structure, it is classified as a layered nanomaterial (such as an organosilicate) [9].

In general, the reinforcement provided by nanomaterials comes from their high aspect ratios [6]. The properties of a nanocomposite are greatly influenced by the size of its filler material and the quality of the interfacing between the matrix material and the filler material. Depending on the nature of the filler material used (layered silicate or nanofiber, cation exchange capacity, and polymer matrix) and the method of preparation, significant differences in composite properties may be obtained [10]. For example, when the polymer is unable to intercalate (or penetrate) between the silicate sheets, a phase-separated composite is obtained, and the properties stay in the same range as those for traditional microcomposites [9]. In an intercalated structure, where a single extended polymer chain can penetrate between the silicate layers, a well-ordered multilayer morphology results with alternating polymeric and inorganic layers. When the silicate layers are completely and uniformly dispersed in a continuous polymer matrix, an exfoliated or delaminated structure is obtained [9]. In each case, the physical properties of the resultant composite are significantly different, as discussed in the following sections. Analogously, in fibrous or particle-reinforced polymer nanocomposites (PNCs), dispersion of the nanoparticle and adhesion at the particle–matrix interface play crucial roles in

3

determining the mechanical properties of the nanocomposite. Without proper dispersion, the nanomaterial will not offer improved mechanical properties.

Properties over that of conventional composites, in fact, a poorly dispersed nanomaterial may degrade the mechanical properties [11]. Additionally, optimizing the interfacial bond between the particle and the matrix, one can tailor the properties of the overall composite, similar to what is done in macrocomposites. For example, good adhesion at the interface will improve properties such as interlaminar shear strength, delamination resistance, fatigue, and corrosion resistance. Finally, it is important to recognize that nanocomposites research is extremely broad, encompassing areas such as electronics and computing, data storage, communications, aerospace and sporting materials, health and medicine, energy, environmental, transportation, and national defense applications [1]. The focus of this chapter is to highlight the state of knowledge in processing, manufacturing, characterization, material properties, challenges, and potential applications for the most common polymer nanocomposites (while numerous products utilizing nanoscale materials are currently available, such as automotive, textile, and cosmetic applications, the major impact for nanomaterials is anticipated to be at least a decade away [1]).

1.2 POLYMER NANOCOMPOSITES

The use of organic or inorganic filler has become ubiquitous in polymeric systems. Polymer composites are manufactured commercially for many diverse applications such as sport goods, aerospace components, automobiles, etc. In the last 20 years, there has been a strong emphasis on the development of polymeric nanocomposites.

In general, the unique combination of the nanomaterial's characteristics, such as size, mechanical properties, and low concentrations necessary to effect change in a polymer matrix, coupled with the advanced characterization and simulation techniques now available, have generated much interest in the field of nanocomposites. In addition, many polymer nanocomposites can be fabricated and processed in ways similar to that of conventional polymer composites, making them particularly attractive from a manufacturing point of view.

1.3   FABRICATION OF POLYMER NANOCOMPOSITE MICROSTRUCTURES

The technological advancement in the field of MicroElectroMechanical Systems have demand for the fabrication of 3D micro/nanostructures and devices. The excitement surrounding the nanoscale science and technology gives us unique opportunities to develop and study revolutionary processes and materials. Nanocomposites embedded with 2D and 3D micro/nano materials find many applications in the field of medicine, tissue engineering, drug delivery, antibacterial implants or catheters, modification of textiles, and modification of polymers. Several optical, electrical and magnetic applications, has opened up new areas of research for manufacturing nanocomposites with engineered nanoparticles material.

Researchers all over the world have been working on different micro/nano manufacturing techniques. Photolithography [4, 5], LIGA (German acronym for Lithographie, Galvanoformung, Abformung) [6, 7], Electrochemical Fabrication (EFAB) [8], localize electrochemical deposition [9] and laser sintering [10, 11] are some of the techniques used for micro/nano fabrication. Some of these techniques have been used for the fabrication of nanocomposites by dispersing nanoparticles, nanofibers or nanotubes in polymer resins.

1.3.1 PHOTOLITHOGRAPHY

Photolithography is one of the widely used techniques for fabrication of nanocomposites [12]. Hong et al. presented two photolithography-based approaches to directly micromachine photopatternable superhydrophobic micropatterns with excellent adaptability and flexibility to a wide variety of substrates, employing the nanomorphology and hydrophobicity of polytetrafluoroethylene (PTFE) nanoparticles and the photopatternability and transparency of an SU-8 photoresist. [12].

In photolithography, a light source such as UV light is used to polymerize the photo-responsive resin with suspended nanoparticles through a mask [4]. Depending upon the requirement of the feature, a mask is prepared and the feature is transferred using a UV source light. The removal of the unaffected part by the light source is performed using the secondary process of chemical etching. UV light has been used primarily for transferring the mask, but various other alternatives such as nanoimprint lithography, X-ray lithography, and ion projection lithography are being explored [4,5]. This technique has been researched and developed for several decades, but the resolution of the fabricated feature using photolithography is limited due to the limitation of optical diffraction. Photolithography also requires the use of expensive masks and molds for the fabrication process. These methods are effective for the mass fabrication of high resolution microfeatures, but they are limited to 2D geometries [5]. Polymer nanocomposite microstructures can be obtained by dispersing the photosensitive resin with naomateirals [13]. Figure 1.2a illustrates a reproduction of the smallest features of the used photomask prepared from a resist containing Au. The accuracy of the generated nanocomposite patterns suggests that the lithographic performance of photoresists is not affected by the presence of Ag and Au salts at

6

low concentration. Figure 1.2b–c shows the microscope images and the corresponding profilometry of patterns from an initial concentration of 0.025 M AgClO$_4$ [14].
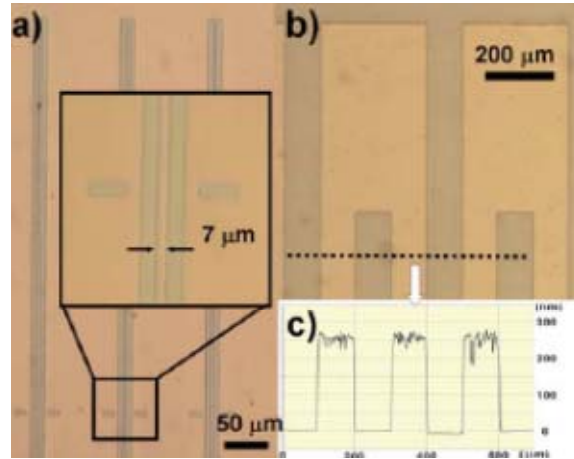
Figure 1.2 Photolithography nanofabrication technique a) 7 mm-wide lines made from a resist formulation containing Au, b) Patterns made from a 0.025 M AgClO$_4$ resist formulation containing lines, and c) the corresponding profilometry [14].

1.3.2 LIGA

The LIGA technique was invented approximately 20 years ago. It is a powerful method that facilitates the high volume production of nanocomposite components for many fields of applications [13]. Kondo et al, presented designs, fabrication and experimental results of high power electrostatic microactuators, using LIGA process which produced a high aspect ratio microstructures of polymer nanocomposite, as shown in Figure 1.3 [15].

The LIGA process makes use of the simple shadow printing process onto a resist on an electrically conducting substrate. After development of the irradiated resist, an electroforming step fills the holes of the relief with metal. This more stable body is used as a mold insert for

further molding or embossing steps [7]. The deep lithography step, performed by the use of highly parallel and collimated synchrotron radiation, is the basic step, thus not only defining the shape but also the structural accuracy of the final product. [15].
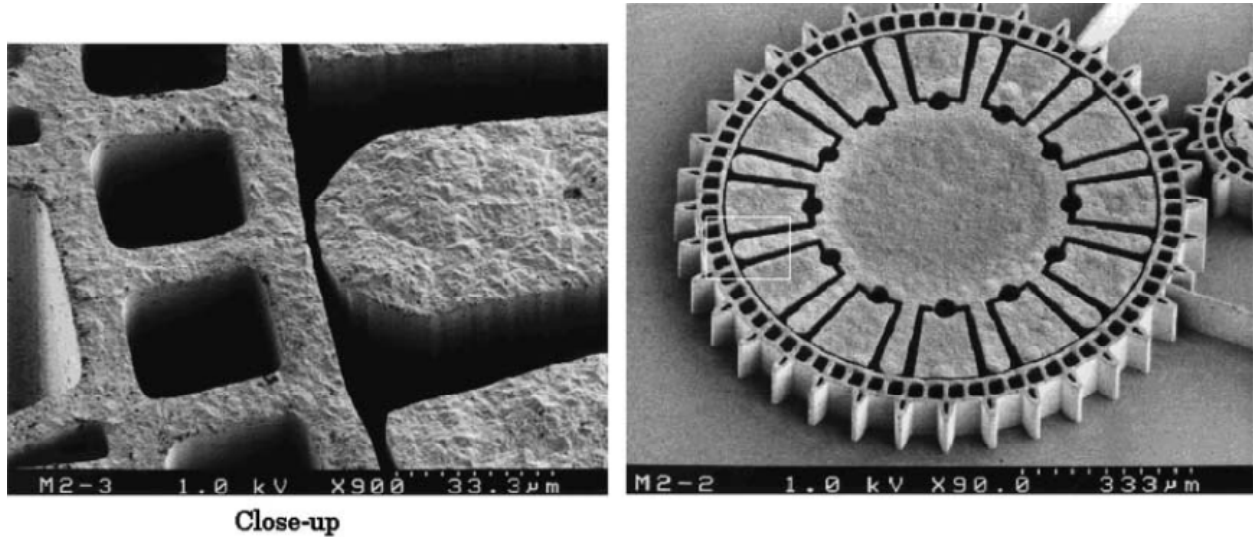
Figure 1.3 SEM image of a nanocomposite microstructure developed by LIGA [15].

Typically LIGA structures allow for the free choice of the lateral 2D pattern that is projected into the third dimension to form prismatic or cylindrical geometries. This technique has generally been used to produce structures with straight walls. However, for all major LIGA process steps, variations have been developed to increase the fabrication flexibility. Geometrical variations in the third (vertical) dimension are possible and can be obtained in different ways by modifying or combining process steps, in particular for producing shapes with increased dimensionality. The consecutive process steps of deep UV lithography, electroforming, and plastic molding can be used to fabricate three dimensional microstructures with nearly no restrictions in their lateral shape in a large variety of nanocomposites [13].

1.3.3   ELECTROCHEMICAL FABRICATION

A relatively new approach called Electrochemical Fabrication (EFAB) was initially invited to addresses the long development time for Optical MEMS, which can go up to 12 weeks. [16]. This technique has also been used for the fabrication of polymer nanocomposite microstrucutres. Ouyang Mi, et al reported the fabrication of nanocomposite film of polypyrrole (Ppy) and TiO2 nanotube (TNT) arrays via electrochemical methods. A novel dual-layered photoreceptor based on the nanocomposite film as a charge generation layer (CGL) was designed and fabricated [16].

EFAB is a solid free-form fabrication technology that creates complex, miniature three-dimensional shapes based on 3-D CAD data [8]. Inspired by rapid prototyping techniques, EFAB generates complex shapes by stacking multiple patterned layers. Unlike rapid prototyping, EFAB is a batch process suitable for volume production of fully functional devices in engineering materials, not just models and prototypes [8].

EFAB has certain limitations and shortcomings. EFAB is a process that requires the use of a mask to build two-dimensional (2D) planar structures. High aspect ratio geometries are thus a result of multiple steps of material deposition or removal through the use of several masks, which requires increased fabrication time and cost. [15].

1.3.4   LOCALIZE ELECTROCHEMICAL DEPOSITION.

In a localized electrochemical deposition (LECD) technique, a conducting microelectrode is used to fabricate high aspect ratio structures [9]. During fabrication, localized deposition is produced by placing an electrode tip, which has micrometre-scale dimensions, near a substrate in

an electrolyte and applying an electric potential between them. Due to the highly localized electric field in the region between themicroelectrode and the substrate, confined deposition is produced. High aspect ratio structures result from the displacement of the end of the electrode along the trajectory of the desired geometry while maintaining continuity with the deposited material. However, nanocomposite structures produced by this method are usually porous and have feature sizes in the tens of micrometers due to the limitation in producing and maintaining a sharp conductive probe, and in confining the electric field down to nanoscale dimensions [17].

1.3.5   LASER SINTERING

Another method that has been widely used in the manufacturing of nanocomposites is laser sintering technology. In this method of fabrication, a high intensity laser is used to ablate the material and form nanoparticles [18]. Chen et al, reported a new method for conductive nanocomposite microfabrication in which they were able to lower the percolation threshold of the nanocomposite [18]. This process is performed inside a liquid polymer resin which is then polymerized using UV light to form nanocomposites layers. The main advantage of this method is that metals, non-metals, glass, polymers can be used to fabricate nanocomposites with varying properties [19-23]. The main disadvantage in this method is that it is mostly limited to planar geometries. Stacking of different layers has been tried, but alignment and handling of the layers contributes to the limitation of aspect ratio of the micro device [10,11].

1.3.6   MULTIPHOTON MICRO/NANOFABRICATION

The nonlinear optical process of multiphoton absorption was first predicted in 1931 by the Nobel laureate physicist Marie Goeppert-Mayer in her doctoral dissertation [24]. The process

was not verified experimentally until the advent of the laser [25]. An intuitive explanation of MPA is that the transition from the ground electronic state to an excited electronic state that is usually achieved by the absorption of one high-energy photon is instead reached by simultaneous absorption of multiple low energy photons. The most common implementation of this is degenerate two-photon absorption (TPA) where both photons have the same energy. The spatial confinement of MPA excitation is used to induce a chemical reaction only at the laser focal point. This polymerization reaction can take place by radical reaction mechanisms which depend on the photoinitiator and monomer being used. The photoinitiators used for radical MPA vary from small molecules to large conjugated molecules. A number of groups have reported the successful application of radical MPA using a variety of resins, homemade and commercial, and different excitation sources [24-28]. Custom photoinitiators have been designed by several groups and have been shown to be effective both for low threshold powers and for the ability to use less expensive laser systems. While the benefits of custom initiators are clear, their availability is limited. Commercial resins or resins made of commercial components have the benefit of accessibility but suffer from a slightly higher power threshold for fabrication. However, for the entire laser systems used, the threshold for these resins is always well below the available power and therefore their use is completely practical.

Due to a combination of optical nonlinearity, MPA can achieve resolution that is considerably better than that predicted by the diffraction limit. The probability for MPA is proportional to I^n (where I is the light intensity and n is the number of absorbed photons), which effectively narrows the point-spread function (PSF) of the beam near the focal point so that it is smaller than the diffraction limit at the excitation wavelength. The real benefit of the optical nonlinearity of MPA lies in the negligible absorption away from the focal point. Photoinitiator

concentrations can be employed that are approximately ten times higher than would be feasible for single-photon excitation without any fear of out-of-plane polymerization.

Multi Photon Absorption (MPA) is a relatively new and evolving technique for the manufacturing of micro/nano structures. This technique, unlike other methods, does not involve any secondary operations or processes for nanocomposite fabrication [29]. Micro/nano structures and devices are manufactured with higher accuracy and complexity using MPA than other prevailing methods of fabrication for various applications. When an ultrashort laser pulse is focused in a photo responsive polymer resin, a solid voxel (volumetric pixel) is formed. The voxel size defines the minimum resolution of the polymer that is converted into solid form. Complex 2D and 3D structures can be formed by scanning the laser in the photo responsive resin [30, 31]. Research on manufacturing of micro/nano structures from different types of polymers using MPA has been conducted over a brief span of time [1, 5, 28, 29]. In certain applications there is a need of fabrication of complex nanocomposite structures [32- 35]. The prevailing techniques for nanocomposite manufacturing are good for planar or 2D device fabrication. For maskless manufacturing 2D and 3D nanocomposite devices with accuracy and precision there is a need of identifying or performance research towards the development of new maskless fabrication techniques using MPP due to its advantages over other methods.

1.3.7 SUMMARY

In summary, some of the most commonly used nanofabrication technique has been discussed. These methods need to go through several complicated and time consuming steps before producing the final shape of the nano/microstructures. Also, these techniques either need the use of expensive masks, which cause the resolution to be limited by diffraction, or they are

scanning beam based techniques which has the drawbacks of high cost and long exposure time. These limitations have motivated researchers to explore unconventional approaches. Table 1.1 shows some of the comparative performance of the conventional nanofabrication techniques.

Nanocomposite materials hold the potential to redefine the field of traditional composite materials both in terms of performance and potential applications. There is no doubt that polymer nanocomposites have tremendous market potential both as replacements for current composites and in the creation of new markets through their outstanding properties. But developing the processing–manufacturing technologies in terms of quantity and value for commercialization will be one of the biggest challenges. For example, dispersion of nanoparticles or chemical compatibility with matrix materials is critical issues.

Table 1.1 Comparison of nanocomposites fabrication techniques.

Technique	Resolution	Throughput	Cost	Capability
Photolithography	moderate	good	poor - moderate	2D
LIGA	Good	poor	poor	2D, 3D
Electrochemical	poor - moderate	good	moderate	2D
Localize electrochemical deposition	poor - moderate	moderate	moderate	2D
Laser sintering	Good	moderate	moderate	2D, 3D
Multiphoton	Good	moderate	moderate	2D, 3D

A homogeneous dispersion of nanoparticles in a polymer by using existing/traditional compounding techniques is very difficult [34-36]. At the same time if it is subjected to force, premature failure takes place in the final product [37]. Degassing is another critical problem while processing a nanocomposite. The air trapped while pouring the highly viscous material in a mold, initiates cracks and failure of specimen can take place under low strains [31]. The alignment of nanoparticles in the composite matrix can be critical to maximize properties such as strength, modulus, and toughness [32].

1.4   RESEARCH OBJECTIVES

As of now, various applications in different fields of scope of the multiphoton polymerization (MPP) techniques indicate that this process has blossomed over the past decade and achieved rapid success. However, there is always need for improvement in certain areas like increasing the spatial resolution and widening the range of applicable materials. The main objective of this thesis is to introduce a new concept of fabrication of nanofiber reinforced microstructures, using multiphoton polymerization process. The parameters that influence this technique have to be investiaged in depth.

Femotsecond laser have been used to produce features that are so small in size. They are simply imminent to make an impact in various industries which created a high demand and interest in this nanofabrication technique. As a result of this potential impact, the following are explored in the scope of this thesis:

- Using MPP for the direct formation of nanofiber reinforced microstructures.

- Study the fundamentals of MPP and experiment the prospect of dual wavelength polymerization.

- Evaluate the effect of laser parameters such as repetition rate, pulse width, scanning speed, laser power, and exposure time, on quality and size of the features produced.

- Demonstrate potential applications of the new fabrication methods by developing a DNA biosensor.

1.5   THESIS OUTLINE

The outline of this thesis is as follows. Chapter 2 introduces the fundamentals of MPP. Chapter 3 provides a detailed description on the femtosecond laser system experimental setup, materials and material characterization equipment used for the research. In chapter 4, the experimental procedures and the results are introduced along with a detailed discussion over the observations of the experiments conducted. Plots providing information about the size of the micro/nano composite structures fabricated nanoparticles are also presented and discussed. Chapter 5 focuses on examining mechanical, electrical and magnetic properties of nanocomposites microfeatures fabricated through the new method. Chapter 6 shows the potential applications of this fabrication method through the creation of nanocomposite microelectrodes for DNA sensing. Finally, Chapter 7 presents the conclusions along with recommendations for future work.

CHAPTER 2

FUNDAMENTALS OF MULTI-PHOTON

POLYMERIZATION

A relatively new technique called multiphoton polymerization (MPP) is an advanced and efficient method for manufacturing micro/nano structures and features using ultrashort laser pulses from a near infrared laser source. One photon polymerization (1PP) process is also used for the purpose of micromachining. However 1PP is a planar technology technique with layer-by-layer polymerization steps, while MPP is truly a three dimensional high-resolution technology [38]. A major issue is that MPP uses a wavelength higher (double or triple) that needed for linear absorption [39].

An intuitive explanation of multiphoton absorption (MPA) is that the transition from the ground electronic state to an excited electronic state that is usually achieved by the absorption of one high-energy photon, instead it's reached by simultaneous absorption of multiple low energy photons. Multiphoton Absorption is a nonlinear process based on the simultaneous absorption of two or more photons in a single event. The most common multiphoton absorption processes are degenerate two- and three-photon absorption effects. The scientific interest for multiphoton absorption processes has been growing dramatically, especially during the last decade. Two-photon absorption (2PA) has found multiple applications in micro/nanofabrication because of its high spatial resolution. Nevertheless, the wavelengths typically used for 2PA excitation, 500-800 nm, are still too short to even further reduce the Rayleigh scattering [40]. To overcome this limitation, higher order nonlinear processes such as three photon absorption (3PA) can be

employed. Because three-photon absorption typically takes place at longer wavelength (~ 1000 nm) [41], the Rayleigh scattering losses in the near infrared (NIR) region can be minimized. However, 3PA has a disadvantage: it requires high irradiances to induce the promotion of electrons from the ground state to the final excited state.

2.1   FUNDAMENTALS OF MPP

Maria Göppert-Mayer first predicted the existence of two-photon absorption (TPA) in 1931. In honor of her work, the SI unit for the TPA cross section (δ) is named Göppert-Mayer (GM). A GM is equal to 10^{-58} m^4 s / photon, and for a typical molecule the peak value of δ is in the range of tenths to tens of GM for the lowest-lying electronic transition that is two-photon allowed. However, molecules that are designed to optimize TPA can have peak values of δ that are several orders of magnitude larger [40]. Because of the high intensities required, the experimental demonstration of TPA relied upon the invention of the laser and, therefore, did not take place until 1961 [41]. With a continuous-wave laser, achieving a sufficient value of intensity squared to drive TPA to a significant extent requires high power. For this reason, although TPA was used for selected applications, it did not find broad use for many years after its demonstration. This situation changed with the development of relatively simple, solid-state femtosecond (fs) lasers in the late 1980's and early 1990's. The advantages of using ultrafast pulses to drive MPA are illustrated by the Ti:sapphire laser. A typical Ti:sapphire laser puts out pulses with a duration of 100 fs at a repetition rate of approximately 80 MHz. Thus, a sufficient peak intensity to drive efficient MPA can be realized at a low average laser power. While the output of a Ti:sapphire laser is in the range of hundreds of milliwatts, two-photon excitation can generally be accomplished at average powers of a few milliwatts or less, depending on the

focusing conditions and the species being excited. Most Ti:sapphire lasers operate at a wavelength of about 800 nm, although with appropriate optics they can operate in the range of ~700-1100 nm.

Figure 2.1 shows an example of the degree of localization of possible excitation using MPA. The sample, a solution of rhodamine B, is excited using either an ultraviolet (UV) lamp focused through a microscope objective with single-photon absorption or a laser focused through a microscope objective with two-photon absorption. In the former case, fluorescence is observed along the entire beam path through the solution. The number of excited molecules in any transverse cross section of the laser beam decreases across the sample as light is absorbed, but would otherwise be identical for any such plane. In the latter case, the fluorescence is confined to a relatively small volume in the region in which the square of the intensity in a transverse cross section of the beam is great enough to induce significant absorption.
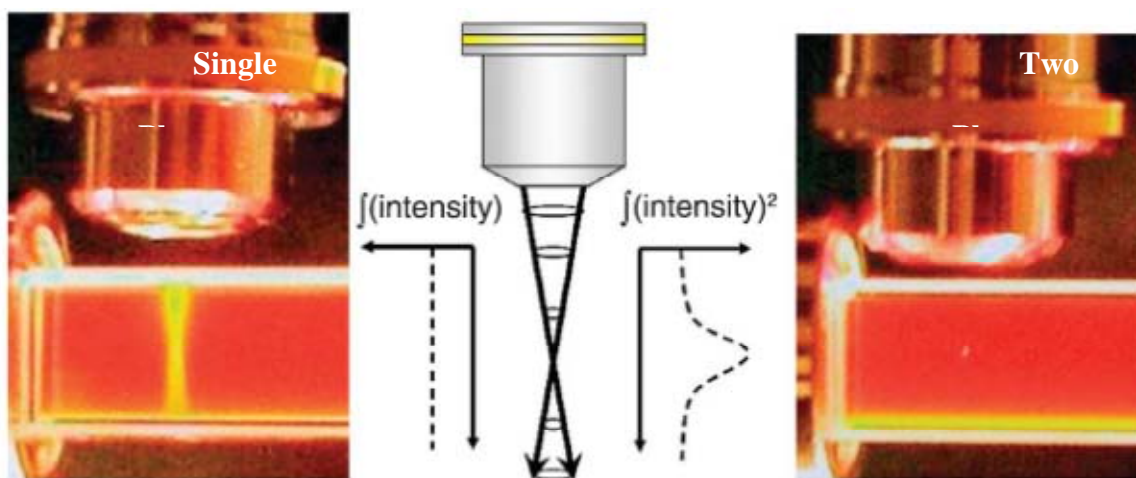
Figure 2.1 Fluorescence in a rhodamine B solution excited by single-photon excitation from a UV lamp (left) and by TPA of a mode-locked Ti:sapphire laser tuned to 800 nm (right). In the former case, the integrated intensity is equal in all transverse planes, while in the latter case the integrated intensity squared is peaked in the focal region [42].

2.2   MULTIPHOTON ABSORPTION POLYMERIZATION

The most well-developed MPA-based fabrication technique is multiphoton absorption polymerization (MAP) [43-52]. In this technique, MPA is used to expose a photoresist, one volume element (voxel) at a time. Once the prescribed pattern has been scanned, the resist is developed to reveal the desired three-dimensional structure. Examples of structures created with MAP are shown in Figure 2.2. The excitation source in the MPA experimental setup is usually a femtosecond laser oscillator.

Three dimensional patterns are scanned by moving the laser focus relative to the sample (with galvanometric mirrors, for instance) or by moving the sample relative to the laser (with a piezoelectric stage, for instance), or combination of the two. If the substrate upon which fabrication occurs is transparent, then the fabrication process can be monitored using transmitted light, as exposure of the photoresist generally leads to a visible change in refractive index. Samples are generally prepared on a substrate to which the photoresist adheres well,. The structures that are fabricated contact the substrate over a large enough area so as not to be washed away upon development. The development usually involves washing the sample in a solvent or a series of solvents. In the case of a negativetone photoresist, the solvent washes away the unexposed material, whereas for a positive-tone photoresist, it is the exposed areas that are washed away. The development often leads to some degree of shrinkage of the structures. The resolution attainable with MAP is considerably finer than the diffraction limit. The most meaningful measure of the attainable resolution is the dimension of an isolated voxel. With 800nm light, it has been proven that it is possible to fabricate voxels with a transverse dimension smaller than 100 nm [53, 54]. This feat is made possible by the nonlinearities inherent in the

MAP exposure process. The fact that the polymerization efficiency depends nonlinearly upon the laser intensity provides reduction in feature size.
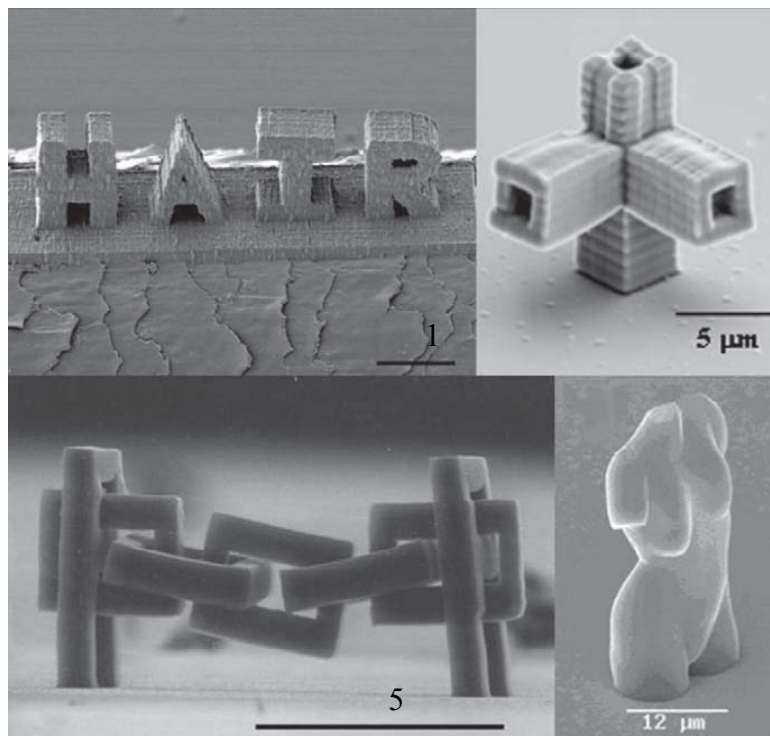
Figure 2.2 Examples of structures created with MAP. (a) A microstructure created directly on a human hair; [46]. (b) A complex set of microchannels fabricated in polydimethylsiloxane. [47]. (c) An interlocking chain [48]. (d) A microscopic rendition of the torso of the Venus de Milo created from a hybrid organic/inorganic material [49].

Thus, at low laser intensities exposure will only occur in the innermost regions of the focal volume, leading to smaller voxels. Considerably smaller features have been observed in suspended lines, although asymmetric shrinkage upon development is likely to play a considerable role in determining the dimensions [55]. As a result of optical constraints, the longitudinal dimension of a voxel is generally significantly greater than the transverse dimensions, causing the voxels to take on a cigar shape [56]. Typical aspect ratios of voxels are on the order of 3:1 or greater [56,57]. The smoothness of structures fabricated using MAP is

determined primarily by the voxel dimensions, density, and the mechanical and optical stability of the fabrication system. A surface roughness on the order of tens of nanometers is easily attainable, making MAP suitable for the creation of high-quality optical devices.

2.2.1 RADICAL POLYMERIZATION

Polymerization is one of the basic processes for fabrication of micro/nano structures. When a light source is focused on a photo-responsive polymer solution, a cross link reaction takes place between the monomer molecules, leading to a polymerization chain reaction. A long polymerized chain results in manufacturing of 2D and 3D structures.

Once the basic components of any photoresist, the monomers or oligomers, are excited they are solidified by polymerization. The important feature of polymerization is the chain reaction of macromolecules, as shown in Eqn. (2.1) [58].

$$M \xrightarrow{M} M_2 \xrightarrow{M} M_3 \dots M_{n-1} \xrightarrow{M} M_n \tag{2.1}$$
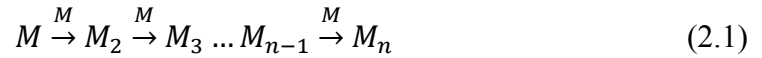
Here M is the monomer or oligomer unit, and M_n, the macromolecule containing n monomer units. The overall process of photopolymerization can be sub-divided into three stages: initiation, propagation and termination and which will be described in the following sections.

2.2.2 INITIATION

The production of active species that attack monomers or oligomers is called photoinitiation, the most important step in photopolymerization. The initiation phase begins with the formation of the free radicals, R, due to the absorption of photons by the photoinitiators, I.

$$I + nhv \xrightarrow{k_{i1}} nR \qquad (2.2)$$

Here, h is Plank's constant, v is the frequency of the photon, and k_{i1} is the reaction rate constant for the first initiation reaction. The primary radicals R is then attach to monomer molecule, M, to complete the initiation phase.

$$R + M \xrightarrow{k_{i2}} P_1 \qquad (2.3)$$

Here, P_1 is the active, growing free-radical polymer and k_{i2} is the second initiation reaction rate constant. The photoinitiation can be expressed by a photosensitizer molecule, S, which absorbs light and then transfers the energy to a photoinitiator.

$$S + nhv \rightarrow S^* \ldots \rightarrow I \rightarrow nR \qquad (2.4)$$

The quantum yield of general monomers and oligomers is very low. In order to increase the initiating efficiency, one or several low-weight molecules that are more sensitive to light irradiation are added. They form initiating species of radicals or cations by absorbing photons. Such small molecules are called photoinitiators. In a commercial resist, photoinitiators are usually used as an additive to enhance the photopolymerization.

2.2.3   PROPAGATION

In the propagation phase, monomer molecules attach to the growing, free-radical polymer to form macroradicals, P_N (N=1,2,. . .), which combine with new monomers, and so on; so the macro-radicals expand in a chain reaction. As long as the polymer chain remains reactive, more monomer molecules continue to adhere to the chain. Here, k_p is the propagation rate constant.

22

$$M + P_{N-1} \xrightarrow{k_p} P_N \tag{2.5}$$

2.2.4 TERMINATION3

Polymer chain termination occurs either through radical combination, which is when a primary radical attaches to the growing, free-radical polymer or two active polymer radicals attach together to form dead polymer P, or through the trapping of active radicals between immobile cross linked polymer. Here, k_t is the termination rate constant.

$$P_N + P_M \xrightarrow{k_t} P \tag{2.6}$$

Polymerization takes place when the ultrashort laser pulse is targeted in the photo-responsive polymer solution. The laser light is composed of numerous photons carrying energy equivalent to h*ν (where h is Planck's constant and ν is frequency). When these photons are targeted in the photoresponsive solution, the photons transfer the energy to the photo-initiator molecules and free radicals are generated. These free radicals are responsible for initiating the polymerization reaction [38]. When one photon has sufficient energy to generate a free radical, the process is called as single photon absorption, and when two photons are simultaneously required for generation of free radical, it is termed two-photon absorption process. In multi photon absorption more than two photons are required for radical generation [43].

2.3 PHOTORESISTS FOR MAP

Negative-tone photoresists (also called prepolymer resins) used for MAP are generally either viscous liquids or amorphous solids (such as gels). A resin contains two key components: a hotoinitiator that is excited via MPA and monomers and/or oligomers that react to form a solid

that survives development. Resins may also contain other components, such as coinitiators or radical inhibitors, depending upon the nature of the initiation and polymerization reactions.

The majority of the materials used for MAP undergo radical polymerization. In this chemistry, MPA excites a photoinitiator that subsequently forms two or more radicals. These radicals in turn generate a chain reaction that causes the monomers/oligomers to cross-link. A highly cross-linked polymer is insoluble in the solvent used for development, and so will survive the washing steps. Commercial radical photoinitiators, while generally having only modest TPA cross sections, often work quite well for MAP [44,57]. High radical quantum yields and initiation velocities tend to compensate for the low δ values of these initiators. Alternatively, some groups have focused on the synthesis of new initiators with TPA cross sections that may be orders of magnitude larger than those of commercial photoinitiators. In some cases, this allows polymerization to be accomplished at laser powers of significantly less than a milliwatt [8,16,26-29]. The large δ values of these initiators balance their lower radical yields and initiation velocities compared with commercial initiators. A number of strategies have been employed to increase δ, the most common of which is to create donoracceptor- donor structures.

Acrylates have been employed in the majority of MAP resins reported to date. A large range of acrylic monomers with different physical properties is available, and these materials can be polymerized readily. Other materials that have been used include hydrogels30, siloxanes31, and organic/inorganic hybrids [47,59]. Cationic polymerization is also finding increasing use in MAP, particularly with epoxy resins [44,57,60,61] such as SU-8. SU-8 is a convenient material for MAP because it is in an amorphous solid state during fabrication, circumventing the difficulties associated with flow of liquid resins. However, SU-8 also requires considerably more

processing than liquid resins. Also of note is the demonstration of positive-tone MPA lithography using a cationic initiator [62]. Positive-tone lithography makes the pattering of voids possible, as opposed to solid regions, and is therefore of use in applications such as microfluidic systems.

IRGACURE 369, (a photo-initiator provided by Ciba-Geigy) has good absorbance in the long wave region of the UV spectrum which is around 400 nm. Thus, the energy carried by one photon is not enough to generate free radicals from photo-initiator molecule [65]. When two photons target the photoinitiator molecule simultaneously, a free radical is generated as shown in Figure 2.3. The first photon excites the photo-initiator molecule to the transition state and the photo-initiator molecule remains in this state till the second photon hits this molecule to excite this molecule to the excitation state and lead to generation of free radical.

2.4   APPLICATIONS OF MAP

As a result of the high optical quality that can be achieved with MAP, many of the applications demonstrated to date have been in the area of photonics. Photonic structures that have been built with MAP include waveguides, couplers, interferometers [63], microlenses [64], microring resonators fabricated directly on optical fibers [65], and even microlasers [66]. Such applications are probably of the greatest interest within the communications window of the spectrum, i.e. wavelengths in the range of 1.5 μm [67]. The development of MAP materials with greater transparency in this wavelength range will be of considerable importance for such applications.

Free Radical

Excitation State

Second
Photon

Transition State

First
Photon

Molecule

Ground State
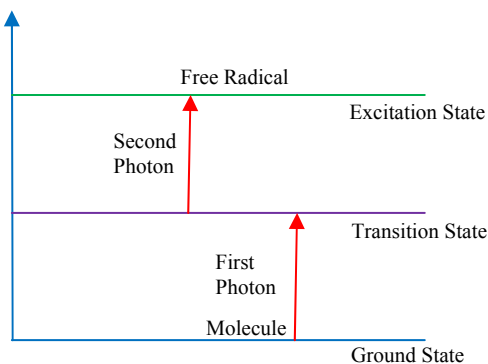
Figure 2.3 Two photon absorption process

Given MAP's ability to create features on a scale of 100 nm, it is an attractive technique for creating photonic crystals with stop bands in the visible range of the optical spectrum. Additionally, it is straightforward to design defects into photonic crystals created in this manner. A number of groups have explored the fabrication of photonic crystals using MAP [47,59,67]. An important issue in this field is that the contrast in refractive index between polymers and air is not sufficient to create a stop band. A number of different approaches have been taken to address this problem. One tactic is to develop hybrid organic/inorganic systems with a higher index of refraction [68].

While this is a promising approach, it has not yet been successful for the creation of photonic crystals with stop bands. Another avenue that has been pursued is the 'inversion' of structures created with MAP [69]. Structures can be backfilled with a high-index material and then the polymer can be removed. So far, the most successful technique for creating photonic crystals with high index contrast involves a double inversion [69,70]. Polymeric structures are inverted using silica, which is in turn inverted using Si. MAP has also been employed to create microscopic mechanical devices. For instance, a number of groups have demonstrated the

fabrication of structures such as cantilevers [71] and spring [70,72], although largely to test the mechanical properties of polymers created with this technique. In addition, Maruo and coworkers [73-75] have demonstrated the use of MAP for the creation of optically actuated micromechanical devices. They have created machines such as nanotweezers, nanoneedles, and nanorotors, all of which can be driven using optical tweezers. MAP has also been used to create structures from biomolecules via cross-linking [45,76-81]. Such cross-linking is generally performed using a sensitizer that can produce radicals upon excitation, such as Rose Bengal [45]. Enzymes cross-linked with MPA generally retain activity [78], and other types of proteins can also maintain binding affinity upon cross-linking [79]. In addition, proteins such as collagen can be cross linked to create scaffolds for cell growth. Cross-linking using MPA has also been demonstrated within living cells [81], and cross-linked protein structures have been translocated through cell membranes [82].

2.5   INCORPORATING OTHER MATERIALS

For many applications it is desirable to be able to incorporate additional materials, such as metals or metal oxides, into threedimensional structures. While direct MPA fabrication with such materials is possible in some cases [84-90], the quality of structures created in this manner is generally considerably lower than those achieved using MAP. Consequently, the post-fabrication chemical modification of polymeric structures created with MAP has become a topic of considerable interest in recent years. The inversion and double inversion strategies discussed above for photonic crystal fabrication are examples of a chemical modification approach. Other groups have developed methods for deposition of metals, including Ag, Au, and Cu, on polymeric structures created with MAP [91-93]. If structures are fabricated from two different

27

polymers, it is possible to perform selective chemical functionalization on one of those materials [89,91,92]. The selective deposition of metals in such functionalized regions has been demonstrated, and the extension of this technique to materials such as metal oxides or

biomolecules should be straightforward [40]. The ability to deposit metals selectively in chosen regions of threedimensional microstructures opens the door to new applications in areas such as photonics and electronics. It is possible to deposit metals with good electrical conductivity, enabling the creation of devices such as microinductors (Figure 2.4) [40].
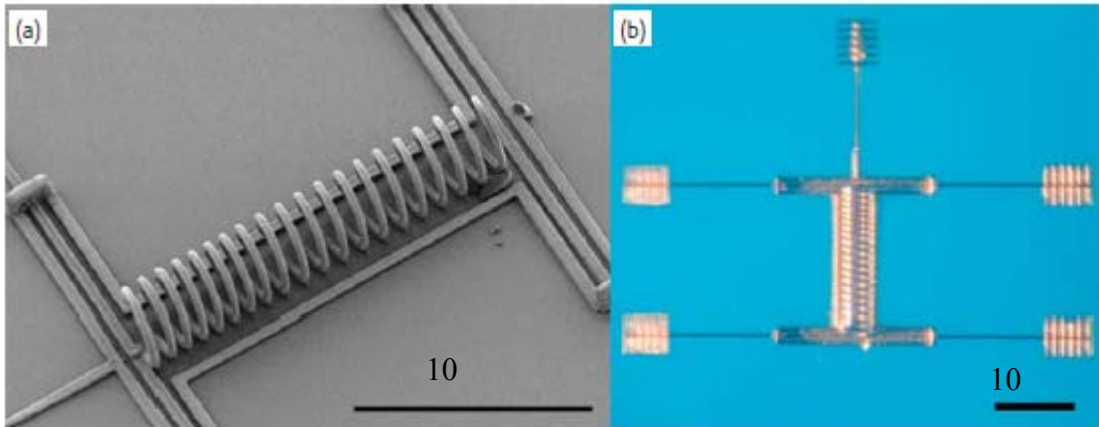
Figure 2.4 (a) Scanning electron and (b) optical micrographs of a microinductor created with MAP [40].

2.6   MASS PRODUCTION

In most implementations, MAP is a serial process in which structures are created one point at a time. If this technique is to be scaled up to produce devices on the wafer scale, it will be necessary to find means of increasing the fabrication speed by many orders of magnitude. Periodic three-dimensional structures, such as photonic crystals, can be fabricated rapidly and over large areas using interference techniques. For instance, in multibeam interference

lithography (MBIL) [94,95,96], the output of an amplified laser system is split into multiple beams that approach the photoresist from different directions with independently controllable polarizations. The resultant complex interference pattern is used to expose the photoresist via MPA. MBIL can be used to write a periodic pattern over a large area of a sample in a short time period. In another intereference-based approach, proximity-field nanopatterning (PnP) [97-99], a complex phase mask is placed in direct contact with a layer of photoresist. Light passing through the mask creates a complicated interference pattern that can expose the resist via single-photon absorption [97,98] or via MPA [99]. An advantage of PnP is that the mask need not be periodic, and so spatially varying structures can be created with this technique. However, the depth scale on which patterns can be created is not as large as that attainable using MBIL or MAP.

Multiple laser focal points can also be used to increase the rate of fabrication. For instance, by passing a laser beam through a multilens array [89,91,100], it is possible to fabricate multiple copies of the same structure simultaneously. By incorporating a two-dimensional spatial light modulator or multimirror array, it should be possible to fabricate at perhaps 100 independent points simultaneously. However, even with the introduction of more efficient photoinitiators, it is unlikely that multipoint schemes can increase the fabrication speed by more than a few orders of magnitude over single-point fabrication techniques. Another approach to mass production is to replicate three-dimensional structures created with MAP [101]. Slow fabrication of a wafer-scale master is acceptable if replicas of the master can be created rapidly. One strategy that has been used for replication is to employ microtransfer molding (μTM) [102], a soft-lithographic technique. In μTM, a mold is created by curing polydimethylsiloxane (PDMS) over a master structure. Replicas are produced by filling the mold with a molding material, pressing it against a substrate, and curing the replica. A single master can be used to

create as many molds as desired, and each mold can be used 20 times or more. Because of the elastic nature of PDMS, the range of structures that can be replicated is unexpectedly large. For instance, structures with large aspect ratios or significant overhangs do not get stuck in the mold, and can be replicated with high reproducibility [101]. However, traditional μTM still suffers from an important topological limitation: master structures with closed loops become locked within the mold and cannot be released. This problem can be avoided if structures are molded in successive layers, but such an approach cannot take full advantage of the three-dimensional capabilities of MAP fabrication.

The closed-loop problem in μTM has recently been solved with a technique called membrane-assisted microtransfer molding (MA- μTM) [103]. PDMS surfaces that are in close proximity have a tendency to adhere to one another, a property that is generally viewed as a problem in soft lithography. However, this phenomenon can be used to advantage in the replication of three-dimensional structures. In the master structure a thin membrane is created in the center of each closed loop, allowing the mold to be released from the master. The PDMS in the region of the membrane is then induced to adhere to itself before the mold is filled, allowing closed-loop replicas to be created. Replicas with or without membranes can be created readily via simple manipulation of the mold before the molding material is introduced [103].

2.7   SUMMARY

In summary, the MPA polymerization is a micro-/nanofabrication technique, in which, ultra short laser pulses are induced to polymerized photoresist. In contrary to lithography techniques based on SPA, the MPA is initiated by absorbing two or more simultaneous photons. Instead of a linear dependency on laser intensity, MPA exhibits a quadratic or higher relationship

with the laser intensity. Such nonlinear characteristic of MPA enables ultrashort pulse lasers to focus inside the volume of resist and polymerize the area in the vicinity of the focal point. As a result of this, MPA provides a mechanism by which chemical or physical processes can be activated with high spatial resolution in three dimensions.

CHAPTER 3

DESCRIPTION OF EXPERIMENTAL SETUP

Even though the concept of MPA was first realized in 1931, it could not be shown experimentally until 1961, when the continuous-wave laser with high energy became available to provide required photon flux density. Selection of laser system and understanding of the laser beam characteristics are most essential for understanding the MPA phenomena. In the first part of the chapter, a laser background and laser beam characteristics are presented. The substrate materials and the characteristics of the photoresists are also discussed here. In the later part, detailed experimental setup used for this study is discussed. All the experiments for this study were conducted using a high power, high repetition rate femtosecond laser in the Micro and Nano Fabrication research lab at Ryerson University, Toronto, Canada.

3.1 LASER BACKGROUND

The word "laser" is an acronym for Light Amplification by Stimulated Emission of Radiation. Through the supply of energy, the electron of an atom, molecule or crystal can change into an excited state. An electron absorbs a light particle (photon) and makes temporary transition to higher-energy state. Subsequently, it jumps back from a higher-energy to a lower-energy state as it emits a photon, which is seen as light. With conventional light sources, this transition occurs by spontaneous emission, that is, the timing and the direction in which the photon is emitted are random. In contrast, with a laser this transition occurs through stimulated

emission. This means a photon stimulates the energy transition within an active medium and thus a second photon emerges whose properties such as frequency, phase, polarization and direction are identical or proportional with the first photon. The emitted light is reflected back and forth between two mirrors through the active medium in the resonator. One of the two mirrors is semi-transparent (in the range of percent), in order to release light from the laser with higher amplification.

Soon after the invention of the first laser, several different types of lasers were invented. These lasers can be divided into different sub-groups according to the principal type of operation and construction. The solid-state lasers, like the Nd:YAG and gas lasers, like the helium-neon (HeNe), the argonion laser, the XeCL excimer laser, and the high-power CO_2 lasers are the most important types in material processing. The rest of the types, semiconductor lasers, liquid lasers, chemical lasers, and X-ray lasers, have more importance in research rather than in practical applications.

Laser applications in material processing has a very significant impact in mechanical engineering processes such as drilling, cutting, welding, and surface treatments. In electrical engineering and material science, processes such as photolithography, thin film deposition, doping, annealing, and defect scanning are also witnessing the importance of lasers. Most importantly, advancements in laser systems have opened doors for faster, efficient and inexpensive fabrication techniques in micro- and nano-fabrication industries. Laser processing is an ideal technique for these industries, because of its flexibility and ability to create high resolution features with great throughput.

3.2   LASER BEAM CHARACTERISTICS

The laser light is characterized by a number of interesting properties. Various applications of lasers exploit specific combinations of the laser properties. This sectionbriefly explains the most important properties of laser light.

In addition to high power, lasers have many other characteristics suitable for material processing. Monochromaticity is one of the unique characteristics of laser light. It is the most important property of laser beam and is measured in terms of spectral line width. It is nearly impossible to achieve perfectly monochromatic light, but laser light is many times more monochromatic than any other light. This is an important property because material processing is wavelength dependent. Hence, choosing a proper wavelength laser allows greater control in laser focus without compromising its depth.

The laser light is coherent, in which waves travels in the same direction (spatial coherence) at the same frequency and in phase (temporal coherence).   Spatial coherence describes the ability for two points in space, in the extent of a wave to interfere, when averaged over time. Temporal coherence is the measure of the average correlation between the values of a wave at any pair of times, separated by delay. It is a measure of how monochromatic a source is. The spatial coherence allows the laser beam to be focused tightly down to the micron level with a very high energy density necessary for extremely small features.

Collimation of the laser radiation is related with the directional nature of the beam. Highly directional beams are highly collimated beams, which can be focused on a very small area even at longer distances. Hence, energy can be efficiently collected on a small area without

much loss in the beam intensity over the longer distance of laser beam travel. The laser light is naturally collimated because it forms in optical resonator. The degree of collimation is directly related and measured with the beam divergence angles. The collimated light has divergence in the order of less than a milliradian. This characteristic of a laser is very important to achieve desired constant spot size at different focal lengths.

In most laser applications, it is necessary to focus, modify, or shape the laser beam by using lenses and other optical elements. In general, laser-beam propagation can be approximated by assuming that the laser beam has an ideal Gaussian intensity profile, corresponding to the theoretical TEM_{00} mode. In order to select the best optics for a particular laser application, it is important to understand the basic properties of Gaussian beams.

In TEM_{00} mode, the beam emitted from a laser is a perfect plane wave with a Gaussian transverse irradiance profile as shown in Figure 3.1. The Gaussian shape is truncated at some diameter either by the internal dimensions of the laser or by some limiting aperture in the optical train. The Gaussian has no obvious boundaries to give it a characteristic dimension like the diameter of the circular aperture, so the definition of the size of a Gaussian is somewhat arbitrary. The commonly adopted definition is the diameter at which the beam irradiance (intensity) has fallen to $1/e^2$ (13.5%) of its peak value.

3.3   SUBSTRATE MATERIALS

Almost all early designs and fabrications of microstrustures were on metallic and nonmetallic materials. This is unsurprising since standard photography and wet-etching techniques perfected in the microelectronics and semiconductor industries could be used to

efficiently structure all these materials to produce microstructures. In terms of fabrication methods, several considerations must be made for selecting suitable substrate material.
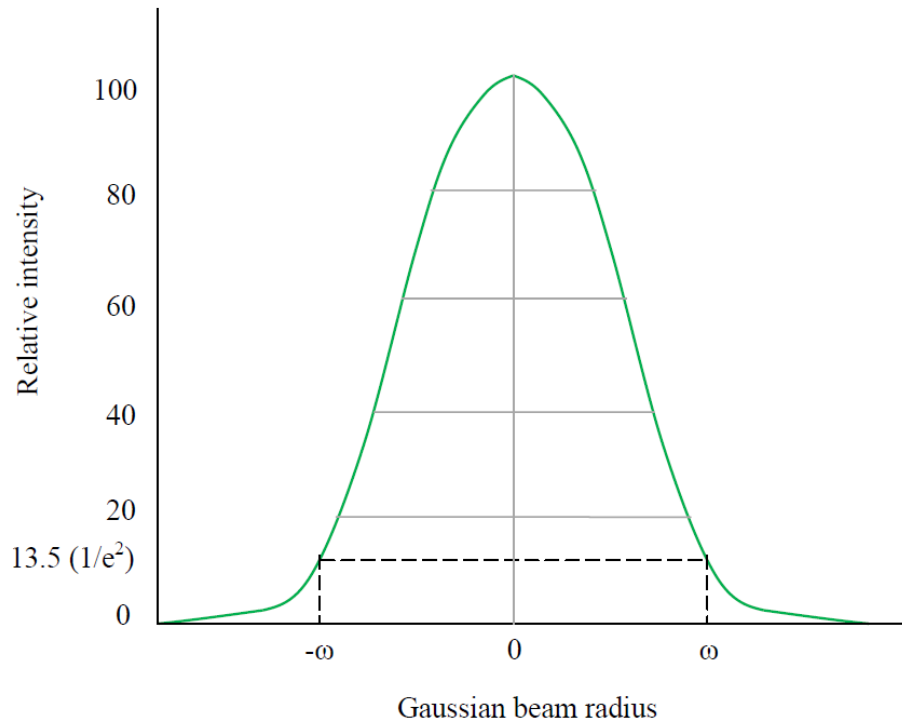
Figure 3.1 Intensity profile of Gaussian TEM_{00} mode

Silicon is the most widely accepted substrate and leverages commercially available equipment for fabrication from the well-established semiconductor and microelectronics fields. Advanced fabrication techniques with anisotropic etching can yield high aspect ratio silicon microstructures. However, silicon is seldom used for cellular analysis due to a lack of surface modification, low breakdown voltage, and most importantly its optical opacity. While silicon can be modified with a thermal oxide, the passivated surface has been shown to degrade rather rapidly due to protein absorption, limiting its long-term utility in cell-based assays. Since silicon is a semiconductor, applications employing high voltage such as capillary electrophoresis and

dielectrophoresis are challenging. Although oxide modification can minimize this problem to permit microgel electrophoresis on chip, separation field strengths have been limited to ~25 V/cm, resulting in longer analysis time and low resolution separations [104]. To enable optical detection, the opaque silicon substrate can be anodically bonded to a glass wafer to form silicon–glass microstructures. The major disadvantage of silicon substrate is relatively high cost and limitations in mass production, which is important for medical and clinical diagnostic applications that require disposable tools to eliminate cross contamination.

Nonmetallic's (like Glass) is a useful platform because it offers chemical surface modification for compatibility with many different assays, including capillary electrophoresis. It also has high mechanical strength, high chemical resistance, and low conductivity. Advantages of nonmetallic microsystems include fabrication with conventional wet etching techniques, high dielectric strength, low background fluorescence, and optical transparency in the visible wavelengths. Since the wet etching of the nonmetallic is isotropic, the critical dimension attained is larger than semiconductor substrates. Other disadvantage of nonmetallic substrate is the lack of disposability due to its high unit cost.

Laser-induced polymerization on the reflecting metal surface is more problematic due to interference effects and poor polymer adhesion to metals. MPP ofORMOCER on a metallic layer is possible for a smaller range of laser powers compared to the MPP on a nonmetallic substrate. Simultaneously the required threshold power for MPP process decreases. The first effect is related to adhesion problems and laser heating of the metallic layer. The reduction of the MPP threshold can be explained by the interference of the incoming and reflected laser beams in the vicinity of the metallic surface. In the interference maxima the polymerizationthreshold is

reduced due to higher intensity. In addition, the high intensity laser pulse creates free electrons by multiphoton photoelectric effect which can also influence the polymerization process. Possible laser heating effects at the metallic surface can result in a chemical destruction of the material. To avoid these effects, the interaction time of the laserbeam with the material (and the metallic surface) should be possibly short.

3.4   PHOTORESISTS

Photoresist is the generalized term for all photon sensitive macromolecule polymers. They are photon sensitive, therefore, can be optically solidified into pattern structure. When a femtosecond laser is tightly focused into the volume of photoresist, it initiates MPA polymerization.   There are two classes of photoresists which can be structured by MPA polymerization: positive and negative type photoresist. Figure 3.2 illustrates the difference between positive and negative photoresists.

The main difference between positive and negative types of photoresist is photochemical reactions responsible for linking or delinking of monomers. A positive photoresist that has long chain molecules can be broken by photon energy into short chains by the delinking process, while for negative photoresist, initially short chain molecules can join together to form long chains after absorbing photon energy.   The macromolecule polymers with long chains are insoluble in the developer where polymers with short chain molecules are soluble in the developer.   Hence, the exposed part is removed by developer for a positive resist, while the unexposed part is removed for negative photoresist.
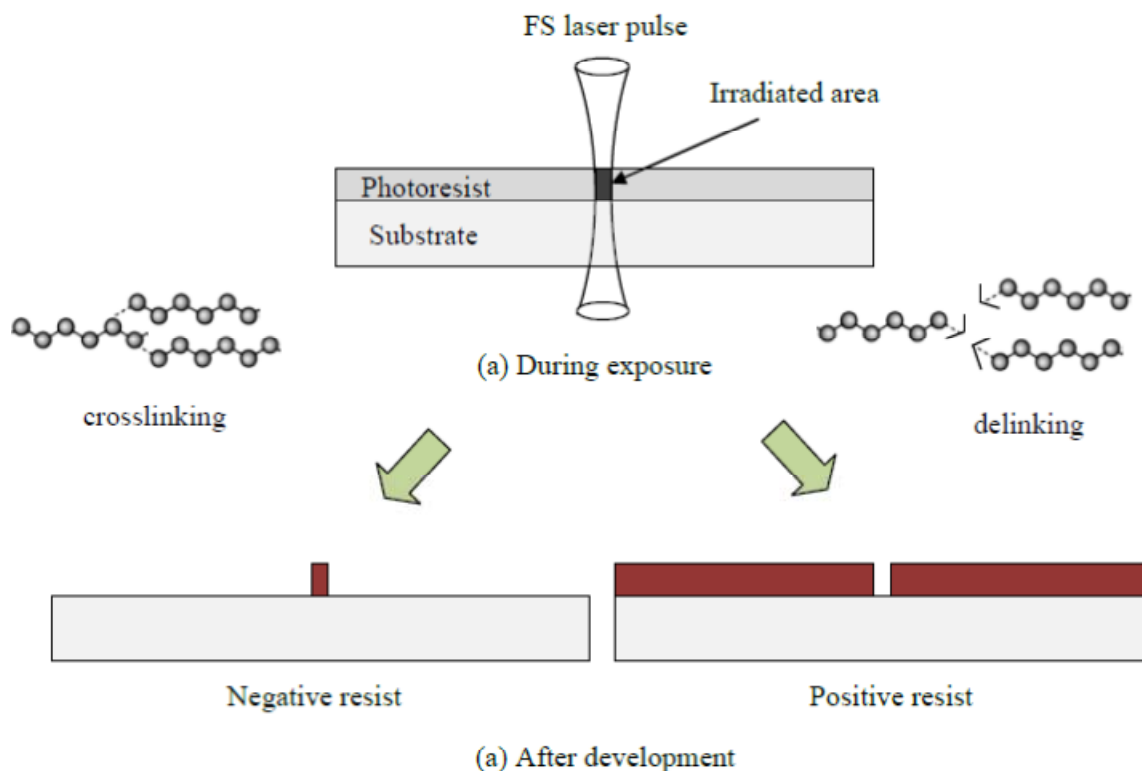
Figure 3.2 Difference in positive and negative resist polymerization.

Apart from the photochemical reaction, positive and negative photoresists are different in many other properties (see Table 3.*1*). These properties present general guidelines for choosing a suitable photoresist for a given application.

Table 3.1 Comparison of general properties of positive and negative photoresists.

Photoresistproperties	Positive resist	Negative resist
Adhesion	Average	Good
Sensitivity	Fairly low	High
Cost	Fairly expensive	Fairly low
Developer	Aqueous based	Solvent
Etch selectivity	High	Low
Swelling	No	Yes
Thermal stability	Good	Average

Only negative resists were considered for this study. Furthermore, negative resists can be sub-divided into solid and liquid phases due to its appearance during the MPA polymerization process. The solid phase resists are epoxy based and polymerized due to the cationic polymerization process. In solid phase resists, an acid is generated in the illuminated region, but the reflective index stays unchanged. Hence, the scan patterns cannot be seen during exposure. Actual crosslinking happens during the post-back process, and only after that the scan pattern becomes visible. In contrast, liquid phase resists are acrylatebased materials, which are polymerized via free-radical polymerization and are visible during exposure.

ORMOCER represents the family of originally modified ceramic materials. It is a liquid phase, arcylate based negative photoresist. ORMOCER is also classified as inorganic-organic hybrid polymers. The most important attribute of ORMOCER is that its physical and chemical properties can be tailored. Hence, they can be used for a wide verity of applications. Also, its chemical, mechanical and thermal stability along with good processing ability is an upgrade over organic polymers in most applications. ORMOCER is a biocompatible material that combines properties of organic polymers, such as, toughness and low processing temperature requirements, with inorganic materials, such as, harness, chemical and thermal stability. A type of ORMOCER used for this study was low viscosity ORMOCOMP (Micro Resist Technology). It has outstanding stability in humid atmospheres, high electrical resistance, good adhesion on most substrates and fast curing. It contains 1% of Ciba[®] Darocur TPO two photon initiator (see Figure 3.3).
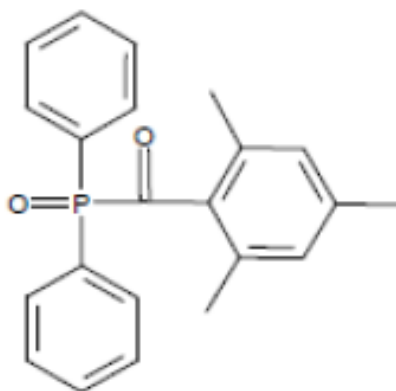
2,4,6-Trimethylbenzoyl-diphenyl-phosphineoxide

Figure 3.3 Darocur TPO structure

3.5   EXPERIMENT DETAILS

The fabrication processes proposed in this thesis is briefly explained here. The overall process flow is depicted in Figure 3.4. The four major stages are nanofiber generation, spin coating, multiphoton polymerization and development.

3.5.1   NANOFIBERS GENERATION

A three-dimensional interweaved nanofibers network is generated using femtosecond laser ablation of metallic, nonmetallic and semiconductor targets under ambient conditions. Bulk quantity of nanoparticles agglomerates and forms a fibrous nanostructure, which shows certain degree of self-assembly, consisting of crosslinked rings and bridges. The three-dimensional interweaved stricture should have better mechanical strength compared to unlinked stacked-up nanofibers.

Laser beam

Direction of motion

Silicon Wafer   Nanofibers

a. Fiber generation

Polymer

Silicon Wafer   Nanofibers

b. Spin coating with polymer

Laser beam

Polymer

Silicon Wafer   Nanofibers

c. Multi photon polymerization

Developer   Polymer

Silicon Wafer   Nanofibers

d. Developer removal to get the final shape
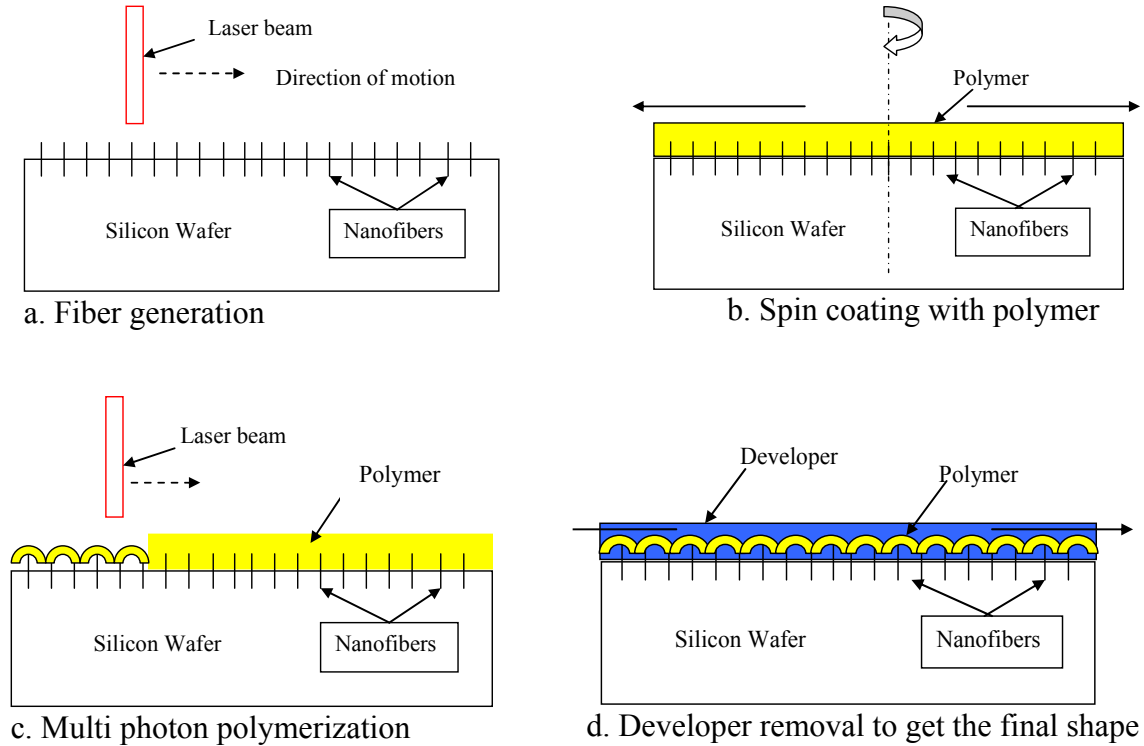
Figure 3.4 Process flow of the new mthod.

3.5.2   SPIN COATING

To obtain maximum process reliability, substrates should be clean and dry prior to applying the photoresist. Figure 3.5 is a schematic drawing, illustrating the spin coating process. Two step spin coating was carried out to achieve desired coating thickness of 0.5 μm. First, five ml of resist was carefully dispensed in the center of the substrate (see Figure 3.5 (a)) and spun for five seconds at the speed of 500 rpm with an acceleration of 100 rpm/second (see Figure 3.5 (b)). Immediately after, the sample was spun again with higher acceleration and higher speed for a few seconds (see Figure 3.5 (c)). The first step allows the resist to spread evenly using the centrifugal force. The second step was to disperse off excessive resist and to evaporate the

solvent to achieve desired coating thickness. Figure 3.6 illustrates the required spin speed of the

second step for any desired film thickness of photoresists ORMOCOMP, respectively.
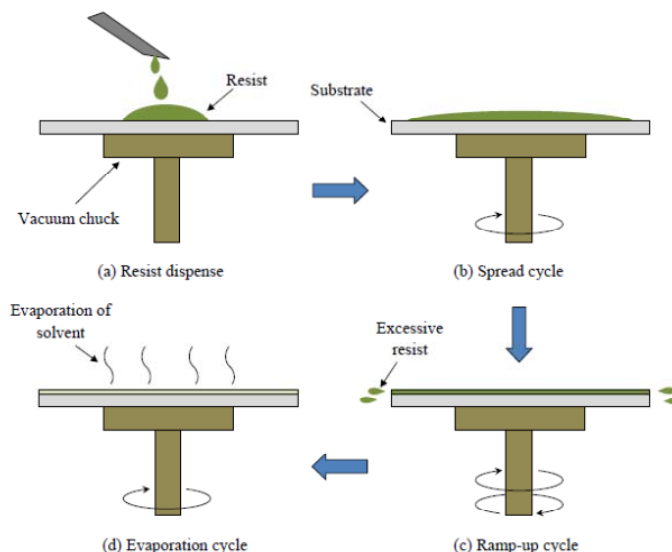
Figure 3.5 Spin coating of resist on substrate (a) resist is dispensed on substrate (b) resist is spread evenly by spinning at low speed, low acceleration (c) high speed, high acceleration to develop a uniform coating thickness and expelling excess resist (d) evaporating of solvent at final speed to obtain desired final coating thickness
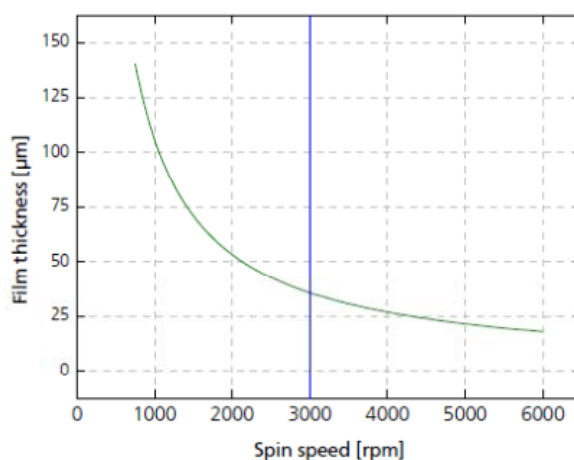
Figure 3.6 Film thickness achievable for ORMOCOMP[1]

---

[1] Source: ORMOCOMP technical data sheet.

3.5.3 MULTIPHOTON POLYMERIZATION

After coating photoresist, the substrate should be softbaked before exposing it with laser source. The purpose of pre-exposure bake is to dry out all the solvent present in the photoresist. The time and temperature for baking are specified by photoresist manufacturers. The baking can be done either in an oven or on a hot plate. Using oven may form a skin on the surface, which may inhibit in incomplete drying and may extend the baking time.

The substrate coated with ORMOCOMP was soft baked on a hot-plate for two minutes at a constant temperature of 90°C. The substrate coated with the resist then exposed under the controlled laser beam for specific geometries created by AutoCAD®.

A thin layer of resist was exposed by focusing the laser beam at the resist/glass interface. Laser parameters such as pulse energies and repetition rates, are varied to study their effects on the polymerization process. Thinner coating eliminates the need of precise control over actual position of the focal point at the resist/glass interface plane. This is critical to have good adhesion to the glass substrate. If the focal plane is inside the volume of resist, the polymerized structure does not have any base to adhere, and subsequently it will be washed-out during the development. When resist is exposed, it may go through thermal expansion and swelling depending on the pulse energy, number of pulses, and the absorption time.

All the experiments were carried out using a diode-pumped Yb-doped fiber oscillator/amplifier system capable of producing variable repetition rates from 200 kHz to 26 MHz with a central wavelength of 1030 nm and a maximum output power of 15 W at a repetition rate of 26 MHz. However, as an exposing light source, a second harmonic (515 nm) central

wavelength with variable major laser parameters such as repetition rate, pulse width and average beam power was used.

Figure 3.7 is a schematic presentation of the machine setup used to expose spin coated ORMOCER sample with a controlled laser beam. A plano-convex lens of 500 mm focal length and a plano-concave lens of 150 mm focal length were used to reduce the laser beam diameter and a λ/2 wave-plate is used in between these lenses to control the polarization of the beam. A harmonic generator was used to convert the laser beam to the second harmonic (515 nm) central wavelength. Previous work has demonstrated that second harmonic increases the efficiency and the ease with which the micromachining of the features were carried out due to the reduction in the order of MPA [105].

Another study of the ultrafast lasers ablation mechanism concluded that since the smallest diffraction-limited focus spot (given as the intensity diameter of the laser focus spot) is proportional to the laser wavelength, a smaller wavelength will result in better machining resolution [106]. The 515 nm mirrors were used to dump the 1030 nm wavelength out of the beam. Afterwards, a plano-concave lens of 75 mm focal length and a plano-convex lens of 300 mm focal length were utilized to expand the beam diameter by 4 times to 10 mm. A quarter waveplate was used to rotate the polarization state of the laser beam to circular. In addition, a diaphragm is used to improve the beam profile. Finally, the 214 fs laser beam was scanned onto the substrate surface with ORMOCER coating through a piezo tip/tilt mirror.

The spot size, also known as the beam waist, is the minimum diameter of the Gaussian beam travelling in a free space. Figure 3.8 shows a schematic diagram of the laser spot size and depth of focus for a laser beam converged by atelecentric lens.

45

1. 1030 nm Mirror
2. F = 500 mm Convex Lens
3. 1030 nm λ/2 Waveplate
4. F= -150 mm Concave Lens
5. 515 nm Harmonic Generator
6. 515 nm Mirror
7. 515 nm Mirror
8. F= -75 mm Concave Lens
9. 515 nm λ/4 Waveplate
10. F = 300 mm Convex Lens
11. 515 nm Mirror
12. Diaphragm
13. Piezo Scanner
14. EFL = 12.478 mm Telecentric Lens
15. Sample and Sample Holder
16. Computer controller
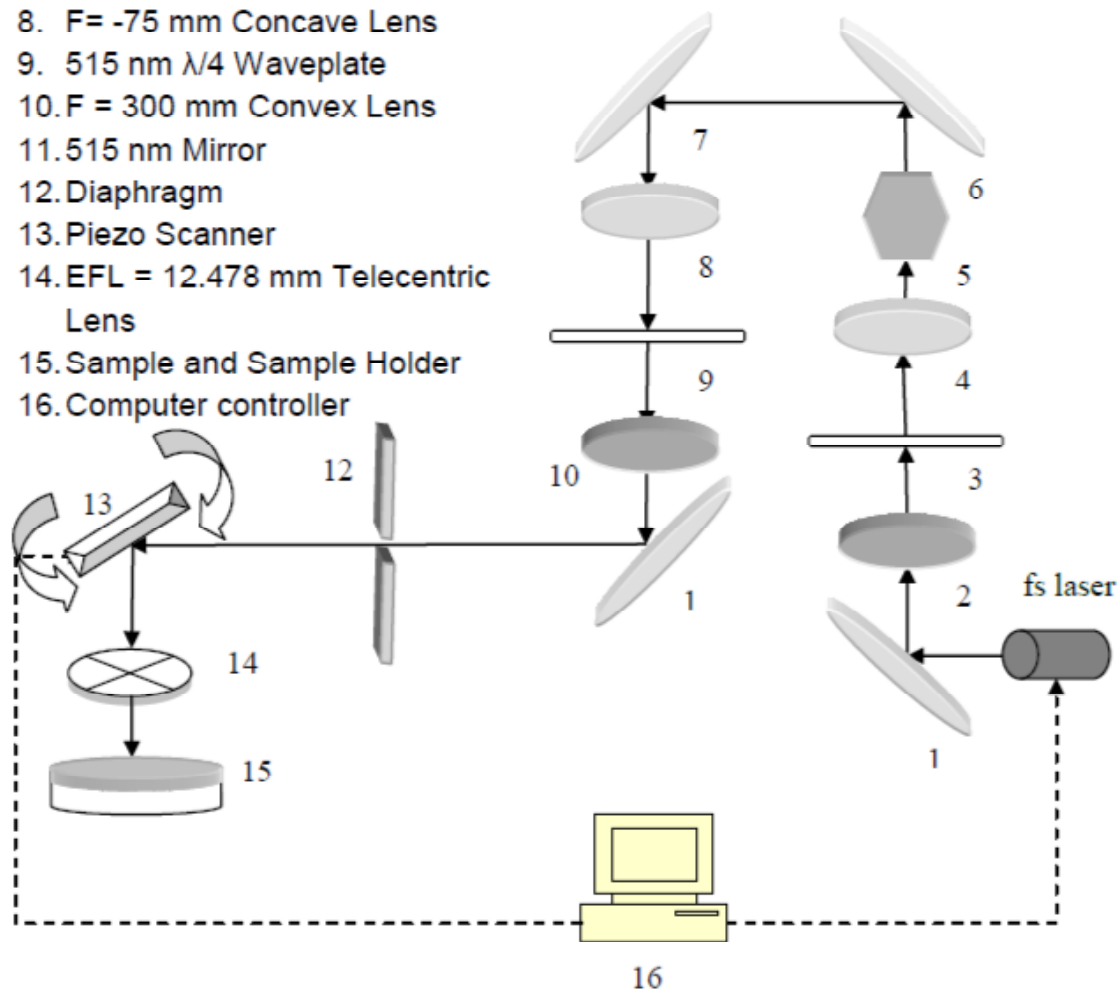
Figure 3.7 Experimental setup
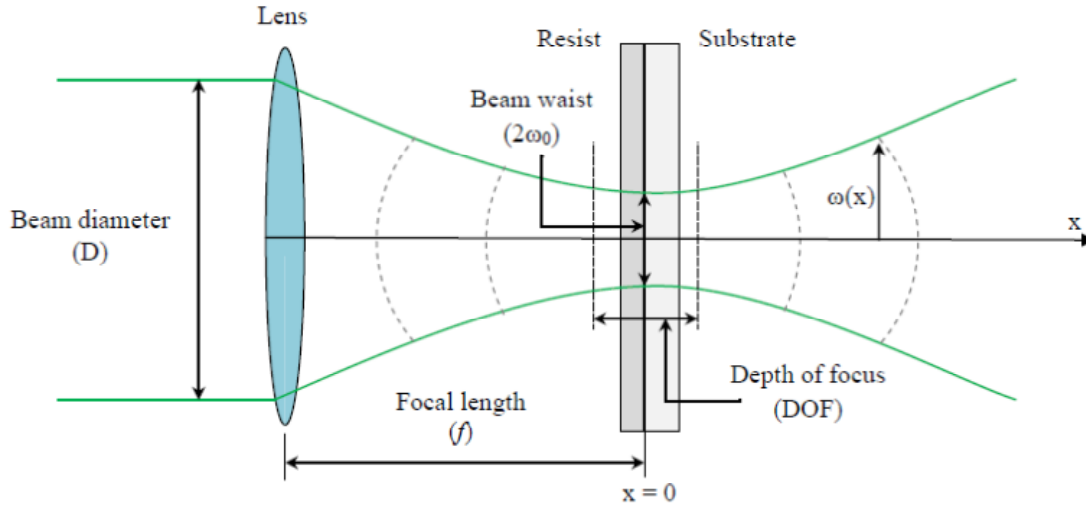
Figure 3.8 Laser spot sizeand depth of focus for converging laser beam using a telecentric lens

Telecentric scanning lenses are specially designed to make the focused beam always perpendicular to the flat focal plane regardless of the beam's position in the scan lens (see Figure 3.9). They also offer greater depth of focus and smaller spot sizes when used for laser material processing. Therefore, it is possible to focus the beam on a very thin film of resist without any precision positioning stage. Telecentric scanning lens, by the very nature of their design, maintains a near normal incidence angle of the beam to the work piece. This ensures that position errors and image distortions are minimized over the entire scan field. Having a greater depth of field and smaller spot size are important for precision laser micro-machining processes where there is a need to produce fine spot sizes while maintaining precise placement over a relatively large field.

For this study, a telecentric lens with a 12.5 mm focal length was used to focus the laser beam. In order to find the size of the focused beam spot, a single spot can be machined on a thin metal film, with pulse energy just above the material threshold. The size of the machined spot,

measured using a Scanning Electron Microscope (SEM), gives the size of the focused beam spot.

The theoretical laser spot size ($2\omega_0$) can be calculated using [107]:
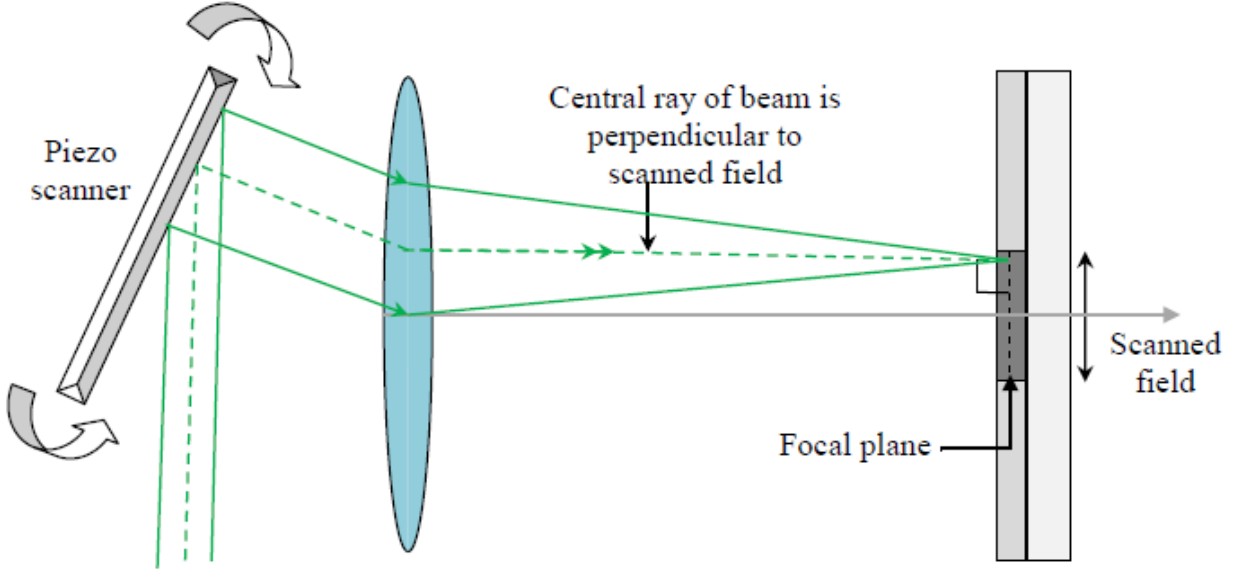
Figure 3.9 Telecentric scanning lens.

$$2\omega_0 \approx 1.27\frac{\lambda_0 f}{D} \tag{1.1}$$

Here, f is the effective focal length of the telecentric lens, λ_o is the wavelength of the laser and D is the laser beam diameter. Values for these parameters are 12.5 mm, 515 nm and 8 mm, respectively. Hence, the theoretical spot size diameter was calculated to be 1.02 μm. Generally, smaller spot size results in higher photon flux, as a result, TPA probability increases with smaller spot size. The depth of focus (*DOF*) is calculated to be 3.19 μm using:

$$DOF = \left(\frac{8\lambda_0}{\pi}\right)\left(\frac{f}{D}\right)^2 \tag{1.2}$$

After exposure, the substrate was hard-baked on a hot-plate at the constant temperature of 95°C for two minutes. The polymerized ORMOCOMP cure and harden during the post-exposure bake.

3.5.4   DEVELOPMENT

Once the substrate was cooled, it was immersed in developer solution for approximately two minutes at room temperature to remove unpolymerized and unhardened resist. The developer solution used for ORMOCOMP was ORMODEV (Micro Resist Technology.

Finally, the microstructures formed by MPA polymerization were observed under Scanning Electron Microscope (SEM). Most of results that can be obtained in atmospheric conditions can be further improved by using clean-room facilities. However due to the associated cost and setup requirements, all experiments were carried out in ambient atmosphere settings.

3.6   SUMMARY

The knowledge of laser systems and characteristics of laser beam is necessary in order to verify the capability of the system for MPA polymerization. This also determines the proper selection of the substrate material and the photoresist. Finally, the experimental parameters must be defined. In using femtosecond lasers as an alternative for polymerizing a photoresist to fabricate microstructures, laser parameters including wavelength, repetition rate, pulse width, pulse energy, and scan speed must be analyzed to satisfy the requirements of specific tasks, stabilize the process and to maximize the efficiency of laser power usage. Table 3.*2* and Table 3.*3* summarize the selected parameters and their effect on the feature and the process.

Table 3.2 Laser parameters effects

Laser parameters		Effects
Power output	(40mW – 1W)	Throughput
Wavelength	(515 nm)	Feature size
Pulse energy	(5 – 50 nJ/pulse)	Feature quality
Pulse width	(214 fs – 3.57 ps)	Feature quality
Repetition rate	(4 – 26 MHz)	Feature controllability
Spot diameter	(1.02 μm)	Feature size & shape

Table 3.3 Process parameters effects

Process parameters	Effects
Prebake	Adhesion to substrate
Spin coating thickness	Feature size, aspect ratio
Postbake	Shrinkage, resolution
Scan speed	Feature quality, linearity, throughput

For each exposure (i.e. constant pulse energy, repetition rate and scan speed) an array of microstructures were created. The dimension of each microstructure within the array was measured and the mean values are reported in each of the studies.

CHAPTER 4

REINFORCED POLYMER MICROSTRUCTURE

FABRICATION PROCESS

This chapter describes a direct fabrication of reinforced polymer microfeatures using multiphoton polymerization of nanofiber dispersed polymer resin. The femtosecond laser is used both for the generation of three-dimensional interweaved nanofiber and for the construction of microfeatures, like microchannels and voxels. A numerical method which combines finite difference and Ruge-Kutta- 4 method were used to numerically simulate the temperature distribution on the substrate surface when it is irradiated by a laser beam. The model was use to analyze the effect of the temperature on the generation of nanoparticles that agglomerate to produce nanofibers and nanospheres of Titanium oxide using femtosecond laser ablation at ambient conditions. Finally, the Plasmon effect of nanofibers on the size of the generated polymer microstructures is discussed.

4.1   GENERATION OF NANOSTRUCTURES USING LASER ABLATION

As the laser beam hits the material surface, some of the photons are absorbed by the electrons in the conduction band. Photon energy in the laser beam is transferred to the electrons. As a result of this, the kinetic energy of the surface electrons increases. Electrons gaining energy from the laser beam via absorption make successive collisions with the lattice molecules and excite lattice phonons to higher energies [108-111]. Thus, molecules have increased vibration energies, i.e. eventually have higher temperatures. It is very important to compute the temperature of the

material which evaporates at the surface in laser surface treatments as the rate at which the material is removed depends on the evaporation, particularly at the surface. However, accurate computing of surface temperature is difficult to obtain. Using the Fourier equation for determining the temperature distribution in higher intensities results in significant error due to the assumptions made in boundary conditions in the theory [112].

Some assumptions are made for simplicity in the solution of the problem. These assumptions include: Energy losses due to thermionic emission can be neglected. Laser beam spot is assumed to be circular in shape and the physical change of laser beam due to optical system and plasma is negligible. The input heat flux due to laser irradiation is treated as an internal heat generation in the powder layer. The heat flux from laser beam is taken as Gaussian distributes heat flux and given directly to the top of the powder layer. The irradiated layer is assumed to be subjected to plane stress type of temperature variation because the thickness of the irradiated layer is very small. The effective thermal conductivity of the powder layer is used in the calculation, which incorporates solid thermal conductivity, thermal conductivity of the surrounding environment. The temperature variation is governed by following thermal heat diffusion equation with internal heat generation [113];

$$\rho C_p(T)\frac{\partial T}{\partial t} = \nabla(k_e \nabla T) + Q_g \tag{4.1}$$

Where ρ is the density of the irradiated substrate, T is temperature, t is time, Q_g internal heat generated due to laser irradiation, ke is the effective temperature-dependent solid thermal conductivity, and $C_p(T)$ is specific heat. Considering enthalpy before and after phase change when the temperature of the material exceeds the melting point, the latent heat of melting is incorporated to get modified specific heat [114]:

$$C_l = C_p + \frac{L_m}{2\Delta T} \quad for \ T_m - \Delta T \le T \le T_m + \Delta T \tag{4.2}$$

Where T_m is the melting temperature (1795 $^{\circ}$C for titanium) and L_m is the latent heat of melting. Equation (4.2) can be written as;

$$C_l = C_p + \frac{L_v}{2\Delta T} \ \ for \ T_v - \Delta T \leq T \leq T_v + \Delta T \tag{4.3}$$

Where T_v is the boiling temperature (3287 $^{\circ}$C for titanium)) and L_v is the latent heat of boiling. In the present model, Gaussian heat flux distribution is taken the same as laser intensity. If the laser input power P and laser beam radius R are known, then the laser intensity I(r) at a distance r from the center of the laser beam is given by [112];

$$I(r) = I_o e^{-4.5(^r/_R)^2} \tag{4.4}$$

The above represents the input heat flux from the laser beam, given to the substrate surface. Hence, equation 4.4 can be written as [112];

$$q(r) = q_o e^{-4.5(^r/_R)^2} \tag{4.5}$$

Here, q(r) is the input heat flux at a distance r from laser beam center, qo is the laser heat flux at the center of the laser beam. The radius of the laser beam R can be calculated using $D_o=1.27\lambda_o f/D$ [32], where D_o is the theoretical laser spot diameter, f is the effective focal length of the telecentric lens, λ_o is the wavelength of the laser beam and D is the laser beam diameter. Values for these parameters were 52.5 mm, 1040 nm and 8 mm, respectively. Hence, the theoretical spot size diameter was calculated to be 8.67 μm and hence $R=D_o/2=4.34$ μm. This incoming heat flux is treated as internal heat generation in the substrate. Hence, quantity of heat generation (W/m^3) can be written as [112];

$$Q_g = \frac{q(r)}{S} \tag{4.6}$$

S, is the thickness of the first layer of the substrate. Equation (4.1) can be re-written as;

$$\rho C_p(T)\frac{dT}{dt} = \nabla(k_e \nabla T) + Q_g \tag{4.7}$$

The above equation can be written for each node in the effected zone. This generates a system of differential equations in the variable T as a function of time t. The formulation is used for the development of finite difference- Ruge-Kutta 4 codes in Matlab 7 which are illustrated in Appendix A. To check the accuracy of present model for the determination of temperature distribution, the temperature distribution on the top surface of substrate is determined, and then compared with experimental results of Fischer et al. [115] as well as with numerical results of Kolossov et al. [116]. The results are consistent with those obtained by Fischer et al., [115] and Kolossov et al. [116] where the present model is used with same conditions as the references mentioned.

Figure 4.1(a) shows three dimensional temperature distribution simulations of the Titanium substrate top surface (20 μm by 20 μm) irradiated with a laser beam at 13 MHz repetition rate and a power of 16 W for 10 ms dwell time. The material properties and other data are obtained from ref [116]. This figure shows that the maximum surface temperature (10248 $^{\circ}$C) is observed at the center of the laser beam which is way above the boiling temperature of titanium. Figure 4.1 (b) shows the contour plot of isotherms at the top surface of the area irradiated sample.

Three zones can be realized in this figure, the first one which located in the middle of the laser beam where the temperatures are above boiling temperature. In this zone (just inside the 3000 $^{\circ}$C isotherm line) the titanium phase changes from solid to gas instantaneously. The second zone is the melting area where the titanium changes its phase from solid to liquid. This zone is located between the 3000 $^{\circ}$C and just outside the 2000 $^{\circ}$C isotherm lines. The third zone where the titanium stays solid is located in the area outside then 2000 $^{\circ}$C isotherm line.
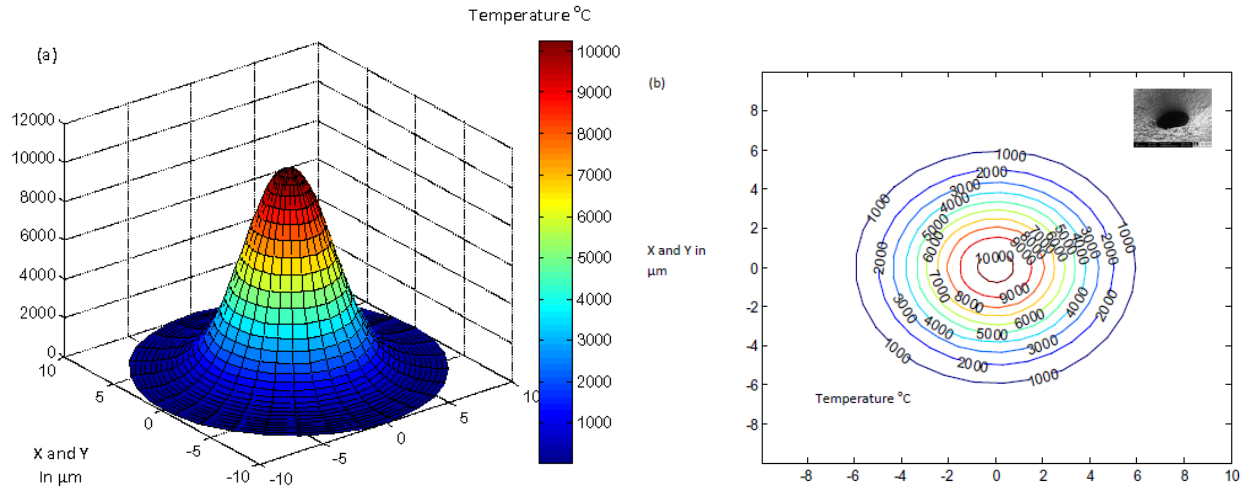
Figure 4.1 Simulation of temperature distribution of titanium sample top surface irradiated with laser beam. (a) Surface plot, (b) contour plot.

Figure 4.2 shows the effect of laser power on temperature distribution along X-axis on the top surface of the titanium substrate due to irradiation of laser beam. Laser power is changed between 4W and 16W with 4W increment. The nature of temperature distribution graph shows that there is an increase in temperature with increase in laser power. Temperature gradient along X-axis (or Y-axis) increases with the increase of laser power which results the rapid increase in temperature within 214 fs. The temperature gradually decreases on both sides of laser center.

Figure 4.3(a, b, c and d) shows the SEM image of the Ti substrate irradiated with femtosecond laser of 1040 nm wavelength, 13 MHz repetition rate and a power of 16, 12, 8 and 4 W, respectively. The process was done in the air under ambient conditions. The nanostructures Shown in figure 4.3 were generated as a result of nanoparticle agglomeration. There are two kinds nanostructures co-exist: the weblike fibrous nanostructure and microspheres. It is found that weblike nanofibrous structures were generated with mean (or average?) particle size of approximately 40 nm, as shown in Figure 4.3(a). Microspheres of approximately 50-1000 nm diameters were generated at laser powers of 12, 8 and 4 as shown in Figure 4.3(b, c, and d).
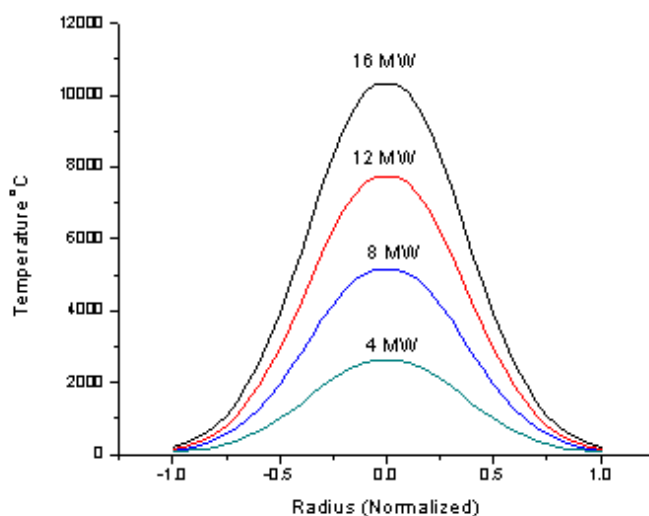
Figure 4.2 Variations of temperature, within different laser power in the titanium sample.

Figure 4.4 (a and b) shows the energy-dispersive X-ray (EDX) analysis of the non-irradiated and irradiated Ti samples. A significant change in the weight percentage of O and Ti is detected before and after irradiation by the femtosecond laser as illustrated in figure 4.4 (a and b) respectively.

X-ray diffractograms of untreated and laser-irradiated samples are presented in figure 4.5. The diffraction peaks can be indexed to metallic Ti and its oxides The peaks $27.5°$, $36.04°$, $54.34°$, $56.62°$ and $69.1°$ can be attributed to different diffraction planes of rutile TiO_2 [114, 115]. The peaks $36.9°$, $40.57°$, $43.1°$, $62.25°$ and $74.7°$ can be indexed to TiO as shown in Figure 4.5. Micro-Raman spectra, shows the presence of rutile TiO_2 in titanium nanoparticle aggregate as shown in Figure 4.6. The peaks at 244, 441.8 and 610 cm^{-1} are attributed to the thermodynamically stable rutile phase of TiO_2 [116].

The physical processes responsible for surface modifications are not always fully understood because of the complicated laser-plasma-surface interactions. Venkatakrishnan et al demonstrated the formation of nanoaggregates and nanostructuring of the surface of silicon

[111]. The surface modifications, in particular the main crystalline phases formed (oxide), are found to depend on the lasers characteristics [117,118]. The chemical analyses of a laser irradiated steel surface showed that the surface is a multilayer structure [119, 120]. It was also found that high temperature favors the formation of nanofibers while low temperature favors the formation of plate-like shapes [120, 121].

The formation of two distinct types of nano-micro structure reflects two kinds of ablation mechanisms of femtosecond laser ablation, one is the phase explosion and the other is hydrodynamic effect [122]. In the first mechanism, the energy of the femtosecond laser is delivered into the material in a short time scale that absorption occurs at nearly solid-state density. The energy is first deposited in the electronic subsystem within a layer of thickness of tens of nanometer. When the density of the free electrons exceeds a certain threshold, enough energy is absorbed to produce macroscopic ablation. The ionized material is removed away from the surface in the form of expanding high pressure plasma.

The plasma remains confined close to the specimen surface at atmospheric pressure. Condensation of vapor in the plume lead to the generation of nanoparticles and their aggregate and will be deposited on the surface of the specimen to form nanofibers as shown in figure 4.3(a) [18]. The other mechanism that becomes observable is the hydrodynamic effects [123, 124]. In this mechanism, resolidified droplets of materials form nanostructures like nanosphere as shown in figure 4.3(b, c and d).

Studies showed that thermal oxidation occurs if the irradiated material is not directly ablated [122]. Due to the series of laser pulses, oxidation probably occurs dynamically between the subsequent pulses until a steady-state regime between modification (energy transfer,
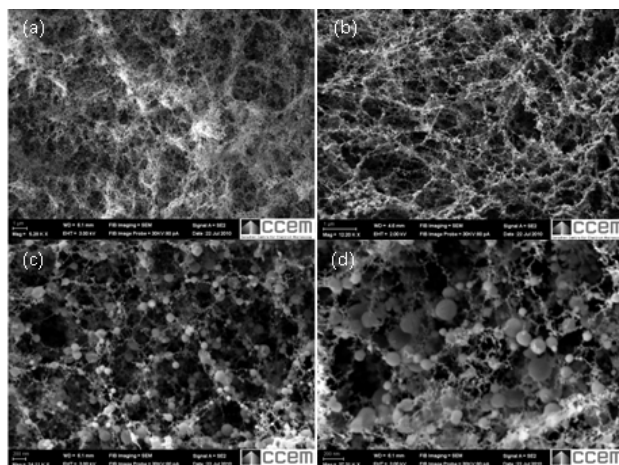
Figure 4.3 SEM micrographs of nanofibrous structure, on femtosecond laser-irradiated Titanium. (a) 16W, (b) 12W, (c) 8W, and (d) 4W.
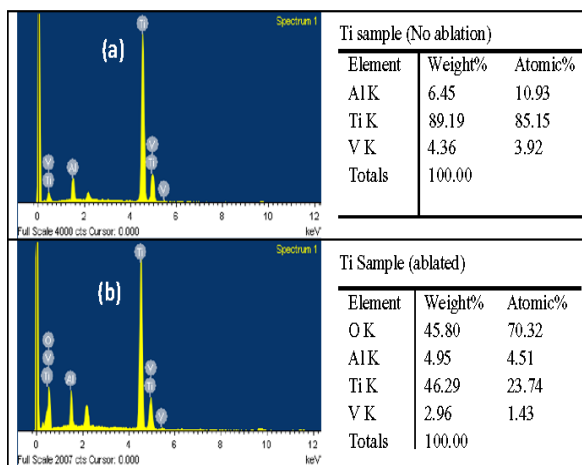
Figure 4.4 EDX analysis of nanofibrous structure and nanoparts. (a) Pure Ti, and (b) Laser-irradiated Ti.
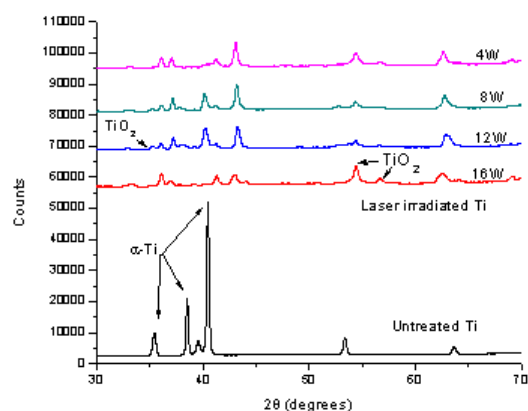
Figure 4.5 X-ray diffractograms of laser-irradiated Ti.
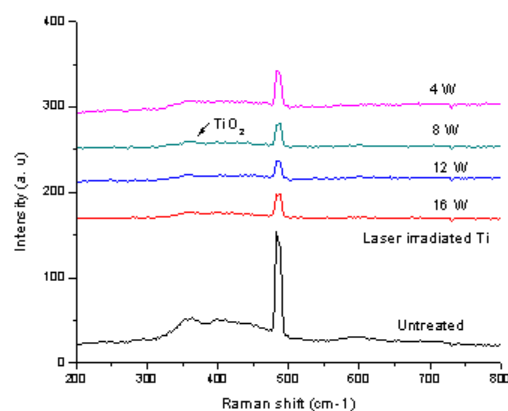
Figure 4.6 Micro-Raman spectra of laser-irradiated Ti

Oxidation and ablation (oxide/material removal) is established [122]. Figure 4.4 shows that the atomic ratio of Ti to O is almost 0.5 which indicates the presence of Ti and Ti oxide nanofibers in the microstructures [125]. Also, we believe that the hydrodynamic effect is responsible for formation of nanospheres and nanodiscs while ablation effect is responsible for the formation of nanofibers because the temperature in the hydrodynamic stage would be less than the

58

temperature in the ablation stage. Therefore, zones of irradiated Titanium sample that has temperatures between 1795 ^{o}C (melting point) and 3287 ^{o}C (boiling point) form nanospheres while those parts of Titanium sample with temperatures above 3287 ^{o}C show nanofibers formation (figure 4.3).

The oxidation also explains the need of a few incubation pulses (leading to the first material modification) until significant material ablation takes place. The minimum laser radiation energy density required for creating detectable damage on the implant target is called the damage threshold. Assuming a perfectly Gaussian shaped spatial beam profile in the experiment, the surface damage threshold of the material can be derived on the basis of the equation [126];

$$\emptyset_{th}(N) = \emptyset_{th}(1)N^{\epsilon-1}, \tag{4.8}$$

Where Φth (N) is the multi pulse damage threshold fluence, $\Phi th(1)$) is the single pulse damage threshold fluence and ε characterizes the degree of incubation, i.e. the dependence of the threshold fluence on the number of pulses N which can be expressed as N= r.t, where r is the repetition rate and t is the dwell time. Since the relationship between $\ln(\emptyset_{th}(N))$ and ϵ is linear, we can write the following;

$$\epsilon = 1 + \frac{\ln[\emptyset_{th}(N_2)/\emptyset_{th}(N_1)]}{\ln [N_2/N_1]}; \tag{4.9}$$

Where $\emptyset_{th}(N_1)$ and $\emptyset_{th}(N_2)$ are the damage threshold fluencies at N_1 and N_2 laser pulses respectively. It was found that at N_1=100 and N_2=1000 pulses, the damage threshold fluences was 0.34 and 0.24 J/cm^2, respectively. Thus the value of ε is 0.85 and the single pulse damage threshold fluence is 0.68 J/cm^2, which leads to the following general relation;

$$\emptyset_{th}(r, t) = 0.68(r.t)^{-0.15}; \tag{4.10}$$

So for r =13 MHz and t =0.1 ms, the damage threshold fluence ($\emptyset_{th}(N = 1300)$) is 0.23 J/cm². The decrease in the surface damage threshold fluencies and hence the surface temperature with the increase in number of laser pulses may attribute because of damage accumulation effect which already has been reported for other materials [127, 128]. Therefore, the number of pulses of the femtosecond laser has a direct impact on the type of the generated nanostructure. This theory supports the results obtained through the experimental work.

4.2   FABRICATION OF REINFORCED POLYMER MICROSTRUCTURES

Figure 4.7 shows an example of microfeatures generated by the described method while the SEM image in Figure 4.8 shows an array of micro voxels formed after laser irradiation of nanofiber dispersed Ormocer at a repetition rate of 26 MHz, a power of 90 mW and a point-to-point scan with a dwell time of 150 msec. The image shows that the average diameter of the voxels is around 15 µm, which is much bigger than the laser spot size.

Since chemical reaction of cross-linking occurs only where molecules have absorbed two photons, the polymerization threshold is sharply defined. Therefore, polymerization only occurs at around the peak of the laser spot where the intensity is high enough to induce 2PP. For this reason, 2PP is capable of overcome diffraction limit and produce voxel far smaller than the laser spot. However, this is not the case in nanofiber reinforced polymerization. Nanofibers significantly enlarge the generated voxel size. The voxel diameter *d* of pure polymer can be estimated by the following equation [129];

$$d(N_o,t) = r_o \left[\ln\left(\frac{\sigma_2 N_o^2 n \tau_L}{C} \right) \right]^{1/2} \quad , \tag{4.11}$$
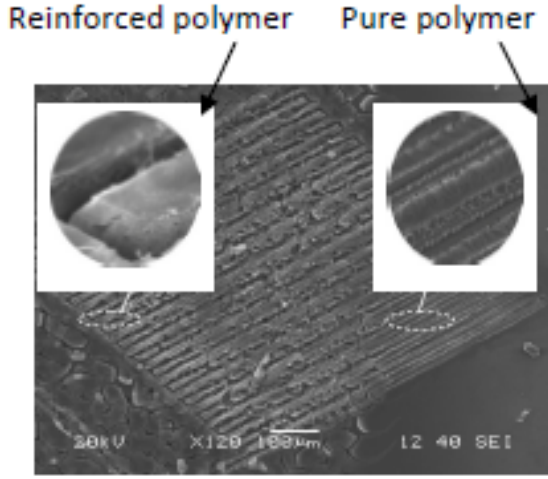
Figure 4.7 SEM Images of the generated microfeatures using the new method.
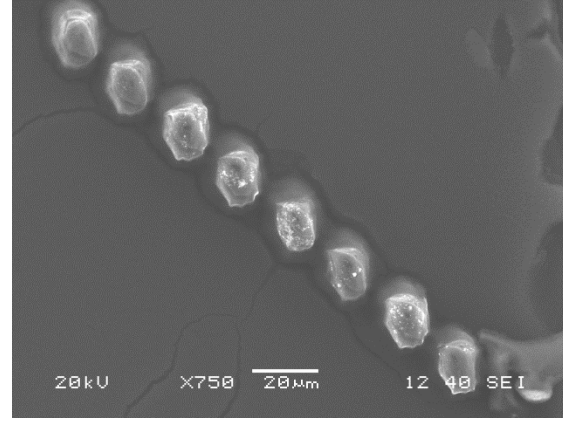
Figure 4.8 SEM image of the voxel array generated by 2PP method.

Where $n = vt$ is the number of pulses, v is the laser pulse repetition rate, t is the exposure time, τ_L is the laser pulse duration, σ_2 is the effective two photon cross section for the generation of radical, and N_o is the constant of photon flux and is given by [129];

$$N_o = \frac{2}{\pi r_o^2 \tau_L} \frac{PT}{vh\omega_L} \qquad , \qquad (4.12)$$

Where r_o is the laser spot size radius, ω_L is the frequency of laser light, T is the fraction of light transmitted through the objective and h is Planck's constant. The value of C is given by [129];

$$C = \ln[\rho_o(\rho_o - \rho_{th})] \qquad\qquad (4.13)$$

Where ρ_o primary initiator particle density and ρ_{th} is the minimum density of radical to allow polymerization happening (threshold value). Voxel size without reinforcement was calculated and plotted in Figure 4.9 for the applied laser energy at a constant irradiation time of 150 ms

and a constant power of 90 mW. The theoretical estimate of the voxel diameter at 90 mW is about 900 nm. However, Figure 4.8 shows the actual voxel is 15 times larger than the predicted diameter. Other experiment results obtained with the same laser parameters and without the dispersed nanofibers, show a special resolution of 2 μm, which is very close to the theoretical voxel diameter. The diameters of nanofibers are about 40 nm, which is a magnitude order smaller than the wavelength of the laser [130]. Therefore, the plasmonic effect of nanofibers could be the main attribution to the enlargement of the voxel volume.
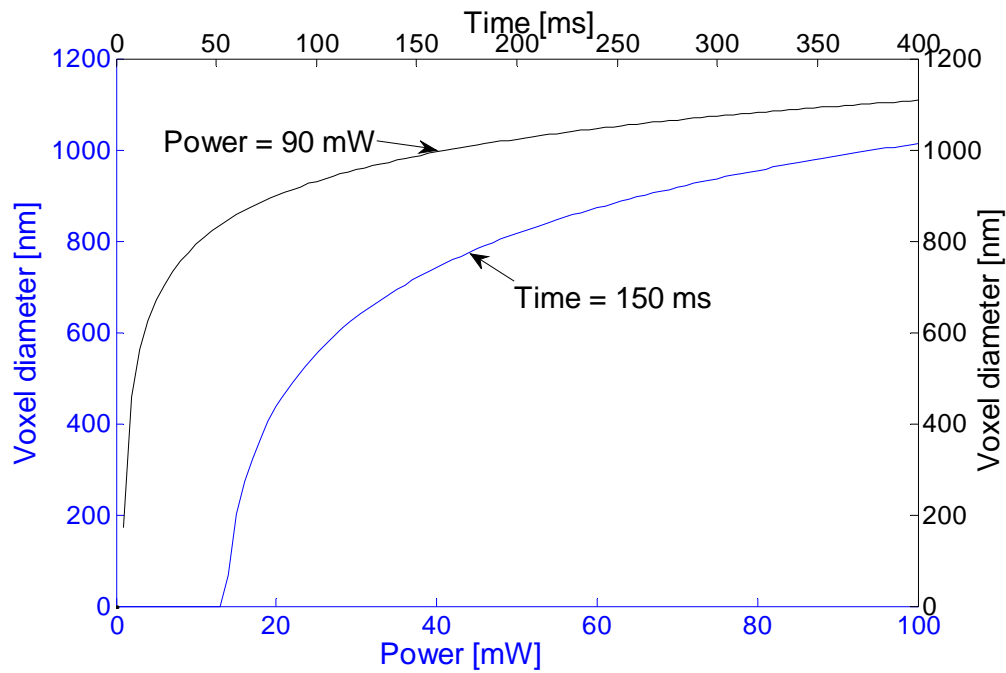
Figure 4.9 Theoretical voxel diameter variations.

When a small metallic nanofiber is irradiated by light, the oscillating electric field causes the electrons to oscillate coherently, as shown schematically in Figure 4.10 [131]. When the electron cloud is displaced relative to the nuclei, a restoring force arises from Coulomb attraction between electrons and nuclei that results in oscillation of the electron cloud relative to the

nuclear framework. The collective oscillation of the electrons is called the dipole Plasmon resonance of the particle (sometimes denoted "dipole particle Plasmon resonance" to distinguish from plasmon excitation that can occur in bulk metal or metal surfaces). For particles small with respect to the incident radiation wavelength, retardation effects are negligible. The Mie theory then predicts cross-sections for absorption and scattering of a particle of radius r as follows [132],

$$C_{abs}(\lambda) = \frac{\pi^2 N_m d^3}{\lambda} \; Im\left(\frac{\varepsilon - \varepsilon_m}{\varepsilon + 2\varepsilon_m}\right), \tag{4.14}$$

$$C_{sca}(\lambda) = \frac{2\pi^2 N_m d^3}{3\lambda} \left|\frac{\varepsilon - \varepsilon_m}{\varepsilon + 2\varepsilon_m}\right|^2, \tag{4.15}$$

Where d is the particle diameter, ε is the permittivity of the particle, ε_m is the permittivity of the medium, λ is the incident radiation wavelength, and N_m is the number of molecules per unit volume at standard temperature and pressure. Figure 4.11 shows values of C_{sca} computed as a function of particle diameter for silicon nanoparticles combined with values for the dielectric function ε obtained from the published literature [133]. All values are computed at the Fröhlich frequency in ORMOCER. C_{sca} becomes dominant for silicon at 1030 nm laser wavelength. Thus, it is expected to be advantageous for 2PP structures to employ particles in this size regime as we are going to see later. However, it is also necessary to avoid particles that are substantially larger in size (100 nm or more in diameter) by increasing laser repetition rate as such large particles typically suffer from the presence of multiple nearly degenerate modes that reduce the strength of the fundamental nanofiber Plasmon effect [132].
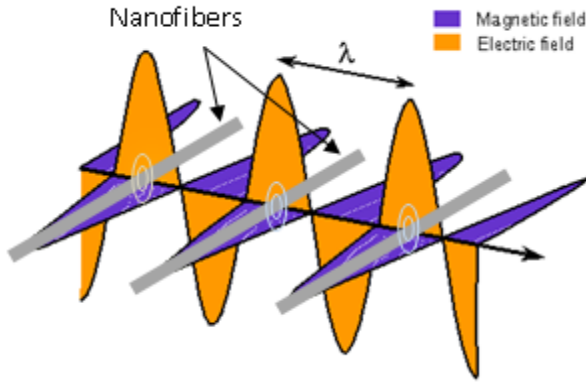
Figure 4.10 Schematic of plasmon oscillation for nanofibers.
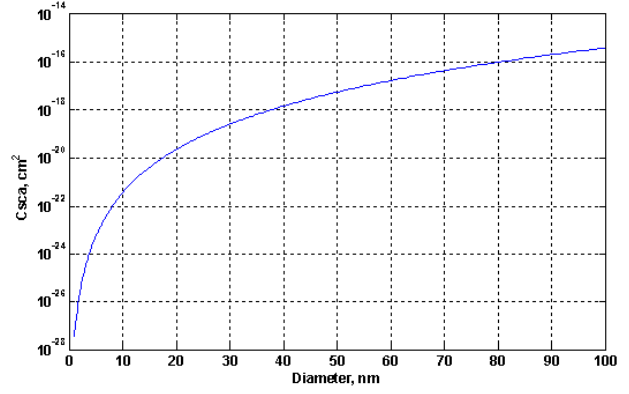
Figure 4.11 Computed values for scattering cross-section for silicon nanoparticles in Ormocer as a function of particle diameter.

The effective two-photon cross section of Ormocer for the generation of radicals is 3×10^{-55} [134]. This value is relatively small. Much higher two-photon sensitivity can be obtained with a two-photon absorption cross section σ_2 in the range 10^{-50} to 10^{-47} [135]. This effective cross section is dramatically increased by adding the nanofibers and for the case of silicon nanofibers with incident radiation wavelength of 1030 nm, the value of σ_2 increases to about 10^{-40}. Thus, the diameter of the voxel increases dramatically with dispersing nanofibers in the Ormocer. For the same irradiate laser energy as shown in figure 5, which indicate that one can get the required feature size for almost 10 times less laser energy, by dispersing silicon nanofibers in the polymer resin. From the definition of the effective two-photon absorption cross section [136] and using the particle scattering cross section as one photon absorption cross section, we can write;

$$\sigma_2 = C_{sca}^2 . \tau_l \qquad \forall \, d < \lambda, \tag{4.16}$$

Using MiePlot v4, figure 4.13 shows a plot of two-photon cross section of Ormocer with diameter of dispersed silicon nanofibers at 1030 fs laser wavelength, which comply with the obtained experimental results.
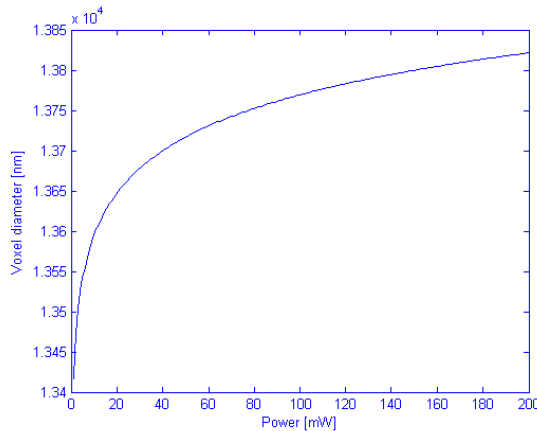
Figure 4.12 Voxel diameter variations with laser power for reinforced polymer at 26 MHz repetition rate.
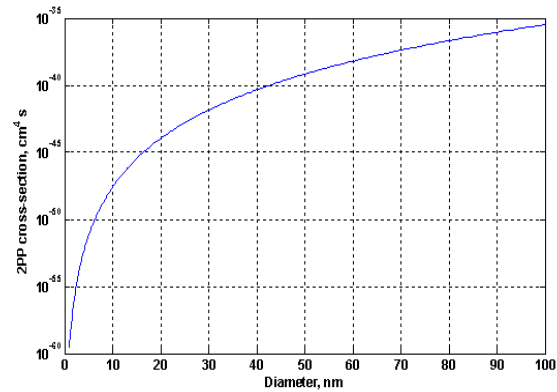
Figure 4.13 Effect of silicon nanofiber size on 2PP cross section for Ormocer at 1040 nm wavelength.

As the energy of the laser beam increases to above the polymerization threshold, the center of the laser pulse ablates the polymer and the polymerization threshold boundary move to the lower intensity of the Gaussian beam, as illustrated in Figure 4.14. The SEM image in Figure 4.15 shows a reinforced channel produced at a repetition rate of 13 MHz, a laser power of 250 mW and a continuous scan at a speed of 300 mm/sec. The ablation removes the polymer from the central part while the two photon polymerization process cures the shoulders of the produced channel. The result is a channel, of which the width depends on the laser power [137]. Increasing the energy will push the polymer ablation threshold boundary to the outmost edge of the Gaussian beam, as shown in Figure 4.14 which means that the polymer will be ablated totally to the wafer surface level.

EDX was conducted on the sample shown in Figure 4.16 to analyze the composition of the generated microfeatures. Both pure polymer features and nanofiber-reinforced features were tested. The result shown in Figure 4.16 confirmed the presence of silicon nanofibers in the reinforced polymer matrix. Compared with pure polymer features, the nanofiber reinforced feature contains higher level of oxygen and lower level of silicon. During ablation process, the

65

temperature of the exposed silicon increases to a very high level which not only causes the silicon to evaporate, but also to oxidize which normally happens between 800 - 1200 ^{o}C. The atomic ratio of Si to O was found to be almost 0.5 in the "reinforced" polymer which indicates the presence of silicon and silicon oxide nanofibers in the polymer matrix [138, 139].
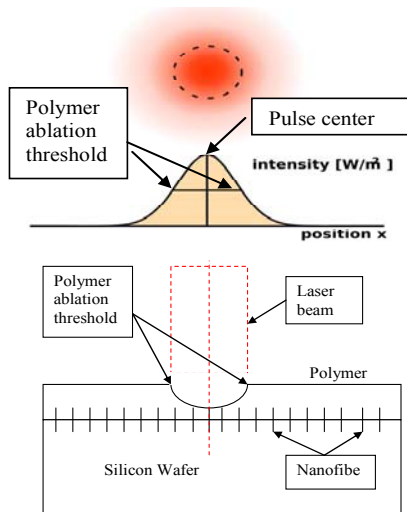
Figure 4.14 Two photon polymarization/ ablation of the reinforced polymer.
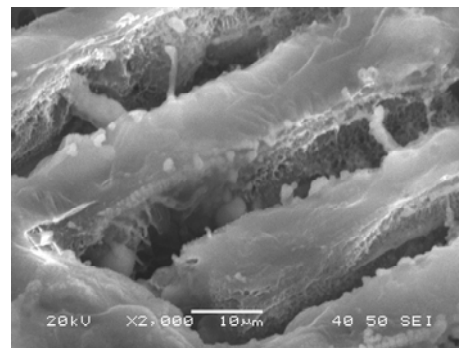
Figure 4.15 SEM image of the reinforced channel at 13 MHz. and 250 mW.
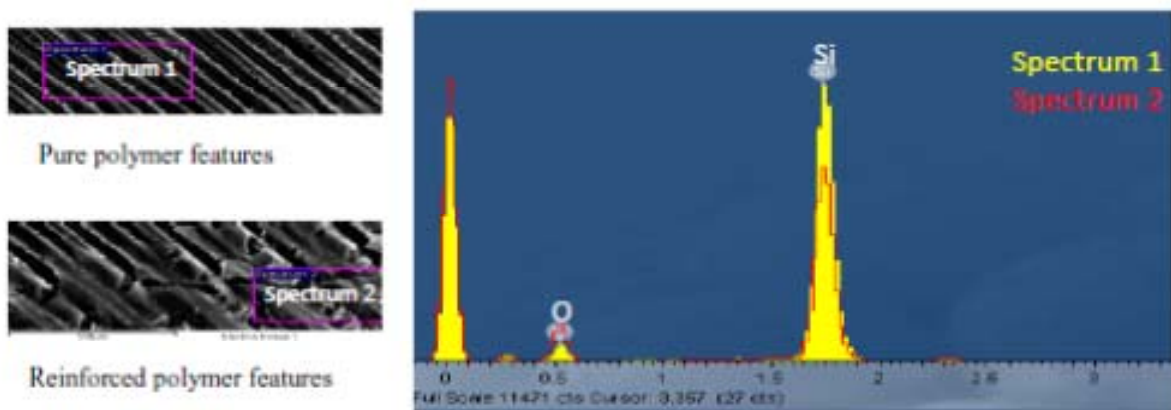
Figure 4.16 EDX measurements of both pure polymer and reinforced polymer.

4.3 DUAL-WAVELENGTH PHOTON POLYMERIZATION FOR REINFORCED MICROSTRUCTURES

So far, two photon polymerization has been conducted with a femtosecond laser beam of a single wavelength. In this research, a dual-wavelength induced multi- photon polymerization was experimented with in an attempt to compensate for the voxel enlargement caused by nanostructure scattering of the laser beam. The experimental result showed that spatial resolution of voxels can be improved with two-wavelength polymerization. A numerical analysis has been conducted to compare the voxel size with single-photon, two-photon and dual-wavelength multi photon polymerization.

4.3.1 SINGLE PHOTON ABSORPTION

Let us first consider the single photon polymerization (1PA) process for ORMOCER irradiated with femtosecond laser at 365 nm wavelength. A photoinitiator of 2-benzyl-2-dimethylamino-40-morphol inobutyrophenone (IRGACURE 369, Ciba-Geigy) has been used in the hybrid polymer resin. This initiator forms radicals upon UV irradiation, thus further initiating a radical chain polymerization process [140]. Under the assumption of a homogeneous distribution of the initiator molecules in the resin, photo-chemically induced cross-linking is started at each point where a radical is formed [141], thus supplying the reactive species (both parts of the UV initiator are actually photo-chemically active) for further polymerization of the resin until the reaction is terminated.

The wavelength of maximum absorption depends on the presence of particular chromophores (light-absorbing groups) in a molecule. The absorbance (A) varies linearly with

both the path length (z) and the analyte concentration (c). These two relationships can be combined to yield a general equation called Beer's Law [142];

$$A = \varepsilon\, z\, c \tag{4.17}$$

The quantity ε is the molar absorptivity; in older literature it is sometimes called the extinction coefficient. The molar absorptivity varies with the wavelength of light used in the measurement. The molar absorptivity (expressed in units of L mol^{-1} cm^{-1}) is directly related to the single photon absorption cross section $\sigma 1$ (in units of cm^2) via the Avogadro constant (N_A) [143]:

$$\sigma_1 = 1000\ln(10)\frac{\varepsilon}{N_A} = 3.82 \times 10^{-21}\varepsilon \tag{4.18}$$

From Eq. (4.17) and Eq. (4.18), one can write;

$$\sigma_1 = 3.82 \times 10^{-21}\frac{1-T}{c\,z} \tag{4.19}$$

And the 1PA cross section in units of cm^{-1} can be calculated using;

$$\propto = \sigma_1 N_A c \tag{4.20}$$

For single photon polymerization, the intensity change of an excitation beam along the optical propagation path z is given by [144];

$$\frac{dI(z)}{dz} = -\propto I(z) \tag{4.21}$$

The resin that we used contained 0.64 wt.% of Irgacure 369 photoinitiator molecules (molar mass of 366.5 g/mol). Knowing that the path length is 22 μm (thickness of the resin), the molar absorptivity and the single photon absorption cross section of ORMOCER (1300 g/L density) can be calculated using Eq. (4.17) and (4.19) they were found to be 1.7×10^4 L mol^{-1} cm^{-1} and 6.5×10^{-17} cm^2 respectively. The probability of a molecule absorbing one photon is proportional to the intensity of the excitation beam;

$$n^{(1)} = \sigma_1 N_g \frac{I}{h\omega} \tag{4.22}$$

where $n^{(1)}$ is the number of molecules excited by 1PA per unit time and unit volume in the material, Ng is the density of molecules in the ground state g, I is the intensity of the excitation source (in energy per unit time and area), and where h ω is the energy of an incident photon, h is Planck's constant (J.s) and ω is the laser repletion rate (s[-1]).

4.3.2   TWO PHOTON ABSORPTION

Two-photon absorption (2PA) is the simultaneous absorption of two photons of identical or different frequencies in order to excite a molecule from one state to a higher energy electronic state. The energy difference between the involved lower and upper states of the molecule is equal to the sum of the energies of the two photons. Two-photon absorption (2PA) is a second-order process, several orders of magnitude weaker than linear absorption. It differs from linear absorption in that the strength of absorption depends on the square of the light intensity, thus it is a nonlinear optical process. The intensity change of an excitation beam along the optical propagation path z is given by [144];

$$\frac{dI(z)}{dz} = -\beta I^2(z) \tag{4.23}$$

Where β is the TPA coefficient of the solution. By integrating Eq. (4.23) we get;

$$\frac{I(z)}{I_o} = \frac{1}{1 + I_o z \beta} \tag{4.24}$$

Where I_o is the incident intensity and can be calculated using [145];

$$I_o = E_o \frac{2.44}{\pi d_o^2 t_p} \tag{4.25}$$

Where E_o is pulse energy, d_o is the laser beam diameter and t_p is the pulse duration. Furthermore, the 2PA coefficient β (in units of cm/GW) of a given solution sample is determined by;

$$\beta = \sigma' N_A c \tag{4.26}$$

Where σ' is the molecular TPA coefficient (or cross section) of the same compound (in units of cm^4/GW) and N_A is the Avogadro constant. For a known β and c, the value of σ' can be easily calculated from Eq. (4.26). The value of TPA coefficient cross section can be expressed in units of cm^4/s using;

$$\sigma_2 = h\omega\sigma' \tag{4.27}$$

The probability of a molecule absorbing two photons simultaneously is proportional to the square of the intensity of the excitation beam;

$$n^{(2)} = \frac{1}{2}\sigma_2 N_g (\frac{I}{h\omega})^2 \tag{4.28}$$

Where $n^{(2)}$ is now the number of molecules excited by 2PA in the unit volume per unit time. The prefactor of 1/2 reflects the fact that two photons are needed to excite one molecule.

4.3.3 THREE PHOTON ABSORPTION

Three-photon absorption (3PA) works when three photons are simultaneously absorbed in one event and its most commonly occurs in longer wavelengths. The intensity change of an excitation beam along the optical propagation path z is given by [144];

$$\frac{dI(z)}{dz} = -\gamma I^3(z) \tag{4.29}$$

Where γ is the three-photon-absorption coefficient, the given sample medium in units of cm^3/GW^2. The solution of Eq. (4.29) can be obtained as;

$$\frac{I(z)}{I_o} = 1/\sqrt{(1 + 2\gamma z I_o^2)} \tag{4.30}$$

The value of γ can be found from the theoretical fitted curve representing the relationship between the transmitted intensity and the incident intensity. The three-photo-absorption cross section for a given solution in units of cm^6/s^2 can be obtained as;

$$\sigma_3 = \frac{\gamma(h\omega)^2}{N_A c} \tag{4.31}$$

Similar to 1PA and 2PA, the probability of a molecule absorbing three photons simultaneously is proportional to the cubic of the intensity of the excitation beam;

$$n^{(3)} = \frac{1}{3}\sigma_3 N_g \left(\frac{I}{h\omega}\right)^3 \tag{4.32}$$

Where $n^{(3)}$ is now the number of molecules excited by 3PA in the unit volume per unit time. The prefactor of 1/3 reflects the fact that three photons are needed to excite one molecule.

4.3.4 DUAL PHOTON ABSORPTION

In this section, we report a new phenomenon of dual wavelength multiphoton absorption (DWA). This phenomenon induces two temporally separated femtosecond laser pulses of different wavelengths (515 and 1030 nm), to generate microstructures via multiphoton polymerization. The phenomenon is explained from the response of photoresist for the laser pulses of dual wavelengths. To the best of our knowledge, this is the first demonstration of dual wavelength polymerization phenomenon, a process that may allow the fabrications of 2D and 3D components of very high resolution. In case of dual wavelength multiphoton absorption, the mechanism is based on two-photon absorption followed by one-photon absorption from the excited level which leads to the same cubic relationship of 3PA between the fluorescence intensity and the excitation intensity. However, in the DWA one can guarantee absorption of the third photon by controlling the separation time of the successive dual wavelength pulses. Under the excitation of high-power ultrafast-pulsed laser, the system simultaneously absorbs n identical photons, promoting an electron from S0 to S1 by virtual states. Subsequently, the electron is excited to higher-lying state Sh by absorbing another single photon, resulting in multiphoton absorption (MPA)-induced excited-state absorption (ESA). We name this process as dual

wavelength three-photon absorption (DWA) and Figure 4.17 illustrates an effective 3PA process of 2PA-induced ESA. In this case, the propagation equation of the pulse intensity is given by [146];

$$\frac{dI(z)}{dz} = -\beta I^2(z) - \propto I(z) \tag{4.33}$$

The solution of Eq. (4.33) can be obtained as;

$$\frac{I(z)}{I_o} = \frac{\propto e^{-\propto z}}{\propto + \beta I_o (1 - e^{-\propto z})} \tag{4.34}$$
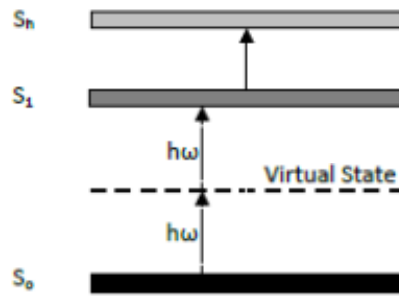
Figure 4.17 Schematic diagram of dual wavelength absorption process.

Figure 4.18 (a and b) shows the measured transmitted laser beam intensity versus the incident intensity in both 2PA and 3PA of ORMOCER. The transmitted intensity dependence on the incident intensity clearly shows an optical power limiting behavior. The solid curve in Figure 4.18 (a and b) is the theoretically fitted curve which should represent Eq. (4.23) and Eq. (4.29). From the best-fit the values of β and γ were found to be 0.038 cm/GW and 6.14 × 10-18 cm^3/GW^2 respectively. The 2PA cross section and 3PA cross section can be calculated using Eq. (4.26) and Eq. (4.30) and they were found to be 4.79 × 10-54 cm^4/s and 1.33 × 10-83 cm^6/s^2 respectively.

Generally, photons might ionize an atom only if they had energy greater than a particular threshold energy corresponding to the ionization energy of the atom. An atom might absorb two
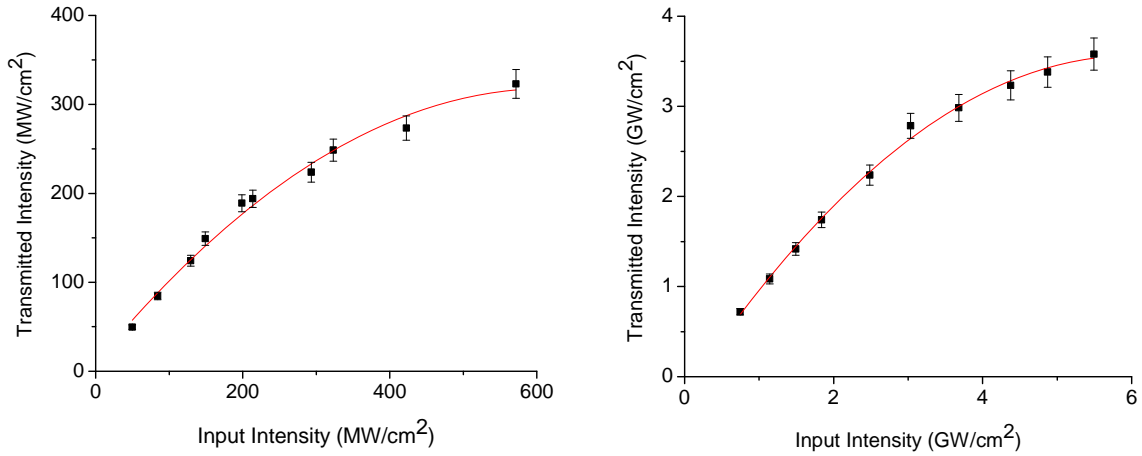
Figure 4.18 Transmitted intensity as a function of the incident intensity for (a) 2PA with femtosecond laser at 515 nm wavelength (left), (b) 3PA with femtosecond laser at 1030 nm wavelength (right).

or more photons simultaneously, thus allowing an electron to transition to states unreachable by single photon absorption. If a third photon interacts with the atom soon after the two-photon process, the third photon may ionize the atom. When absorbing multiple photons simultaneously, an atom will proceed to an intermediate state corresponding to a characteristic eigenstate or to a "virtual state." These virtual states are not eigenstates; they correspond to no specific n or l state. Instead, they are merely superpositions of waves. No population of electrons transitions to the virtual state.

The lifetime of a virtual state is short, relative to eigenstates. Actually, the closer the virtual state is to an actual eigenstate, the longer the lifetime of the virtual state as a result of the Heisenburg's Uncertainty Principle, with a virtual state lifetime approximated as $h/(4\pi\Delta E)$ where ΔE is the energy difference between the virtual and actual states. An allowed two-photon transition can be viewed as a sequence of two one-photon allowed transitions [147], hence, the DWA mechanism can be viewed as a sequence of three one-photon allowed transitions. The

73

lifetime of the virtual state was estimated ~30ps which is longer than the duration between successive pulses of the laser beam (~1 ps in our experiment) [147]. Thus the third photon will be absorbed before the end of the lifetime of the virtual state.

As a result of the intensity dependence of 2PA and 3PA provide a mechanism by which chemical or physical processes can be activated with high spatial resolution [148]. The ability of 2PA to excite molecules with this 3D spatial resolution, results from the fact that the intensity of a focused laser beam decreases approximately as the square of the distance, z, from the focus. Thus, since 2PA scales quadratically with light intensity (Eq. 4.23), the number of excited states formed by 2PA is proportional to z^{-4}, whereas the number of excited states formed by one-photon absorption is proportional to z^{-2}. In the mean time, a higher spatial resolution is expected for 3PA than both 1PA and 2PA because the laser intensity decreases approximately as the cubic of the distance z and the number of excited states formed by 3PA is proportional to z^{-6}. This is illustrated in Figure 4.9, where the theoretical dependence of the intensity ratio (or transmittance) for a laser beam with a Gaussian profile for 1PA, 2PA, 3PA and DWA is simulated as a function of z/z_r where z_r is Rayleigh length. The 2PA and 3PA transition requires photons with approximately half the energy (twice the wavelength), and $1/3^{ed}$ (triple the wavelength), respectively of that of the photons needed for 1PA into the lowest excited state of a molecule. If the beams at wavelengths λ and 2λ have the same waist at the focus, the excitation rate follows the trend of the solid lines in Figure 4.19 for the 1PA, 2PA, 3PA and DWA cases. It can be seen that the width of the peak is narrower in the latter situation which means better resolution for the much stronger distance dependence of polymerization process. In other words, 3PA should provide the best spatial resolution among the other suggested processes. However, 3PA is very weak relative to 2PA and 1PA in the sense that the ratio $n^{(3)}/n^{(2)}$ and $n^{(3)}/n^{(1)}$ is typically small for
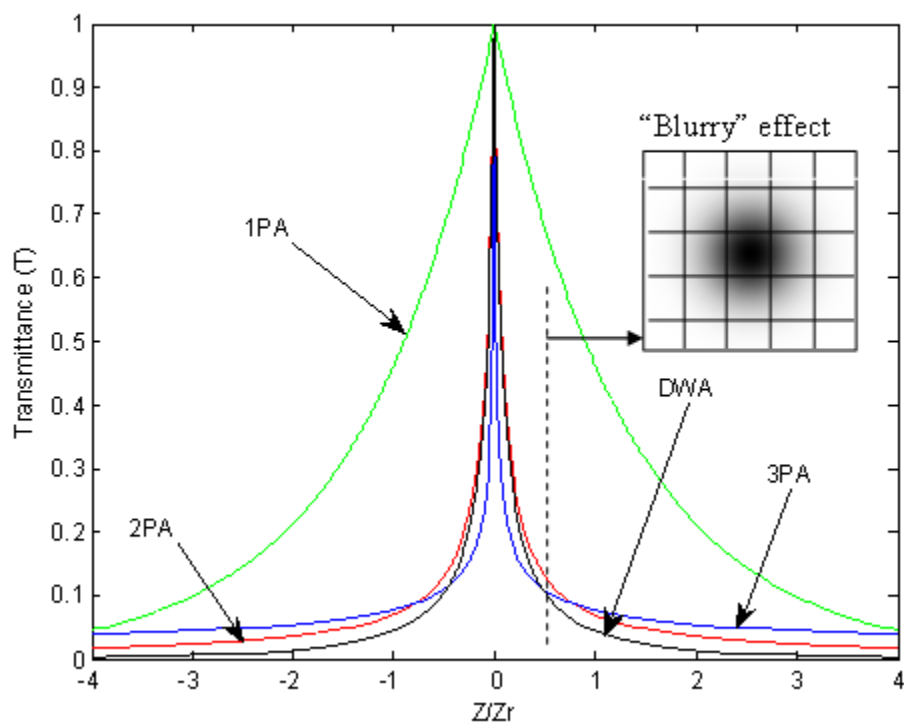
Figure 4.19 Transmittance for the 1PA, 2PA, 3PA and DWA processes along the laser beam propagation direction and the "Blurry" effect using Eq. (4.15), Eq. (4.17), Eq. (4.23) and Eq. (4.27) respectively..

intensities below about 10 GW/cm^2, and for the absorption cross sections seen in typical organic molecules. Usually, pulsed lasers with high peak power are needed to study 2PA and 3PA in materials and for applications based on this processes. Practically, the spatial resolution could be improved by utilizing either shorter wavelengths, but the diffraction limit cannot be circumvented. This means that using 2PA is more appropriate to achieve better spatial resolution and eliminate the "Blurry" effect (which happens as a result of continuous photochemical reaction beyond the targeted area) that occurs more effectively with 3PA process as shown in Figure 4.19. On the other hand, the suggested mechanism (DWA) combines the good spatial

resolution of 3PA and fact the 2PA overcomes the "Blurry" effect and the results can be seen in the figure.

Performing photopolymerzation in air, which would simplify commercial practice, has major complication due to two effects of oxygen. Oxygen acts as a quencher of photoexcited states of molecules and also inhibits polymerization by reaction with radicals. This problem can be avoided by performing the photopolymerization under an inert atmosphere (nitrogen or argon). Using a protective coating of paraffin oil or some other compound has also been reported [149]. These methods are usually avoided because of cost and other practical considerations. The use of dual wavelength system overcomes the oxygen problem by having a higher intensity energy absorption in the surface layer.

To realize real 2D microstructuring with femtosecond lasers we scanned the laser beam with an x-y galvo scanner with a translation stage. Figure 4.20 shows SEM images for a microrode using 1.02 μm laser beam diameter through 3PA, 2PA and DWA processes. The average microrode diameters were found to be about 1.9 μm, 1.6 μm and 1.2 μm for the three mechanisms respectively. It can be seen from the images that although the laser spot size diameter was 1.02 μm, the fabricated microrodes in all the cases were bigger. It is the "blurry" effect that causes the size to be bigger and it's clearly that this effect is less effective in case of DWA. Finally, Figure 4.21 shows an example of microfeatures generated by DWA method after laser irradiation of nanofiber dispersed Ormocer at a repetition rate of 13 MHz, a power of 250 mW. The image clearly shows that the "blury" effect is less effective when the microfeatures are fabricated using DWA method compared with the microfeatures created by 2PP shown I n Figure 2.15.
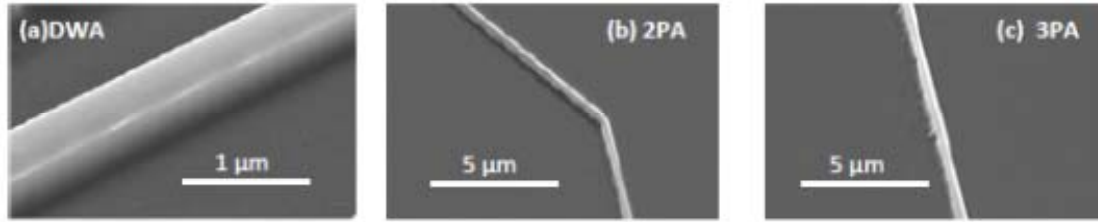
Figure 4.20 SEM images of fabricated microfeatures using 2PA, 3PA and DWA processes.
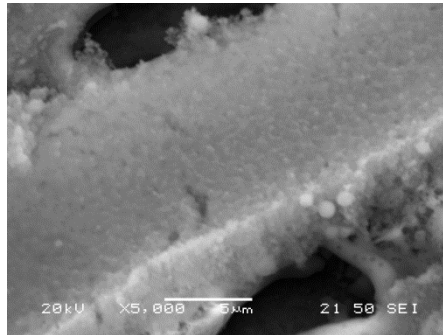
Figure 4.20 SEM images of fabricated nanofibers reinforced microfeature using DWA processes.

4.4   SUMMARY

A new microfabrication technique for the formation of microfeatures with nanofibers-reinforced polymer was presented in this chapter. Femtosecond laser has been utilized for both nanofibers generation and struture formation through MPP. Nanofibers-reinforced polymer microstructure was created with a single-step irradiation of nanofibers dispersed Omorcer. A new method combining finite difference, and Runge–Kutta 4 transient thermal model has been developed to calculate the temperature distribution on the top surface of the substrate during laser ablation for nanostructuring. Increasing power of the femtosecond laser results in the

increase of energy/pulse which increases the surface temperature. The high temperatures (above boiling) results in the formation of nanofibers while low temperatures (below boiling) would result in the formation of nanospheres. The final shape of the microstructure is highly dependent on the energy of the femtosecond laser. The feature size increases with the increase of laser power till it reaches the polymer ablation threshold. The scattering effect caused by the nanofibers significantly enlarged the size of the produced voxel volume, hence the resolution. This technique will open the door for the development of new applications previously not possible, particularly in rapid prototyping of biomedical imprinted micro devices, which requires unique mechanical and electrical properties. More investigations will be done to characterize the properties of the reinforced polymer structures in the next chapters. Since MPP has been demonstrated for three dimensional microfabrications, this new method should have the potential for the direct fabrication of reinforced three dimensional structures.

Finally, we have demonstrated a new phenomenon of three photon absorption with dual wavelength femtosecond laser and its ability to significantly reduce the "blurry" effect. We have derived an analytical expression for the transmittance that depends on the 1PA and 2PA cross-sections. We have also presented the analytical theory of the z-dependent nonlinear transmission for straightforwardly yet unambiguously characterizing DWA. Experimental results showed that microfeatures obtained by DWA method have better resolution than other 2PA and 3PA microfeatures because of the significant elimination of the "blurry" effect.

CHAPTER 5

NANOCOMPOSITES MICROFEATURES WITH

ENHANCED PROPERTIES

The previous chapter shows that femtosecond laser irradiation is a useful tool for the fabrication of nanocompsite microstructures. This chapter focuses on examining mechanical, electrical, and magnetic properties of nanocomposites microfeatures fabricated through this method.

5.1 MECHANICAL PROPERTIES ENHANCEMENT

The NanoIndentation Tester uses an already established method where an indenter tip with a known geometry is driven into a specific site of the material to be tested, by applying an increasing normal load. When reaching a pre-set maximum value, the normal load is reduced until partial or complete relaxation occurs. At each stage of the experiment, the position of the indenter relative to the sample surface is precisely monitored with a differential capacitive sensor. For each loading/unloading cycle, the applied load value is plotted with respect to the corresponding position of the indenter. The resulting load/displacement curves provide data specific to the mechanical nature of the material under examination. Established models are used to calculate quantitative hardness and elastic modulus values for such data [150-157].

The mechanical properties of the fabricated microstructure were determined by using NanoIndentation Test System. The sample was mounted horizontally on motorized X

translational table. The tests were carried out on the fabricated microfeature (60 μm length by 10 μm width by 10 μm width by 8 μm thick) at initial load of 0 μN and increased linearly to maximum load of 20000 μN. A loading rate of 40000 μN/min was maintained during the incremental increase of the load, until the indenter reached the maximum depth into the surface. The load was then held for 30 s before the indenter was unloaded. Two indentations were measured to obtain average value.

Indentation of the surface of a material with an indenter loaded with force, results in a penetration depth of the indenter into material. The data is recorded as a function of time, consisting of a single loading and unloading cycle curve and indentation depths as shown in figure 5.1. The incorporation of silicon nanofibers into the Ormocer matrix, resulted in its film surface being more resistant to penetration by an indenter compared to that of the pure Ormocer obtained by Doraiswamy et al [157]. The maximum indentation depth at the maximum load of 20000 μN was about 1900 nm.

Hardness and elastic modulus can be determined using the method developed by Oliver and Pharr [154]. The hardness represents the resistance of a material to local surface deformation. The Indentation Testing Hardness, H, is determined from the maximum load, F_{max}, divided by the projected contact area A_p at the contact depth h_c [158];

$$H = \frac{F_{max}}{A_p(h_c)}$$
(5.1)

Where A_p (h_c) is the projected area of contact of the indenter at distance, h_c from the tip and h_c is the depth of the contact of the indenter with the test piece at F_{max} .Which can be expressed by $h_c = h_{max} - \varepsilon(h_{max} - h_r)$, where h_{max} is the maximum indentation depth at F_{max}, h_r is the point of intersection of the tangent to the unloading curve with the depth axis, and ε is a constant depending on the nonlinearity of the unloading curve [151]. For modified Berkovich indenter,

$A_p(h_c) = 24.5\ h_c^2$ [152]. The elastic modulus represents the overall stiffness of the reinforced

polymer network. The reduced modulus of the indentation contact, E_r, is given by [158];

$$E_r = \frac{\sqrt{\pi}.S}{2\sqrt{A_p(h_c)}} \qquad (5.2)$$
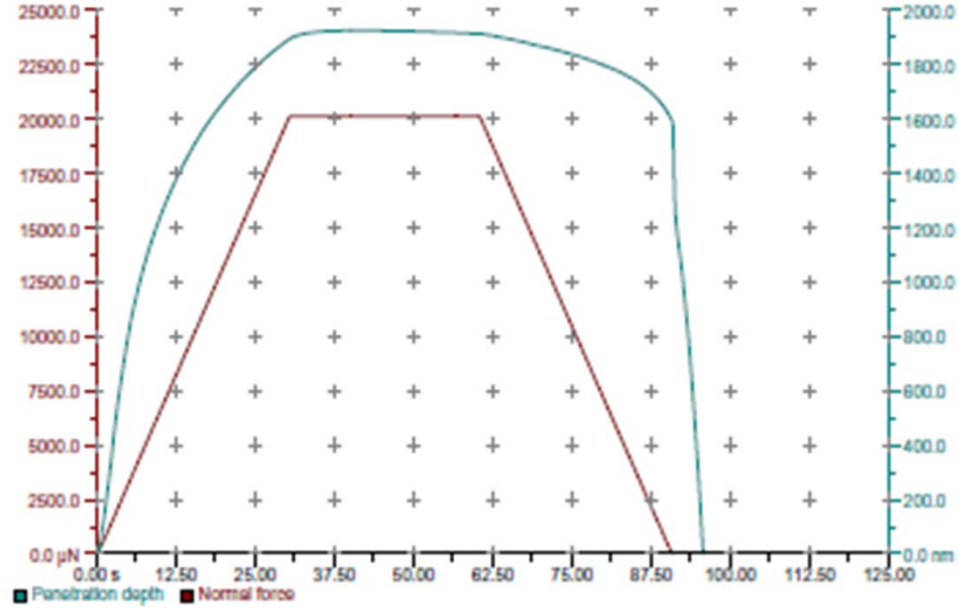
Figure 5.1 Indentation normal force and penetration depth with time for the reinforced polymer.

where S is the contact stiffness or the slope of the unloading curve at the point of maximum load

which can be found by;

$$S = \frac{F_{max}}{h_{max} - h_r} \qquad (5.3)$$

The relationship between Indentation Modulus, E, and the reduced modulus, E_r, of the

sample is given by [158];

$$\frac{1}{E_r} = \frac{1 - v_s^2}{E} + \frac{1 - v_i^2}{E_i} \qquad (5.4)$$

Where v_i is the Poisson's ratio of the indenter, v_s is the Poisson's ratio of the sample and E_i is the

modulus of the indenter. Figure 5.2 shows the typical indentation loading–unloading curves for

81

the fabricated reinforced polymer microstructure. The hardness and Young's modulus values for a polymerized Ormocer surface, were determined in a previous work using nanoindentation and were found to be 0.185 GPa and 7.011 GPa, respectively while Poisson's ratio is 0.45 [153]. The hardness and Young's modulus of Silicon using nanoindentation were found to be 13 GPa and 202GPa, respectively while Poisson's ratio is 0.22 [154]. The average nanoindentation hardness and reduced Young's modulus of the reinforced polymer microstructure were found to be 10.332 Pa and 14.793 GPa respectively. Using the information in Figures 5.1 and 5.2 and utilizing Equations 5.1 to 5.3, the hardness and elastic modulus of the reinforced polymer microstructure were found to be 0.226 GPa and 11.936 GPa respectively. Clearly, the incorporation of Silicon nanofibers into the Ormocer has a significant effect on mechanical properties enhancement. Hardness and elastic modulus of the polymer were increased by about 25% and 75% respectively.
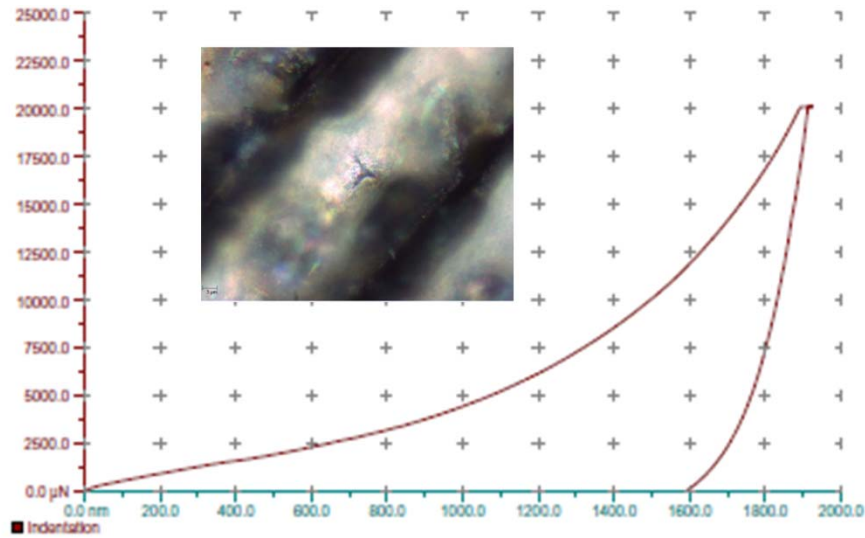
Figure 5.2 Typical indentation load–displacement curves for the reinforced polymer.

The elastic stress–strain characteristics of a randomly nanofibers dispersed polymer are described by three elastic constants, namely, Young's modulus E, Poisson's ratio n vs , and shear

modulus G. Only two of these three elastic constants are independent since they can be related by the following equation [159];

$$G = \frac{E}{2(1+v_s)} \tag{5.5}$$

By substituting the values of E, and v_s, the shear modulus can be calculated and it was found to be G=4.116 GPa for the reinforced polymer microstructure. This is an increase from 2.417 GPa for pure polymerized Ormocer [153].

A thin layer containing randomly oriented discontinuous nanofibers exhibits planar isotropic behavior. The properties are ideally the same in all directions in the plane of the layer. For such a layer, the tensile modulus and shear modulus are calculated from [159];

$$E = \frac{3}{8}E_{11} + \frac{5}{8}E_{22} \tag{5.6}$$

$$G = \frac{1}{8}E_{11} + \frac{1}{4}E_{22} \tag{5.7}$$

where E_{11} and E_{22} are the longitudinal and transverse tensile moduli for a unidirectional discontinuous nanofiber lamina of the same nanofiber aspect ratio, and same nanofiber volume fraction as the randomly oriented discontinuous nanofiber composite. Rearrange Eqn 5.7 and subtract Eqn 5.6 from Eqn 5.7, then using transverse modulus $E_{22} = \frac{1+2\eta_t v_f}{1-\eta_t v_f}E_m$, $\eta_t = \frac{(E_f/E_m)-1}{(E_f/E_m)+2}$, Poisson's ration $v_s = v_f v_f + v_m v_m$ and $v_f + v_m = 1$ [155], the volume fraction ratio of the nanofibers in the polymer matrix can be written as;

$$v_f = \frac{\frac{8(3G-E)}{E_m}-1}{\left(\frac{(E_f/E_m)-1}{(E_f/E_m)+2}\right)\left(2+\frac{8(3G-E)}{E_m}\right)} \tag{5.8}$$

wherev_m is the volume fraction of the polymer matrix, v_f and v_m are Poisson's rations of nanofibers and polymer matrix respectively, E_f and E_m are Young's moduli for nanofibers and polymer matrix respectively. By substitutin the appropriate values in Eqn 8, the volume fraction

of the nanofibers, generated with femtosecond laser at 13 MHz and 15W, in the polymer matrix can be calculated and it was found to be 24%. An important function of the matrix in a nanofiber-reinforced composite material is to provide lateral support and stability for nanofibers under longitudinal compressive loading like the one applied by the indenter head. In polymer matrix composites in which the matrix modulus is relatively low compared with the nanofiber modulus, failure in longitudinal compression is often initiated by localized buckling of nanofibers. Usually, the shear mode of failure is more important than the extensional mode of failure and the shear mode is controlled by the matrix shear modulus as well as nanofiber volume fraction [159].

A viscoelastic polymer has an elastic component and a viscous component. Applying stress to a polymer causes molecular rearrangement as a result of changing positions by parts of the long polymer chain (creep). Polymers remain solid even when these parts of their chains are rearranging in order to accompany the stress which creates a back stress in the material. When the back stress is of the same magnitude as the applied stress, the material no longer creeps. If the original stress is taken away, the accumulated back stresses will cause the polymer to try to return to its original form with the help of its elastic component. The polymer loses energy when a load is applied then removed with the area between loading and unloading curves (figure 5.2) being equal to the energy lost during the loading cycle. Thus permanent plastic deformation of the polymer occurs even when the applied load is removed.

The high surface area of nanofibers provides better interaction between the polymer chains and nanofibers [160]. The silicon nanofibrous structures act as a preferential nucleation site for crystalline phases which results in an increase in the modulus and hardness [161]. Hardness, which is directly related to the flow strength of a material, depends on the effective

load transfer between the matrix and the reinforcement phase in the composite. Strong interfacial bonding between the matrix and the nanofibers is essential for efficient load transfer to obtain high strength. Plastic deformation in polymers occurs by nucleation and propagation of shear bands [162]. Shear bands in the unreinforced polymer matrix propagate unhindered as there are no barriers for their movement. However, the presence of nanofibers in the composites could offer resistance for the propagation of shear bands. A good mechanical interlocking and the presence of obstacles to the motion of shear bands are the reasons for the enhancement of hardness and elastic modulus in polymer dispersed nanofibers.

5.2   CONDUCTIVE POLYMERS MICROFABRICATION

Many methods for the synthesis of conductive polymers have been developed. Most conductive polymers are prepared by oxidative coupling of monocyclic precursors. Such reactions entail dehydrogenation [163]. One challenge is usually the low solubility of the polymer [163]. An important property of the electrically conductive reinforced polymer is the positive temperature coefficient (PTC) effect, which means that the electrical resistivity of the composites increases during the heating process, and hence decreasing the electrical conductivity of the reinforced polymer [164]. PTC materials have widespread applications, including sensors, self-regulating heaters, and switching materials. The PTC mechanism was due to the difference in the coefficients of thermal expansion between the fillers and the matrix [165, 166].

A conductive polymer microstructure was fabricated with the method described in chapter 4. The conductive nanostructure was formed from graphite sheet. The conductivity of the nanocomposite was measured using two probe system.

The first step in this technique is the generation of Carbon fibrous nanostrcutures (CFN) using the femtosecond laser. Figure 5.3 shows the SEM images of areas in the specimens processed with frequencies 2, 4, 8 and 13 MHz and a pulse width of 428 fs. This frequency range is well above the threshold frequency for nanoparticle formation [167]. The nanofibers were formed by agglomeration of nanoparticles and the 3-D web-like nanofibers have average diameters of 90, 70, 55 and 40 nm for repetition rates of 2, 4, 8 and 13 MHz respectively. Figure 5.4 shows the Raman spectra of the bulk nontreated carbon substrate and the laser irradiated areas at various repletion rates of 2, 4, 8 and 13 MHz. All samples exhibit mainly two Raman bands at about 1580 and 1335 cm^{-1}, respectively, the former corresponding to the Raman-allowed E_{2g2} mode called the graphite mode (G-band) and the latter to the defect-induced Raman band called the defect mode (D-band) [168]. Also, a D-band at approximately 1620 cm^{-1} due to the maximum in the phonon density of states is clearly observed at all repetition rates. The shapes of the D and G peaks become broader, and the bandwidth of the D peak increases with increasing repetition rate. These features of the Raman spectra are similar to those published in literatures for carbon nanofibers [169].

Femtosecond laser TPP technique can be used to fabricate arbitrary 2D and 3D microstructures. The SEM image in Figure 5.5 shows a reinforced channel produced at a repetition rate of 13 MHz, a laser power of 140 mW and a continuous scan at a speed of 5 μm/sec. These microstructures are built from the lines of solidified liquid resin. Thus, it is very important to investigate spatial resolution of the solidified resin and to optimize fabrication parameters in order to obtain better quality of microstructures. The lateral dimension of solidified lines can be written as [170];

$$d = \frac{I_o}{NA} \sqrt{\ln \left(E_o \frac{NA^3 P^2}{V} \right)} \tag{5.9}$$
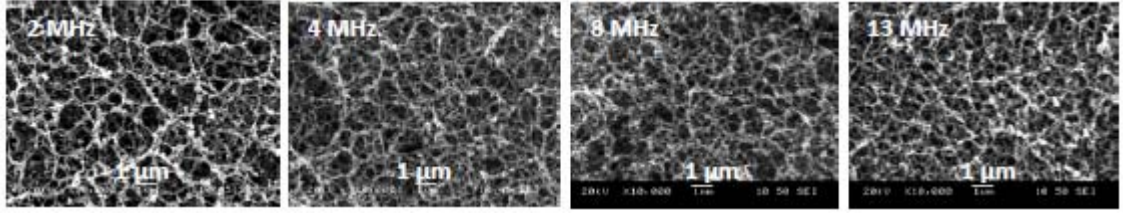
Figure 5.3 SEM Images of the generated CFN's using femtosecond laser of 2, 4, 8 and 13 MHz.
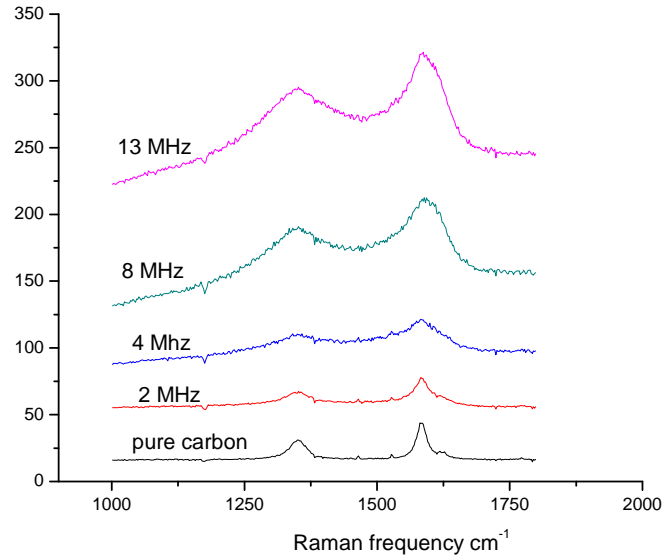
Figure 5.4 Raman spectroscopy of untreated and laser irradiated carbon substrates.

where $I_o = \frac{2\lambda}{\pi n}$ and $E_o = \frac{2.78 \frac{\sigma_2}{A} n^3}{(hc)^2 \tau f_q \lambda}$, f_q, τ, and λ refer to the repetition rate, pulse width and wavelength of femtoscend laser, respectively, c denotes the velocity of femtosecond laser in vacuum, n and σ_2/A are the refractive index and the characterization of the TPA material, respectively. From the above expressions, it can be found that the laser power (P), scanning speed (V), and numerical aperture (NA) make a difference on the dimensions of solidified lines when other parameters are constant for a given experimental system and photosensitive resin (E_0

and I_0) are nonadjustable. It is seen that with increasing laser power and decreasing scanning speed, the line width increases correspondingly. A focusing objective lens with focal length of 12.48 mm is selected. The influence of scanning speeds and laser power on line width as well as the experimental results obtained is shown in Figure 5.6. From the experimental results, we observed that the scanning speed of 5 and 10 µm/s the resin can be solidified completely via TPP when the power ranges from 80 to 140 mW. Also, we can see the phenomenon clearly that as the scanning speed increases, the line width tends to become smaller. These results are in agreement with the theoretical results. The larger values of the line width in the experimental results are mainly due to the existence of carbon nanofibers in the polymer resin [170].

Electrical properties of compositions made of nanofibers, dispersed in polymer, are mainly characterized by the formation of a conduction network by contact conditions between neighboring nanofibers in the network. In this work, CFN's dispersed in the developed resin was used as a conductive composition material. The conductivity of the nanocomposite films was measured using two points probe testing device from SVSLabs Inc. The voltage passing through the nanocomposite film was recorded, as well as the current and the value of the resistance (and hence the conductivity) was obtained using Ohm's law.

Figure 5.7 shows the relationship between the laser repetition rate, electrical conductivity and mean particle size. It is clearly indicates that as the repetition rate of the femtosecond laser increases, the electrical conductivity of the microstructure increases. A significant increase in CNF's density is observed as the repetition rate increases (Figure 5.3). Since laser power and spot size were kept constant in our experiments, pulse energy reduces with the increase of pulse repetition rate and results a reduction in nanofiber size and hence increase CNF's density [19].

Consequently nanoparticles ejected by successive laser pulses prefer to agglomerate with particles ablated from the previous laser pulse, which are still at very high temperature and results an increase of nanofibrous structure density [170, 171]. Further increase in frequency can increase the number of nanoparticles which are agglomerating to the nanofibrous structure [170, 171]. This increase in CFN's density results in higher CFN's content in the polymer and such alarger conductive network inside the polymer. This means higher electrical conductivity provided that the CNF's content is higher than the percolation threshold.
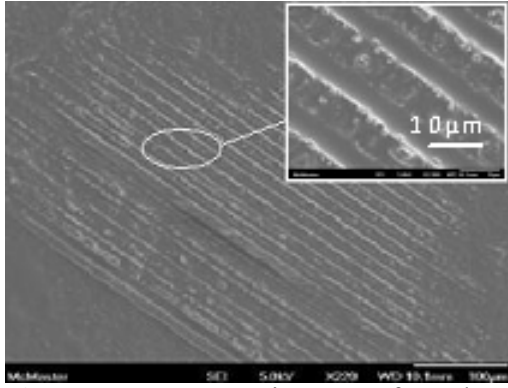
Figure 5.5 SEM image of carbon nanofibers reinforced polymer microfeatures
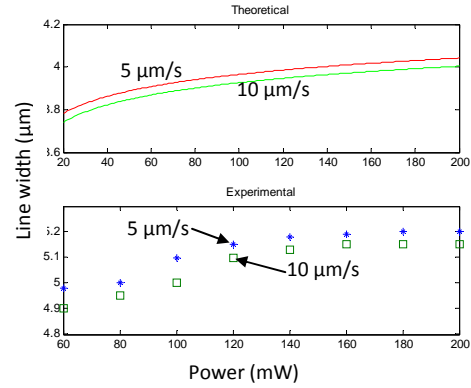
Figure 5.6 Relationship between line width and laser power (theoretical and Experimental)
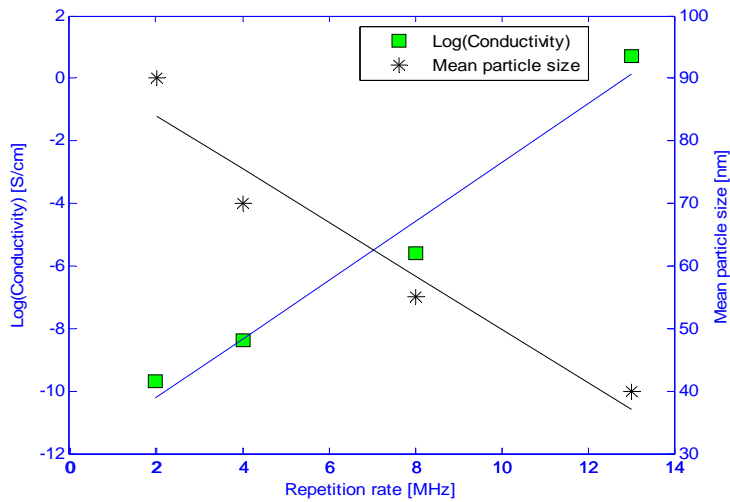
Figure 5.7 Relationship between electrical conductivity and laser repetition rates.

Figure 5.8 shows the temperature dependence of the reinforced polymer on the electrical conductivity for laser repetition rate of 13 MHz. It can be seen that the electrical conductivity of the reinforced polymer decreases as temperature increases, mainly due to PTC effect. Electrical conductivity in CNF's reinforced polymer exist because of the direct contact between CNF's and tunneling resistance determined by the width of the insulating resin around the CNF's. Thermal expansion caused by heat gradient increases gap width between contiguous CNF's and reduces the number of conductive pathways which results in a decrease in electrical conductivity.
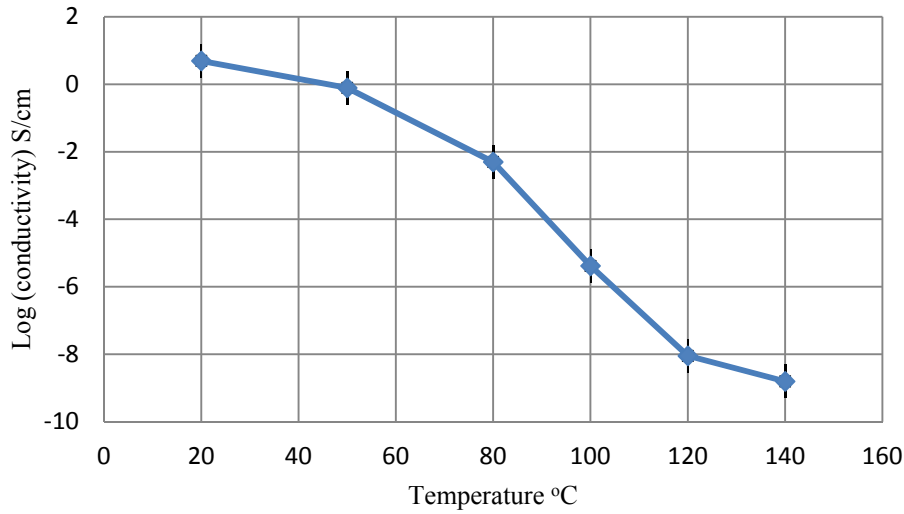
Figure 5.8 Effect of temperature on the electrical conductivity of the CNF's nanocomposit.

The temperature dependence of the electrical conductivity maybe explained by the general theory of the thermal fluctuations. The resistivity of the junction is given by [172]

$$\rho = \rho_o e^{-T_1/(T+T_o)} \qquad (5.10)$$

Where the constants ρ_0, T_1, and T_0 depend essentially on the characteristics of the tunnel junctions, which are supposed to be functions of various parameters such as filling factor, filler

size and shape, sample processing. The relative resistivity (ρ_r) can be used to characterize the intensity of the PTC effect:

$$\rho_r = \log\left(\frac{\rho_{140}}{\rho_{20}}\right) \qquad (5.11)$$

Where ρ_{140} and ρ_{20} are the resistances of the composites at 140 and 20°C, respectively. Thus the relative conductivity can be expressed as;

$$S_r = \log\left(\frac{\rho_{20}}{\rho_{140}}\right) \qquad (5.12)$$

The influence of repetition rate on the relative conductivity and mean particle size is shown in Figure 5.9. This indicates how sensitive and to what extent the reinforced polymer resistance responds after being stimulated by the temperature change. The electrical sensitivity of the reinforced polymer can be expressed by;

$$K_s = \frac{\Delta S_r}{\Delta \omega_r} \qquad (5.13)$$

Where K_s is the electrical sensitivity, ΔS_r is the change in relative conductivity and $\Delta \omega_r$ is the change in relative repetition rate which can be expressed by;

$$\omega_r = \frac{\omega}{\omega_{min}} \qquad (5.14)$$

where ω_{min} is the minimum repetition rate used to generate nanofibers, in this case it is 2 MHz. The equation of the straight line obtained from Figure 5.9 is $S_r = 0.1743\,\omega_r - 10.6117\ 17$ which indicates that the electrical sensitivity K_s is about 0.1743. The higher the value of the electrical sensitivity, the more sensitive is the reinforced polymer to change in temperature and thus less conductivity at higher temperatures. Also, the PTC effect of nanocomposites fabricated with high laser repetition rate is weaker, than that of nanocomposites fabricated with low repetition rate. This is a direct result of the volumetric expansion of the matrix which cause more contiguous CFN's to get disconnected and reduce number of electrical pathways.
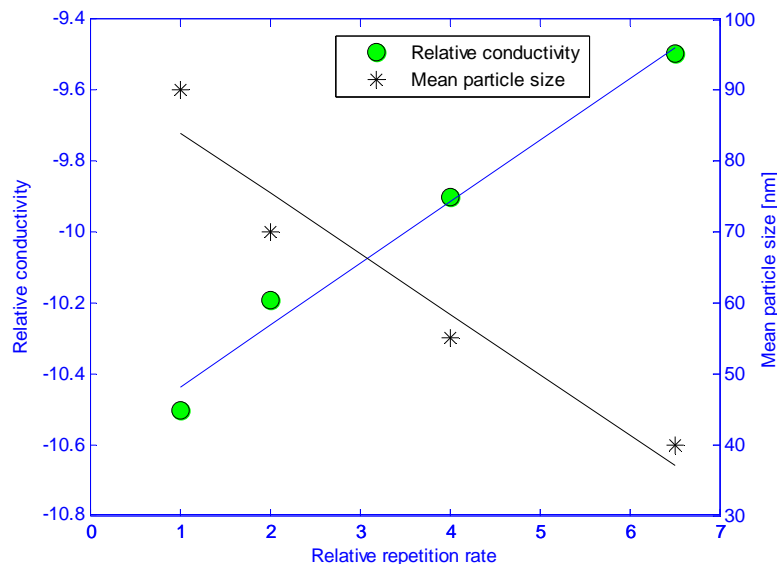
Figure 5.9 Influence of repetition rate on relative conductivity of the nanocomposite.

5.3   MAGNETIC POLYMER NANOCOMPOSITES

Magnetic polymer nanocomposites can be defined as materials composed of an inorganic magnetic component in the form of particles, fibers or lamellae, with at least one dimension in the nanometer range (1±100 nm) embedded in an organic polymer or vice versa. The basic idea in a composite is to integrate several component materials and their properties in a single material. In magnetic polymer nanocomposites, organic-inorganic synergies add new properties that cannot be achieved in just organic or inorganic materials.

Magnetic neodymium-iron-boron (NdFeB)nanofibers and nanoparticles, have become one of the hotspots in the research field of magnetic materials to meet the demand for miniaturization of electronic components in recent years, and have been successfully prepared by various routes like the sol-gel auto-combustion method [173], co-precipitation [174], hy-

drothermal method [175], reverse micelles [176], microemulsion method [177], alternate sputtering [178], pulsed laser deposition [179], and so on. However, until now there have been no reports on the synthesis and magnetic properties of NdFeB ferrite nanofibers in literatures.

In this section, a magnetic weblike fibrous nanostructure is formed due to the agglomeration of the bulk quantity of nanoparticles created during laser ablation at mega hertz pulse frequency. A distinct characteristic of the fibrous nanostructures is that particles are fused and the agglomeration shows certain degree of organization, unlike the random stacking of particles observed at femtosecond laser ablation at pulse frequency in kilohertz and hertz regime. The effect of pulse repetition rate on the nanofibers size and hence the magnetization was also investigated. The nanostructureswere characterized by scanning electron microscopy (SEM), transmission electron microscopy (TEM), energy-dispersive x-ray (EDX), x-ray diffraction (XRD) and magnetic force microscopy (MFM).Also, the fibrous nanostructures have relatively uniform diameters (30-90 nm) and did not observe a wide range of variation in size distribution. This agrees with the characteristics of nanoparticle formation through homogenous nucleation, which tends to generate monosized nanoparticles.

The laser pulse repetition rate plays a critical role in the formation of nanofibrous like structure. Figure 5.11 shows SEM Images of the magnetic weblike nanofibers generated at 4, 8, 13 and 26 MHz pulse repetition rate. The average diameters of the generated nanofibers were around 70, 60, 45 and 30 nm, respectively. Figure 5.12(a) shows the TEM image of magnetic nanofibers at 26MHz pulse repetition rate and Figure 5.12(b) shows a single magnetic nanofiber generated by femtosecond laser. It depicts that magnetic nanofibers possess weblike structures with diameter no more than 30 nm. Further EDX analysis of the irradiated surface shows existence of Oxygen

as shown in Fig. 5.13 which indicates, besides the percentage of Oxygen to neodymium-iron-boron, the existence of oxidized magnetic nanofibers [180].

The total magnetization of a nanofiber is given by the vectorial sum of all single magnetic moments of the atoms [181]. As for the atomic magnetic moments in generated nanofibers, the average magnetization will be zero in the absence of magnetic field since all magnetic moments are randomly directed in space. When a magnetic field is applied by the substrate, the magnetic moments will orient in the direction of the field and give rise to a net magnetization of the nanofibers. Magnetic field microscopy, from NT-MDT, (MFM) image of the weblike nanofibers structurs generated at 26 MHz is shown inFigure 5.14.The NdFeB nanofibers exhibit magnetic properties (darker parts) as shown in the MFM image of Figure 5.14 which are distinguishable from the background (brighter parts).
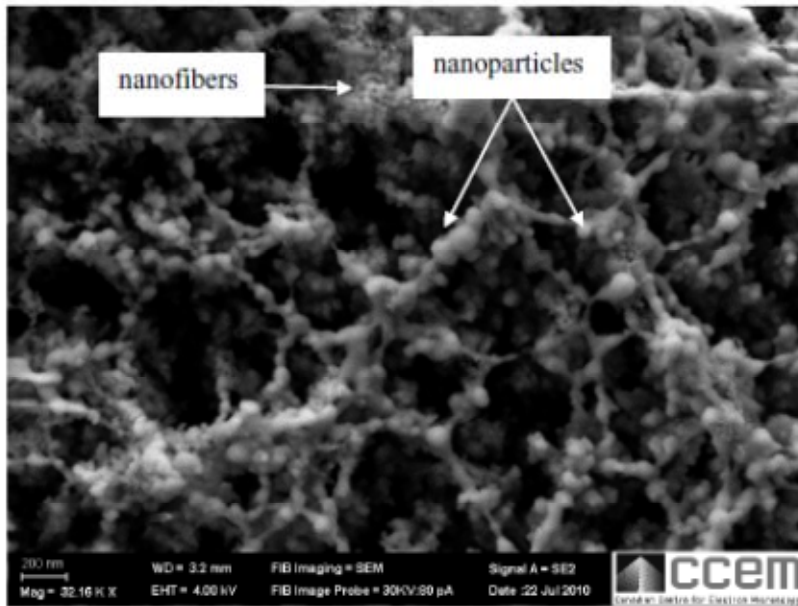
Figure 5.10 SEM image of magnetic nanofibrous structure and nanoparticles on NdFeB substrate irradiated with femtosecond laser at 26 MHz repetition rate and 15 W average power.
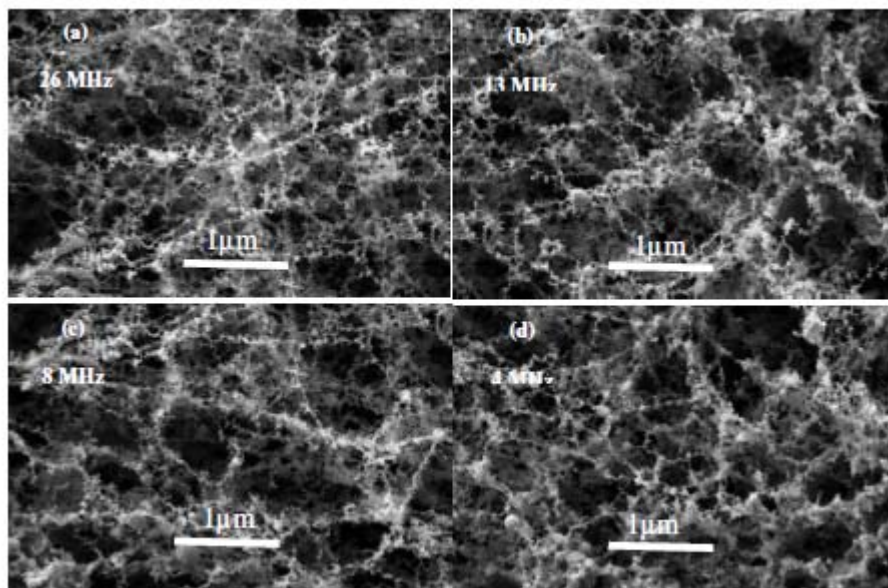
Figure 5.11 SEM images of the generated nanofibers, (a) 26 MHz, (b) 13 MHz, (c) 8 MHz and (d) 4MHz.
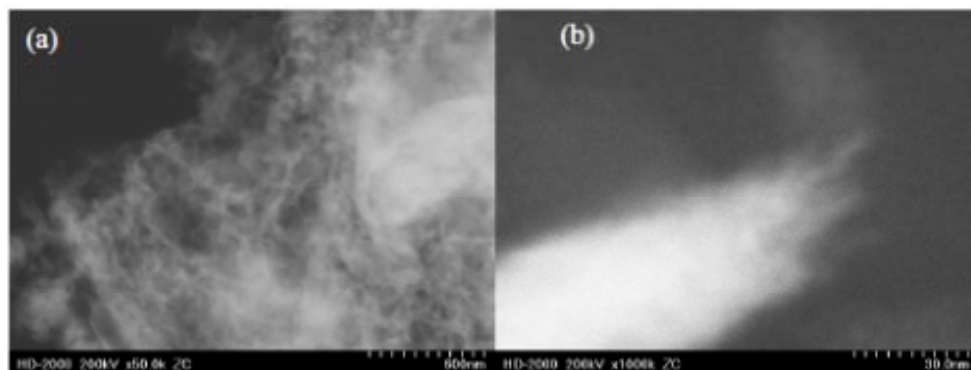
Figure 5.12 TEM images of magnetic nanofibers generated by femtosecond laser at 26 MHz pulse repetition rate and 15 W power.
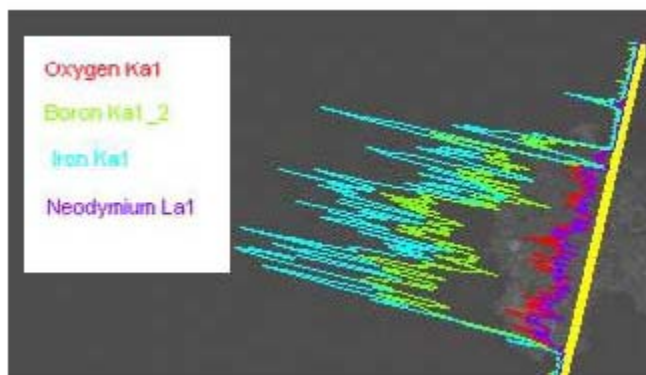
Figure 5.13 EDX analysis of magnetic nanofibers structures.
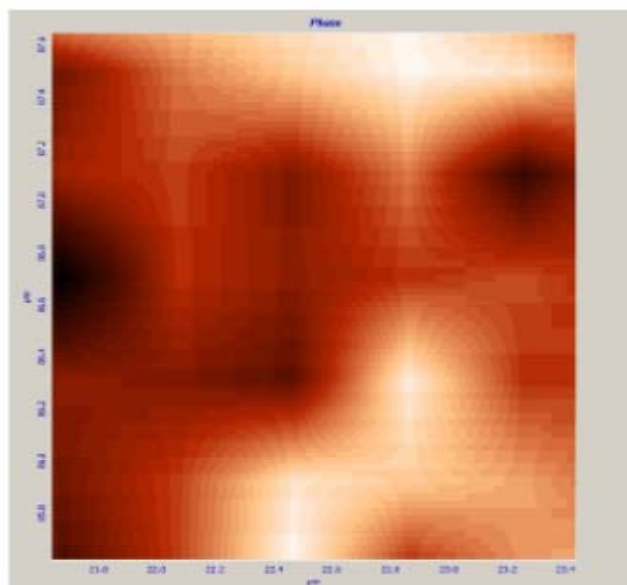
Figure 5.14 MFM image of NdFeBnanofibrous structures formed upon irradiation of laser at 26 MHz pulse repetition rate.

The laser pulse repetition rate plays a critical role in the formation of magnetic nanofibrous structure [182]. In order for nanoparticles to aggregate and form fibrous structure, a continuous supply of vapor is required to maintain the nucleus density of the expanding plume. Nanoparticles generated from the successive laser pulse are fused to the particles created from the previous laser pulse that are still above the melting temperature and grow as nanofibrous like structure as shown in Figure 5.10. As the pulse repetition rate of the femtosecond laser increases, the time between successive pulses decreases which gives less time for clusters to agglomerate and generate nanofibers with smaller diameter. It is evident from the SEM images shown in Figure 5.11 (a,b,c, and d) that smaller size nanofibers was generated with the increase of the laser pulse repetition rate.

Characterization was performed using XRD as a function of femtosecond laser pulse repetition rate. Figure 5.15 shows XRD pattern of NdFeB magnetic nanofibers generated by femtosecond laser at 26 MHz and a power of 15 W. The average nanofibers size is about 28.5nm

estimated from the XRD peaks using the Scherrer formula [183]. This value is consistent with nanofiber size obtained by TEM analysis as shown in Figure 5.12. In comparison, the size of nanofibers prepared using the conventional methods is around 40 nm which is slightly bigger than our method and do not have the weblike structure [184]. Figure 5.16 shows the XRD patterns for magnetic nanofibers generated at 4, 8, 13 and 26 MHz repectively. For the non irradiated area in Figure 5.16, no diffraction peaks indexed by the Nd2Fe14B phase were observed. However, the peaks from Nd2Fe14B phase can be observed clearly in the samples irradiated with femtosecond laser. For the area irradiated with laser at 26 MHz, the peak from α-Fe was mainly found. Therefore, it is considered that the α-Fe peak is attributed to the surface oxidation and it is existed on the surface of the sample.

Figure 5.17 shows the experimental and theoretical relationship between laser pulse repetition rate and magnetic nanofibers size. The nanostructures were generated as a result of nanoparticle agglomeration. As the laser pulse repetition rate increases, the pulse to pulse duration will be shorter and hence less time for agglomeration process is available which results in smaller size fibrous nanostructure [180].The average nanofiber size can be estimated from the Sherrer equation [183-185]:

$$r = \frac{0.9\lambda}{B\cos\theta} \qquad\qquad (5.15)$$

Where r is the nanofiber size, λ is the X-ray wavelength, B is the full width at half maximum of the peak (FWHM), and θ is the diffraction angle. From the diffraction peaks in Figure 5.16, the average nanofiber size was estimated using the above equation and plotted in Figure 5.17. Those calculations are close to our experimental results as shown in the figure.
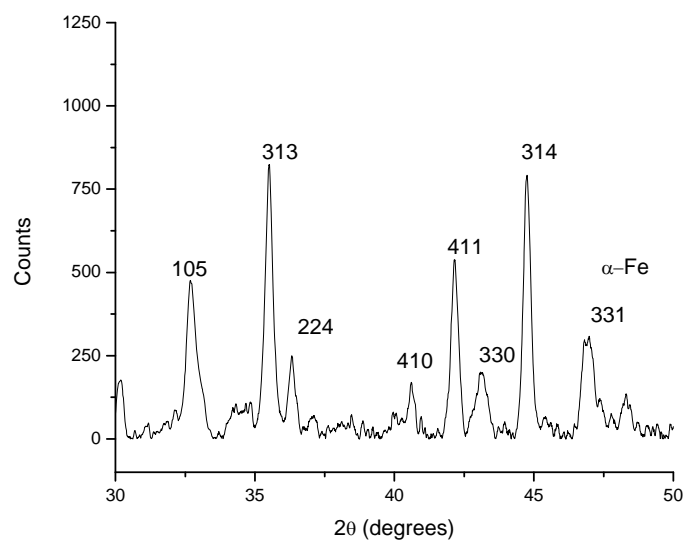
Figure 5.15 XRD pattern of NdFeB magnetic nanofibers generated at 26 MHz and 15 W.
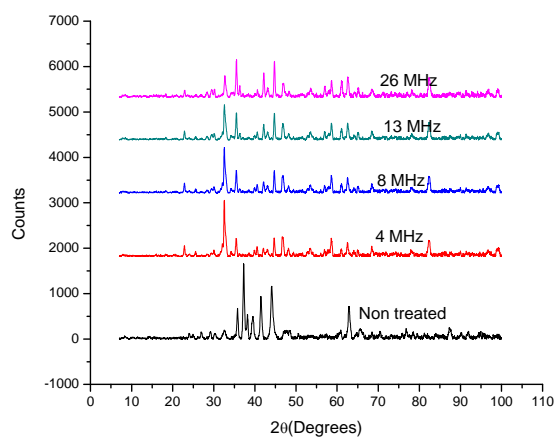
Figure 5.16 XRD patterns for NdFeB magnetic nanofibers generated at 4, 8, 13 and 26 MHz..
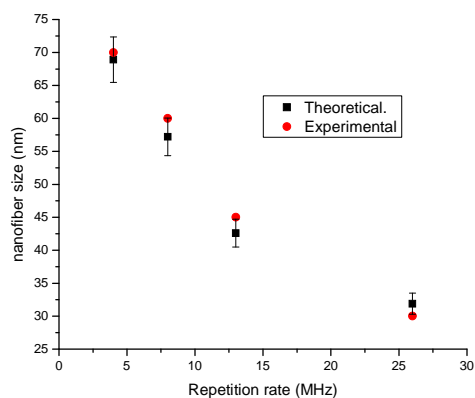
Figure 5.17 Theoretical and experimental magnetic nanofibers size as a function of femtosecond laser pulse repetition rate.

The metastable Nd-rich phase is a grain-boundary phase which has an FCC structure. This grainboundary phase exhibits a characteristic contrast which is similar to a metastable high-pressure phase observed previously as FCCγNd [186]. The structure of the phase is however closely related to that of NdO and it was frequently reported that oxygen content is fundamental in the formation of this phase [187]. However, oxygen-containing FCC phases as shown in Figure 4 were observed only at high temperatures. Therefore, oxygen presence is not critical for the formation of the FCC phase, although at higher temperature this phase may absorb oxygen more easily than other phases because of the high Nd content. Moreover, oxygen can probably stabilize this metastable phase and at higher temperature it can transform into the stable NdO oxide. It was noticed, however, more than three phases can coexist at a given temperature (e.g. at melting point) only if the fourth element was introduced into the ternary system i.e. oxygen in Nd-Fe-B system [188]. The FCC phase is presumably a metastable phase with a structure close to the short-range order in the Nd-rich amorphous phase [189]. It probably forms from the under-cooled substrate with lower melting point than $Nd_2Fe_{14}B$ or from the amorphous phase produced at grain boundaries during the laser ablation process.

Figure 5.18 shows the typical variations of magnetic strength M as a function of laser repetition rate for the NdFeB nanofibers grown at room temperature. The thickness of the generated fibers layer in all of the four pieces were the same [190], however, the morphology of the nanostructures would be changed because of the change in nanofibers size caused by the change in repetition rate. The data were for the samples measured with a Guassmeter along the in-plane direction. The figure indicates that at higher repetition rates, the M of the nanofibrous structure get lower, due to the presence of an abundant amorphousphase which also shows lower coercivity. The relatively large coercivities of nanofiberous structures were due primarily to their

99
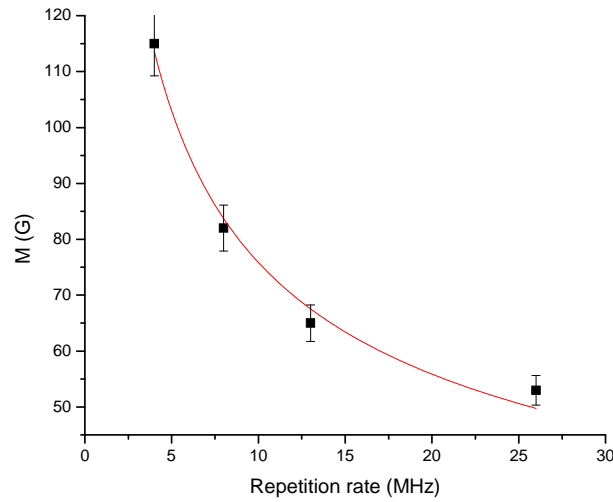
Figure 5.18 Magnetic strength (M), as a function of laser pulse repetition rate

specific morphology. Theory has predicted that a system containing magnetic dipoles that are arranged into a linear chain will exhibitan increase in covercivity [190]. Our results seemed to be consistent with this prediction as long as dipole–dipole interactions between grains played the dominant role in the magnetization process. The NdFeB grains contained in each nanofiber were actually aligned along its long axis, and the dipole–dipole interactions between grains tended to lineup all magnetic dipoles along the same axis.

Figure 5.19 shows the SEM image of magnetic nanocompostie microstructure generated by the new method described in chapter 4. Two photon polymerization methods were used to generate the magnetic microchannels. However, three photon polymerization or DWA could also be used to generate the magnetic microchannels. This is a unique nanocpmposite structure that could be used for biomedical applications as will be discussed in the next section.

Figures 5.20 (a, b and c) show the M-H curves for the magnetic nanofiberous structure alone, polymer (Ormocer on sample) and magnetic nanocomposit respectively. As is expected in
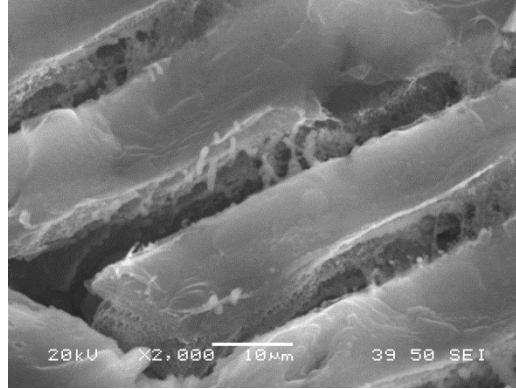
Figure 5.19 SEM image of magnetic nanocomposite microfeatures

ferromagnetic materials, the saturation magnetization MS of the magnetic nanocomposite structures at room temperature is higher than that of the pure polymer. The larger coercivitiesHC we see could be as a result of the oxide Fe. Figure 5.20 (b) shows the room temperature M-H curves for the polymer (Ormocer). It has a weak diamagnetic response to the applied field, but appears to have a small amount of unknown impurity, contributing to a very weak non- linear deviation near zero field that could be a paramagnetic effect. Small traces of paramagnetic impurities are found in nearly all materials, and so it is not surprising in these polymers. However, as we will see, these trace impurities do not affect the quality of our ferromagnetic composites. The magnetic measurements of the nanocomposites are shown in Figure 5.20 (c), which has a coercive field HC of approximately 260 Oe at room temperature. This large coercivity suggests that oxide nanofibrers are present on the microstructure. It can be seen that the magnetization of the generated nanocomposite has been increases compared to pure polymer.

This increase in remnant magnetization is expected below the superparamagnetic-ferromagnetic transition temperature, which is above 300K for the magnetic nanofibers of average size, 20 nm due to reduced thermal activation energy. Interparticle interactions which

(a)	(b)	(c)
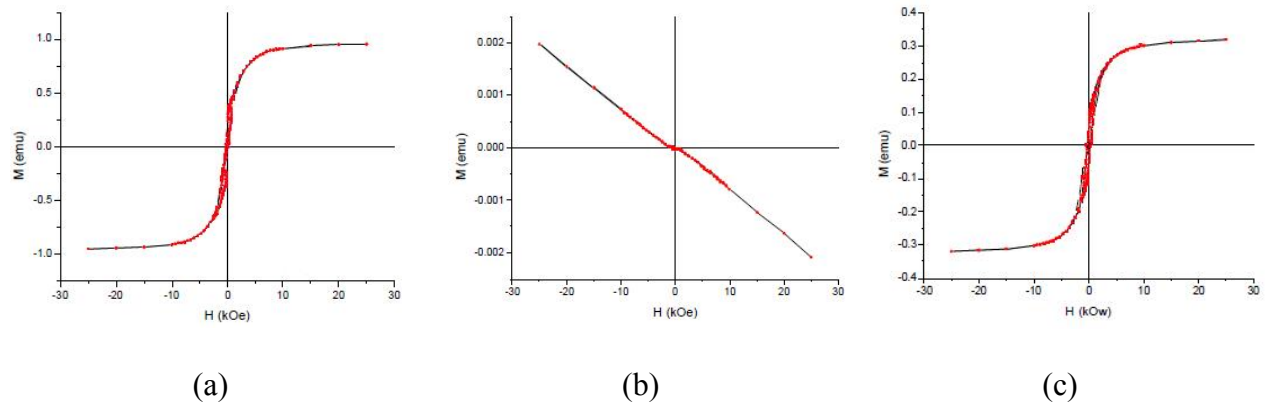
Figure 5.20. Room temperature M-H curves (a) Magnetic nanofiberous structures, (b) Ormocer, and (c) magnetic nanocomposite.

depend on the iron concentration in the polymer matrix, strongly influence the remnant magnetization. Since agglomeration of nanoparticles into nanofibers is observed in all our polymer composite samples, interactions are expected to play a significant role in the magnetic response. These interactions lead to a non- linear increase in MR as the concentration of iron is increased. The magnetic interactions are generally expected to be dipolar in nature, although in strongly coupled clusters, exchange interactions are also possible [191].

5.4   SUMMARY

In this chapter, some of the mechanical, electrical, and magnetic properties of microfeatures fabricated with nanofiber-reinforced polymer were evaluated. The effects of the generated nanofibers on the hardness and elastic modulus of the reinforced polymer were investigated by nanoindentation analysis. Results showed that the hardness and elastic modulus significantly increased compared with those for pure polymerized Ormocer. The new method was proposed for fabricating reinforced electrical conductive polymer. CFN's was generated using femtosecond laser which is also could be used to fabricate microstructure on the surface of

the CNF's reinforced polymer. Results showed that increasing the repetition rate causes an increase in the electrical conductivity. This is a direct result of the significant increase in CNF's density when the repetition rate increases, provided that the CNF's content in the polymer is above the percolation threshold. The temperature-conductivity relationship has been also studies in this work. The concept of electrical sensitivity has been introduced to examine how sensitive and to what extent the reinforced polymer resistance responds, after being stimulated by the temperature change. Magnetic nanocompostie microstructure was also fabricated using the new method. The magnetic strength of the generated nanofibers can be controlled by changing the repetition rate of the femtosecond laser.

CHAPTER 6

FABRICATION OF NANOCOMPOSITE MICRO-ELECTRODES FOR THE ELECTROCHEMICAL DNA SENSING

This research work has demonstrated that combining femtosecond laser ablation and polymerization, microstructures of polymer-based nanocomposites can be fabricated. These nanocomposite microstructures demonstrated enhanced properties. This chapter showcases the potential applications of this fabrication method through the creation of a nanocomposite microelectrode for DNA sensing.

6.1   ELECTROCHEMICAL DNA DETECTION

The detection of DNA sequences using electrochemical readout is particularly attractive for the development of clinical diagnostics. Quantitative electrochemical measurements can be established using compact and inexpensive instrumentation as well as covalently labeling DNA samples with reporter groups is often unnecessary, simplifying preparation procedures. Indeed a number of methods exist for the electrochemical detection of DNA, most of which rely on the signal produced by a noncovalently bound redox-active reporter group, that is increased when DNA is hybridized to a surface modified with a probe sequence. However, the sensitivities of

many of these methods are not sufficient for practical applications because small signals are obtained from the finite concentration of a surface-bound species present at the electrode surface.

Electrocatalytic processes can be used to amplify signals produced at DNA modified electrode surfaces to increase the sensitivity and accuracy of the detection assay. The catalytic reaction of the electrochemically generated $Ru(bpy)_3^{3+}$ with guanines contained within a hybridized target provides a powerful tool for the detection of DNA with limitation because of sequence dependence. In addition, electrocatalysis involving an intercalating probe has been used to amplify signal changes reporting the presence of mismatch producing point mutations. However, neither system is ideal for hybridization based detection of closely related sequence.

This work has developed a new electrocatalytic DNA detection assay that reports DNA hybridization and resolves single base changes in the target sequence. The method exploits a reaction between $Ru(NH_3)_6^{3+}$, DNA-binding and redox-active probe and $Fe(CN)_6^{3-}$. $Ru(NH_3)_6^{3+}$ binds to DNA nonspecifically through electrostatic interactions with the phosphate backbone, and therefore the electrochemical reduction of this species yield a signal that reports on the increase of the negatively charged groups at the electrode surface upon hybridization of a target sequence. The signal is amplified by Fe (III) oxidant, which permits Ru (III) to be regenerated for multiple redox cycles. Because the immobilization of probe sequence on gold surfaces appears to amplify the kinetic effects of base mismatches on DNA hybridization, single base changes can be resolved. We have applied this assay towards the detection of genes from Helicobacter pylori, a pathogen implicated in gastric ulcer and cancer.

Further work has been done to investigate the utility of this method by moving it to a new class of three dimensional nanoelectrode (NE) that enable ultrasensitive electrocatalytic nucleic

acid detection assays. These nanofiberous NE's were fabricated using femtosecond laser and they prove to be a novel and useful platform for electrochemical DNA detection. Our studies testing the use of these template structures with our electrocatalytic reporter system revealed that very low detection thresholds for target DNA sequences can be obtained. One factor contributing to the heightened sensitivity is the high signal-to-noise ratio achieved with the large electrocatalytic signals observed at DNA modified nonofibers. We are able to explain the improved sensitivity with evidence illustrating that electrocatalysis at DNA modified gold nanostructures generates amplified signals that are significantly larger than those observed at bulk gold surface. The results presented strongly suggest that the 3D architecture of the nanofibrous structure facilitates the electrocatalytic reaction because of enhanced diffusion occurring around these structures. Effect unique to the nanoscale is shown to underlie the utility of nanofibers for DNA biosensing.

6.1.1 DNA SENSORS BASED ON CONDUCTING REINFORCED POLYMERS

A conducting polymer containing nanofibrous structure can be very sensitive even to small perturbations at the interface, thanks to its high electrical conductivity and electron transfer capabilities when the interface is covered by its film. Biocompatible conducting polymers can be variably modified for immobilization of probe DNA via covalent linking or electrostatic interactions. The conductivity of the conducting polymer electrochemically deposited on the electrode surface can be modulated by changing the pH of the medium, the electrochemical potential, and/or the electrolyte. Because of these characteristics and other advantages, conducting polymers could be utilized extensively for the construction of biosensors including DNA sensors which, to the best of our knowledge, is reported for the first time.

6.1.2   NOBLE METAL NANO/MICROELECTRODES

Noble metals are known to create strong chemical bonds with compounds terminating with a thiol (-SH) group [192]. In order to achieve immobilization of nucleic acids on solid substrates, researchers have developed techniques by which DNA molecules can be linked to a thiol group [193]. In this case, the thiolated terminal of molecules is chemisorbed on the substrate, while the DNA portion of the molecules are standing parallel to each other and away from the substrate. Since they are formed quickly, resulting in a well-defined and reproducible surface, and are stable under normal laboratory conditions, Gold electrodes are fabricated using the femtosecond laser material processing described in chapter 4.

6.1.3   ELECTROCHEMICAL RESPONSE OF NANO/MICROELECTRODES

Cyclic Voltammetry is an electrochemical technique where the potential waveform in Figure 6.1 is applied between the working and reference electrodes and the resultant current is measured between working and auxiliary electrodes to generate a current versus potential curve.
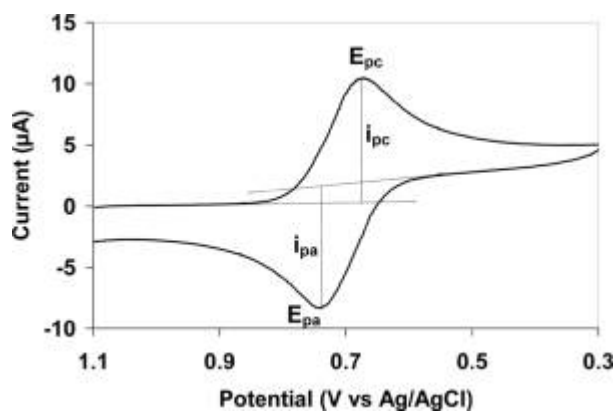
Figure 6.1 Schematic representation of a typical Cyclic Voltammetry (CV) scan of a reducible electrochemical complex [194].

6.2   FABRICATION OF NANOELECTRODES FOR DNA SENSING

The samples (or working electrodes) used were 20×5 mm gold-coated (thickness of 350 nm) silicon wafers of 500 µm thickness. The laser beam is focused on the sample surface with a lens of focal length of 71 mm and scanned using a computer-controlled galvanometer. A computer controls the laser beam to irradiate the sample surface. A polarizer and analyzer are used to rotate and analyze the beam polarization. An acoustic modulator is used for pulse number control. The experiments were carried out in air at atmospheric pressure. The radiation fluence used was 0.5 J/cm^2 at a pulse repetition rate of 25 MHz with an interaction time of 1 ms and with the pulse width of 214 fs. Two sets of samples were prepared with same experimental conditions. One set was used to generate nanofbrous structures inside a 5×5 mm area of the Au/Si wafer. The second set was used to generate a 5×5 square on the Au/Si wafer to guarantee the same dimensions of the first set but with bare gold on the surface. The rest of the wafer was insulated in both sets with insulating material (Ormocore) except for a 2×5 mm area on the opposite side of the laser treated area to allow for electrical connection.

The synthetic oligonucleotides were purchased from Integrated DNA Technologies, Inc. (USA). Their base sequences are: Probe DNA:5- /5ThioMC6-D/ATA AGG CTT CCT GCC GCG CT -3, Complementary target DNA: 5- AGC GCG GCA GGA AGC CTT AT -3and Non-complementary target DNA: 5- TTT TTTTTTTTTTTTTT TT -3. Cyclic voltammetry (CV) measurements were performed with a PalmSense electrochemical sensor (USA). All electrochemical experiments were performed with a conventional three-electrode system. The reference and auxiliary electrodes were purchased from BASi (USA). We used a platinum wire auxiliary electrode, an Ag/AgCl reference electrode, and home-built nanofibrous and unprocessed gold working electrodes.

Figure 6.2 shows a schematic representation of the fabrication procedure of the DNA biosensor. The immobilization of thiolated probe DNA was performed by the deposition of a 100 µL solution containing 5 µM single stranded thiolated DNA, 20 mM MgCl₂, 25 mM sodium chloride and 25 mM phosphate buffer on the planar and nanofirbous modified gold electrodes for one hour in a dark humidity chamber at room temperature.
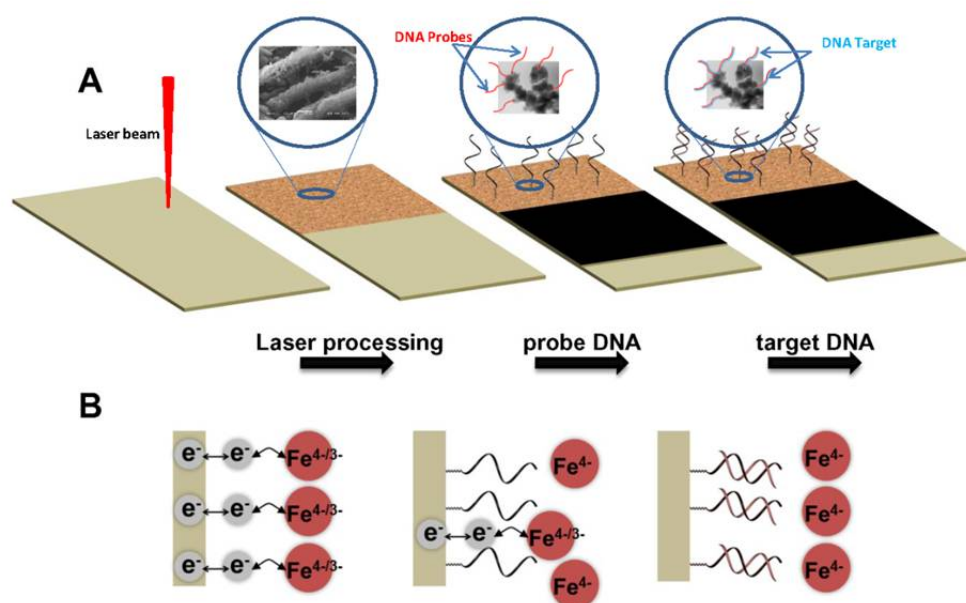
Figure 6.2 Schematic representation of electrochemical DNA detection using gold nanofibrous electrodes (GNE) A. Steps involved in fabricating single stranded DNA-modified GNEs. B. Label-free electrochemical detection using the redox reporter potassium ferrocyanide (Fe^{4-})

Then, the electrodes are washed after probe deposition for 10 minutes using 25 mM sodium chloride (NaCl) and 25 mMphotphate buffer PH 7 solution (25/25). Probe-modified electrodes are scanned in and 2 mM Fe $(CN)_6^{3-}$. Following the first electrochemical readout and washing the electrodes with an aqueous solution of 25 mM sodium chloride and 25 mM phosphate buffer, the two electrode (planar and nanofibrous) are incubated in a dark humidity

chamber with different concentrations of noncomplementary DNA targets in 25 mM sodium chloride (NaCl) and 25 mMphotphate buffer PH 7 solution (25/25) at 37^OC for one hour. Probe-modified electrodes are scanned again in 2 mMF$e(CN)_6{}^{3-}$ and the process is repeated for the complementary and noncomplementary DNA targets. To determine whether any of the on-electrode probe sequences are successfully hybridized, the reductive catalytic current is measured after hybridization. The change in peak reductive current is documented for different probe/target combinations.

6.3   RESULTS AND DISCUSSION

Figure 6.3 demonstrates the cyclic votammagram of processed and unprocessed electrodes in 0.5M H_2SO_4. According to this figure, the effective surface area of nanofibrous modified electrode is about 10 times larger than the area of the planar gold electrode. Whereas, the surface area increase for the common gold nanoparticles electrodeposited electrode is only about 2–4 times compared with that of planar gold electrode [194]. This further indicated that the three-dimensional porous nanostructures created by laser processing largely increased the effective electrode surface area.

Figure 6.4(a) shows the cyclic voltammograms obtained for the modified electrodes in 1mM $Fe(CN)_6{}^{3-}$ solution at the scan rate of 100mV/s. A pair of redox peaks was observed on the nanofibrous modified electrode with the anodic (E_{pa}) and cathodic (E_{pc}) peak potential of 0.08V and 0.42 V, respectively. After probe DNA immobilization on the nanofibrous modified electrode, the peak current of $Fe(CN)_6{}^{3-}$ was largely inhibited and the peak to peak potential

110
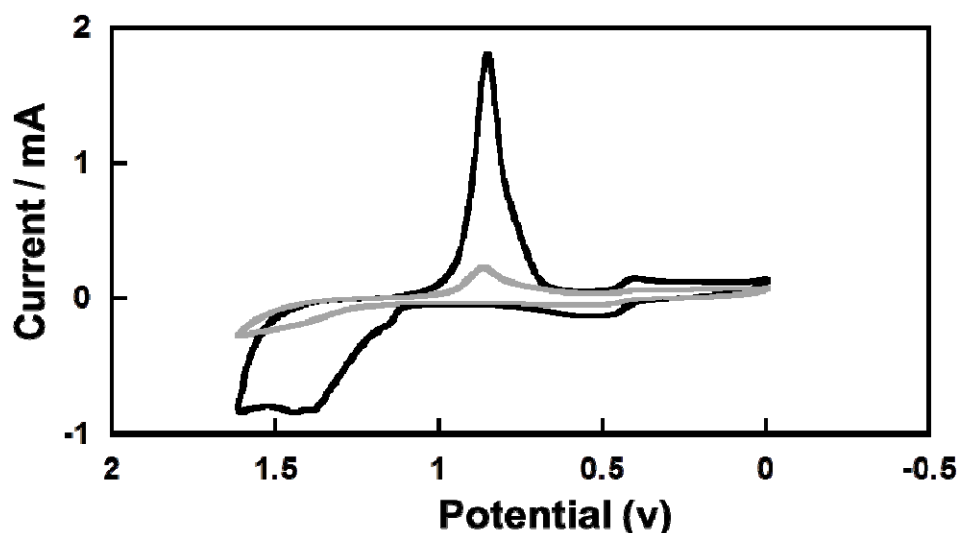
Figure 6.3 Cyclic voltammogram in H_2SO_4 of gold electrode before (gray) and after laser processing and creation of gold nanofibres.

separation (ΔE_p) was largely increased. This could be explained by electrostatic repulsion of $Fe(CN)_6^{3-}$ from the negatively charged DNA film. This behavior is line with results described in literature in immobilization of DNA on gold macroelectrodes [195].A further decreased peak current and increased ΔE_p was observed after hybridization of probe DNA with target complementary DNA. This could be well assigned that the introduction of complementary DNA increases the negative charge responsible for the increased repellence of redox species. The same experiment was done with the noncomplementary DNA. However, there is no significant decrease in the voltammetric signals of non-complementary compared to the complementary DNA and also these signals are close to the ssDNA probe signal.

To evaluate the performance of nanofibrous modified electrode, the peak current change before and after hybridization of probe DNA with complementary target DNA was further studied. The peak current of $Fe(CN)_6^{3-}$ on the nanofibrous electrode decreases with the increasing target DNA concentration ranged from 1 fM to 1 μM as shown in Figure 6.44(b). The

111

peak current change of fabricated DNA sensor exhibited a linear correlation to the logarithm of the target DNA concentration ranged from 1 fM to 1μM as shown in Figure 4(b). The obtained low detection limit between 1-100 fM, is among the lowest label-free and single step methods reported to date [196].

In order to demonstrate that the enhanced detection limit of the gold nanofibrous electrode is indeed related to its unique structure, we compared its performance to an unprocessed gold electrode of the same geometric area. The peak reduction current of the ferrocyanide reporter at the gold nanofibrous electrode is larger than the unprocessed electrode as shown in figure 6.5. This is expected due to the enhanced surface area of the nanofibers as demonstrated in Figure 4. The more striking result is that in addition to the higher current, which can lead to a higher signal to noise ratio, there is a larger signal change when negatively charged DNA molecules interact with nanofibrous electrodes rather than unprocessed electrodes. This is true for both cases of deposition of DNA probes – 15 % instead of 2%- and capture of DNA targets – 56% instead of 27%.
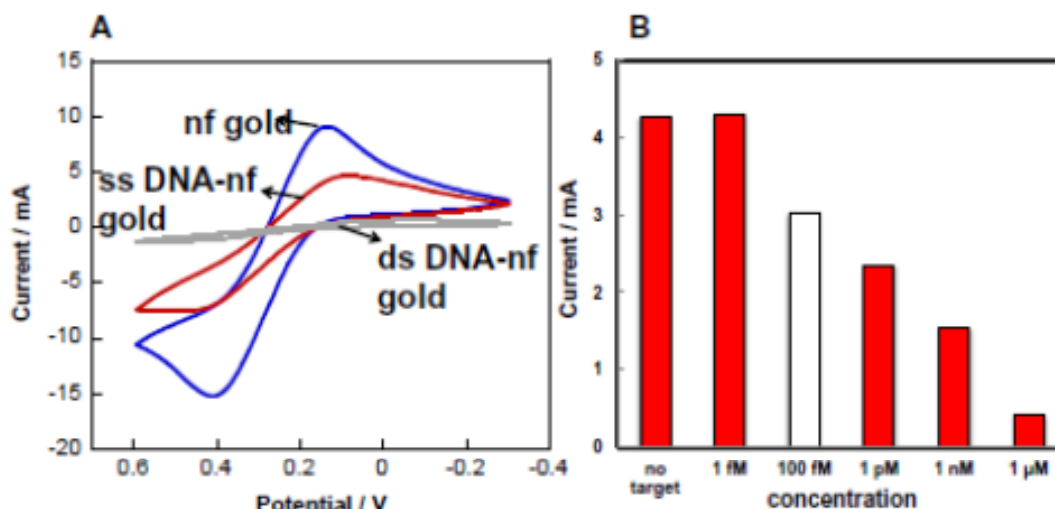
Figure 6.4. Detection of DNA hybridization using GNEs. A. Cyclic voltammogram, B, detection limit of the GNEs.

The nanofibrous modified electrode with a huge surface area to volume ratio was considered to supply numerous attaching points for probe DNA immobilization. As well as, the immobilization orientation and assembly density of probe DNA may be well controlled by three-dimensional weblike structure of nanofibers for optimized hybridization efficiency. On the other hand, the hierarchical three-dimensional weblike structure in present case may diminish the repelling behavior when approaching of the target DNA towards the immobilized probe DNA and enhance the hybridization efficiency. The role of nanofibers in the sensitivity improvement can be explained by the small size of the generated nanofibers, which could be as small as 2 nm, and the weblike kind of nanofibrous structure which would increase number of probe DNA per unit area and hence, increase the probability of hybridization.
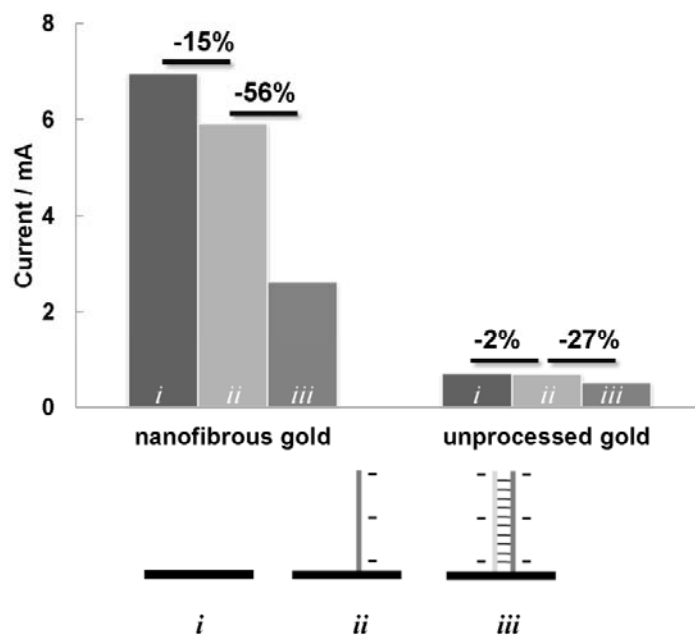
Figure 6.5 Comparison of gold nanofibrous electrodes with unprocessed gold electrodes in detection of 100fM complementary target. i,ii,iii represent the measurements performed on bare electrodes, ssDNA modified electrodes, and dsDNA modified electrodes respectively.

113

6.4   SUMMARY

An electrochemical DNA biosensor based on 3D stand free nanofibrous electrodes for sensitive DNA sequence detection has been constructed. The nanofibrous structures largely increase the electrode surface area by about 10 times compared with that of bare gold electrode. The biosensor fabrication process was thoroughly investigated with cyclic voltammetry using $Fe(CN)_6^{3-}$ as an electrochemical redox probe. The 3D gold nanostructure has a significant impact on increasing the immobilization amount of probe DNA and further hybridization amount with target DNA. The target DNA sequence could be quantified over the range from 1 fM to 1nM. This nanofibrous biosensor could be used for the detection of target DNA in real biological and clinical samples and it could be further modified for applications in detection of cancers and infectious diseases. This work demonstrated a potential application of the fabrication method developed through this thesis work.

CHAPTER 7

CONCLUSIONS AND FUTURE WORK

The use of organic or inorganic filler has become ubiquitous in polymeric systems. Polymer composites are manufactured commercially for many diverse applications such as sporting goods, aerospace components, automobiles, etc. In the last 20 years, there has been a strong emphasis on the development of polymeric nanocomposites, where at least one of the dimensions of the filler material is of the order of a nanometer. The final product does not have to be in nanoscale, but can be micro- or macroscopic in size. Most of the widely used methods for microfabrication of nano-phased structural polymer nanocomposite microfeatures are complicated and the mechanical properties of these microfeatures are poor due to voids and the nonuniformity of final product.

7.1   CONCLUSIONS

This thesis work developed a new method for the formation of microfeatures with reinforced polymerusing femtosecond laser material processing. The femtosecond laser was used for both the generation of a three-dimensional interweaved nanofiber and the construction of microfeatures, such as microchannels and voxels, through multiphoton polymerization of a nanofiber-dispersed polymer resin. Two photon polymerization and multiphoton polymerization was used to solidify nanofiber dispersed resins to construct microfeatures. microstrucures of various properties have been fabricated with this method. The hardness and elastic modulus of

the nanocomposites have improved by 25% and 75%, respectively, with the incorporation of nanofibers using the described method, which has the potential of direct fabrication of reinforced micro/nanostructures. The new method was capable of fabricating nanofibers reinforced electrical conductive polymer microfeatures. It was found that in temperature range of 20-140 ^{o}C, the conductivity decreased with the increase of temperature. The electrical conductivity of the reinforced polymer increases with the increase in the repetition rate of the femtosecond laser. The new method was also used to fabricate magnetic nanocompostie microstructure. A non-linear increase in magnetic response (MR) of the fabricated microfeatures as the concentration of iron is increased. Finally, this new method was used for direct fabrication of reinforced nanostructured DNA biosensor. The new biosensor is capable of multiplexed, sensitive, high-dynamic range and rapid detection of specific nucleic acids contained in cells. The main contributions are summarized below:

1. A new method for the formation of rapid prototyping of microfeatures with the nanofiber-reinforced polymer.

2. A new phenomenon of dual wavelength multiphoton absorption (DWA). This phenomenon induces two temporally separated femtosecond laser pulses of different wavelengths to generate microstructures via multiphoton polymerization. This process allows the fabrications of 2D and 3D components with improved resolution.

3. Electrical sensitivity polymer mcirostructure was fabricated and test showed that this structure demonstrated wider work range compare to state of the art ones.

4. An electrochemical DNA biosensor based on 3D stand free nanofibrous electrodes for sensitive DNA sequence detection was constructed. The obtained low detection limit of the DNA biosensor between 1-100 fM, is among the lowest label-free and single step

116

methods reported to date. The more striking result for the DNA biosensor is that in addition to the higher current, which can lead to a higher signal to noise ratio, there is a larger signal change when negatively charged DNA molecules interact with nanofibrous electrodes rather than unprocessed electrodes. This is true for both cases of deposition of DNA probes – 15 % instead of 2%- and capture of DNA targets – 56% instead of 27%.

7.2   FUTURE WORK

This section provides an overview of the remaining challenges in developing practical biosensing devices. Addressing such challenges involves defining research problems that can be addressed by researchers involved in engineering, chemistry, biochemistry and materials research.

- Performing further studies in mechanical, electrical, thermal, magnetic enhancement, particularly by controlling the concentrations of chemicals delivered to the polymer and study the response of the nanocomposites to the exposure to increasing concentrations of chemicals.

- Continue the optimization of nanocomposites by finding the laser parameters that give highest diffraction efficiency and by finding the best experimental conditions (such as recording intensity and exposure time) to record reflection holograms.

- It is recommended that a mathematical model is developed with the capability of analyzing and predicting the size of voxel for any given combination of process parameters and material characteristics.

APPENDIX A

MATLAB CODES FOR TEMPERATURE

DISTRIBUTION

```
clc

clear

ra=20e-6;

nr=30;

zf=1e-3;

[z1,Io] = ode45(@Intensityrkt,[0 zf],[1e15]);

lg=length(Io);

Ir=flipud(Io);

z=0:zf/(lg-1):zf;

zr=-zf:zf/(lg-1):0;

plot (zr,Ir,'g',z,Io,'g')

lemda=1060e-9; wo=10e-6;

zr=pi*wo^2/lemda;

wz=wo*(1+(z/zr).^2).^0.5;

r=0:ra/(nr-1):ra;

theta=0:2*pi/(nr-1):2*pi;

[R,THETA]=meshgrid(r,theta);

rl=length(R);

tl=length(THETA);
```

```matlab
for i=1:rl

    for j=1:tl

        Z(i,j)=Io(1)*exp(-2*r(i)^2/wz(1)^2);

    end

end

X=R.*cos(THETA);

Y=R.*sin(THETA);

surf(X,Y,Z')


function dydt = Intensityrkt(t,y)

dydt = -1e-17*(y(1))^3;


function dT = rigid(tm,T)


nr=100;nz=50;

radius=0.01;depth=0.05;

dr=radius/nr;dp=2*pi;dz=depth/nz;

Tamb=20; k=50;rho=7800;c=470;

ii=1;

dT = zeros(nr*nz,1);    % a column vector

B=zeros(size(dT));

for i=1:nz

for j=1:nr

    rm=dr/2+(j-1)*dr;
```

```matlab
if j==1

    Rmm=inf;

else

    dv=rm*dr*dp*dz;

    Rmm=dr/((rm-dr/2)*dp*dz*k);

end

if j==nr % boundry conditions

    dv=rm*dr*dp*dz/2;

    Rmp=dr/((rm+dr/4)*dp*dz*k);

else

    dv=rm*dr*dp*dz;

    Rmp=dr/((rm+dr/2)*dp*dz*k);

end

if i==1

    dv=rm*dr*dp*dz/2;

    Rkm=dz/(2*rm*dp*dr*k);


else

    dv=rm*dr*dp*dz;

    Rkm=dz/(rm*dp*dr*k);

end

if i==nz

    dv=rm*dr*dp*dz/2;

    Rkp=dz/(2*rm*dp*dr*k);
```

```
else

    dv=rm*dr*dp*dz;

    Rkp=dz/(rm*dp*dr*k);

end

if (((i>1)&(i<nz)) & ((j>1)&(j<nr)))

    Ci=rho*c*dv;

    A(ii,ii)=-1/Ci*(1/Rmp+1/Rmm+1/Rkp+1/Rkm);

    A(ii,ii+1)=1/Ci/Rmp;

    A(ii,ii-1)=1/Ci/Rmm;

    A(ii,ii+nr)=1/Ci/Rkp;

    A(ii,ii-nr)=1/Ci/Rkm;

    B(ii,1)=0;ii=ii+1;

elseif ((i==1) & ((j>1)&(j<nr)))

    Ci=rho*c*dv;

    A(ii,ii)=-1/Ci*(1/Rmp+1/Rmm+1/Rkp+1/Rkm);

    A(ii,ii+1)=1/Ci/Rmp;

    A(ii,ii-1)=1/Ci/Rmm;

    A(ii,ii+nr)=1/Ci/Rkp;

    B(ii,1)=Tamb;ii=ii+1;

elseif ((i==nz)& ((j>1)&(j<nr)))

    Ci=rho*c*dv;

    A(ii,ii)=-1/Ci*(1/Rmp+1/Rmm+1/Rkp+1/Rkm);

    A(ii,ii+1)=1/Ci/Rmp;

    A(ii,ii-1)=1/Ci/Rmm;
```

121

```matlab
    A(ii,ii-nr)=1/Ci/Rkm;

    B(ii,1)=0;ii=ii+1;

elseif ((j==1) & ((i>1)&(i<nz)))

    Ci=rho*c*dv;

    A(ii,ii)=-1/Ci*(1/Rmp+1/Rmm+1/Rkp+1/Rkm);

    A(ii,ii+1)=1/Ci/Rmp;

    A(ii,ii-nr)=1/Ci/Rkm;

    A(ii,ii+nr)=1/Ci/Rkp;

    B(ii,1)=0;ii=ii+1;

elseif ((j==nr) & ((i>1)&(i<nz)))

    Ci=rho*c*dv;

    A(ii,ii)=-1/Ci*(1/Rmp+1/Rmm+1/Rkp+1/Rkm);

    A(ii,ii-1)=1/Ci/Rmm;

    A(ii,ii-nr)=1/Ci/Rkm;

    A(ii,ii+nr)=1/Ci/Rkp;

    B(ii,1)=0;ii=ii+1;

elseif ((i==1) & (j==1))

    Ci=rho*c*dv;

    A(ii,ii)=-1/Ci*(1/Rmp+1/Rmm+1/Rkp+1/Rkm);

    A(ii,ii+1)=1/Ci/Rmp;

    A(ii,ii+nr)=1/Ci/Rkp;

    B(ii,1)=Tamb;ii=ii+1;

elseif ((i==1) & (j==nr))

    Ci=rho*c*dv;
```

```
        A(ii,ii)=-1/Ci*(1/Rmp+1/Rmm+1/Rkp+1/Rkm);

        A(ii,ii-1)=1/Ci/Rmm;

        A(ii,ii+nr)=1/Ci/Rkp;

        B(ii,1)=Tamb;ii=ii+1;

    elseif ((i==nz) & (j==1))

        Ci=rho*c*dv;

        A(ii,ii)=-1/Ci*(1/Rmp+1/Rmm+1/Rkp+1/Rkm);

        A(ii,ii+1)=1/Ci/Rmp;

        A(ii,ii-nr)=1/Ci/Rkm;

        B(ii,1)=0;ii=ii+1;

    elseif ((i==nz) & (j==nr))

        Ci=rho*c*dv;

        A(ii,ii)=-1/Ci*(1/Rmp+1/Rmm+1/Rkp+1/Rkm);

        A(ii,ii-1)=1/Ci/Rmm;

        A(ii,ii-nr)=1/Ci/Rkm;

        B(ii,1)=0;ii=ii+1;

    end

end

end

B

dT=A*T-A*B;
```

REFERENCES

[1]   Uppal, N., Shiakolas, S. (2008) Modeling of Temperature-Dependent Diffusion and Polymerization Kinetics and their Effects on Two-Photon Polymerization Dynamics. *J MicroNanolith MEMS MOEMS* Volume. 7, Issue: 4, Pages: 43002.

[2]   Wing, Y., Yu, Z. (2006) Polymer nanocomposites. Woodhead publications.

[3]   Koo, J. (2008) Polymer nanocomposites. McGraw hill,

[4]   Li, J., Lawrence, S. (2008) Sub-resolution assist feature for modern photolithography process simulation. *Japanese Journal of App Physics*. Vol.47, pp.6; 4862-4865.

[5]   Sun, C., Zang, X. (2002) Experimental and numerical investigations on microstereolithography of ceramics. *Journal of App Physics*. Vol.92, pp. 8.

[6]   Bertsch, A, Renaud, P., Lorenz H. (1998) Combining microstereolithography and thick resist UV lithography for 3D microfabrication. *Proc IEEE MEMS*. pp. 18-23.

[7]   Schmidt, A., Ehrfeld, W. (1992) Recent developments in deep X-Ray Lithography. *J Vac Sci Technol B*. Vol. 10(1), pp.278-285.

[8]   Cohen, A, Zhang, G., Tseng, F.-G., Frodis, U., Mansfeld, F., Will, P. (1999) EFAB: Rapid, low-cost desktop micromachining of high aspect ratio true 3-D MEMS. *Proc IEEE MEMS*. pp. 244-51.

[9]   Madden, J., Hunter, I. (1996) Three dimensional microfabrication by localized electrochemical deposition. J *Microelectromech Syst.* Vol. 5(1) pp.24-32.

[10] Barcikowiski, S., Hustedt, M., Chichkov, B. (2008) Nanocomposite manufacturing using ultrashortpulsed laser ablation in solvents and monomers. *Polymery*. pp. 657-662Z.

[11] Sun, Y., Dong, X., Nakanishi, S., Chen, W., Duan X., Kawata, S. (2007) Log-pile photonic crystal of CdS-polymer nanocomposite fabricated by combination of two-photon polymerization and in situ synthesis. *Appl. Phys*. Vol. A86, pp. 427-431.

[12] Hong, L., Pan, T., (April 2010) Photopatternable Superhydrophobic. *Journal of Microelectromechanical systems*. J Vol. 19, No.2, pp. 246-254.

[13] Maleka, C., Saileb, V. (2004) Applications of LIGA technology to precision manufacturing of high-aspect-ratio micro-components and systems: a review. *Microelectronics Journal*. Vol. 35, pp.131–143.

[14] Marques-Hueso, J., Abargues, R. Valdes, J L., Martinez-Pastor, J.P. (2010) Ag and Au/DNQ-novolac nanocomposites patternable by ultraviolet lithography: a fast route to plasmonic sensor microfabrication. *Journal of material chemistry*. Vol. 20: 35, pp. 7436-7443.

[15] Kondo, R., Takimoto, S. (2002) Suzuki and S. Sugiyama, High aspect ratio electrostatic micro actuators using LIGA process *Microsystem Technologies*. Vol. 6, Number 6, pp. 218-221.

[16] Ouyang, M., Bai R., Xu, Y., Zhang, C., MA, C., Wang, M., Chen, H. (2009) Fabrication of polypyrrole/TiO2 nanocomposite via electrochemical process and its photoconductivity *Transactions of Nonferrous Metals Society of China*. Vol. 19, Issue 6, pp. 1572-1577.

[17] Wana, S., Wang, L., Xue, Q. (2010) Electrochemical deposition of sulfur doped DLC nanocomposite film at atmospheric pressure *Electrochemistry Communications*. Vol. 12, Issue 1, pp. 61-65.

[18] Chen, D.Z., Lao S., Koo, J.H., Londa, M., Alabdullatif, Z. (2010) Powder Processing and Properties Characterization of Polyamide 11-Graphene anocomposites for Selective Laser Sintering *Proc. 2010 SFF Symposium*, Austin, TX.

[19]   Gad-el-Hak, M. (2005) The MEMS Handbook. Second Edition. Virginia Commonwealth University. CRC press, USA

[20] Murray, P.T., Koehler, B., Schreiber, J. (2006) Nanomaterials produced by laser ablation techniques Part 1-synthesis and passivation of nanoparticles. *Proc, Of SPIE*. Vol. 6175, 61750D.

[21] Koehler, B., Murray, P., Shin, E., Schreiber, J. (2006) Nanomaterials produced by laser ablation techniques Part 2-high-spatially resolved nondestructive characterization of nanostructures. *Proc. Of SPIE*. Vol. 6175, 61750C.

[22] Gubin, S P., Yu, Y., Kosobudsky, I D. (2005) Nanomaterials based on metal-containing nanoparticles in polyethylene and other carbon-chain polymers. *Int. J Materials and product tech.* Vol. 23.

[23] Varga, Z., Feher, J., Filipcsei, G., Zrinyi, M. (2003) Smart Nanocomposite polymer gels. *Macromol. Symp.* Vol. 200, pp. 93-100.

[24] Goppert-Mayer, M. (1931) Elementary processes with two quantum jumps. *Annalen der Physik*. (Berlin, Germany) Vol. 9, pp. 273-94.

[25] Kaiser, W., Garrett, C. (1961) Two-Photon excitation in CaF_2: Eu^{2+}. *Physical Review Letters*. Vol. 7, pp. 229.

[26] Sun, H.-B., Kawata, S. (2003) Two-Photon Laser Precision Microfabrication and Its Applications to Micro-Nano Devices and Systems. *Journal of Lightwave Technology*. Vol. 21, pp. 624.

[27] Baldacchini, T., Chen, H., Farrer, R. A., Previte M. J. R., Moser, J., Naughton M. J., Fourkas J. T. (2002) Multiphoton photopolymerization with a Ti:sapphire oscillator *Proceedings of SPIE-The International Society for Optical Engineering*. Vol. 4633, pp. 136.

[28] Baldacchini, T., Farrer, R. A., Moser, J., Fourkas, J. T., Naughton, M. J. (2003) Replication of Two-Photon-Polymerized Structures with Extremely High Aspect Ratios and Large Overhangs *Synthetic Metals*. Vol. 11 pp.135-136.

[29] Baldacchini, T., Fourkas, J. T. (2004) Three-Dimensional Nanofabrication Using Multiphoton Absorption. Marcel Dekker: New York.

[30] Baldacchini, T., LaFratta, C. N., Farrer, R. A., Teich, M. C., Saleh, B. E. A., Naughton, M. J., Fourkas, J. T. (2004) Acrylic-based resin with favorable properties for three-dimensional two-photon polymerization *Journal of Applied Physics*. Vol. 95, 6072.

[31] Lee, K-S., Kim, R H., Yang, D., Park, S. (2008) Advances in 3D nano/microfabrication using two-photon polymerization. *Prog. Polym. Sci*,Vol. 33, pp. 631-681.

[32] Lee, K-S., Kim, R H., Yang, D., Park, S. (2006) Recent developments in the use of twophoton polymerization in precise 2D and 3D microfabrications. *Polym. Adv. Technol*. Vol. 17, pp. 72-82.

[33] Serbin, J., Chichkov, B. N. (2003) Three-dimensional nanostructuring of hybrid materials by twophoton polymerization. *Proc of SPIE*. Vol. 5222.

[34] Ovsianikov, A., Doraiswamy, A., Narayan, R., Chichkov, B. N. (2007) Two- photon polymerization for Fabrication of Biomedical Devices. *Proc of SPIE*. Vol. 6465.

127

[35] Serbin, J., Fallnich, C., Chichkov, B. N. (2002) Two-photon polymerization with Femtosecond pulsed and fabrication of microoptical devices and photonic crystals. *Pacific Rim Conference on Lasers and Electro-Optics, CLEO - Technical Digest.* pp. 491.

[36] Ueno, K., Juodkazis, S., Shibuya, T., Yokota, Y., Mizeikis, V., Sasaki, K., Misawa, H. (2008) Nanoparticle Plasmon-Assisted Two-Photon Polymerization induced by incoherent excitation source. *J. Am. Chem. Soc.* Vol. 130, pp. 6928-6929.

[37] Yunos, D., Boccaccini, A. R. (2008) Polymer-bioceramic for tissue engineering scaffolds. *Journal of Material Science.* Vol. 43, pp.4433-4442.

[38] Denk, W., Strickler, JH. Webb, W. (1990) Two-photon laser scanning fluorescence microscopy Science. Vol. 248, no 4951, pp. 73-76.

[39] Callis, P. (1997) Two-photon-induced fluorescence. *Annu. Rev. Phys. Chem.* Vol.48, pp.271-279.

[40] LaFratta, C. N. , Walt, D. R. (2008) Very high density sensing arrays. *Chem. Rev. Vol.* 108(2), pp.614–637.

[41] Sun, H. B., and Kawata, S. (2004) Two-Photon Photopolymerization and 3D Lithographic

[42] Microfabrication. In NMR - 3D Analysis Photopolymerization. *Springer.*

[43] Kuebler, S. M., Rumi, M., (2005) Nonlinear Optics. Applications: Three-Dimensional

[44] Microfabrication. In Encyclopedia of Modern Optics. Guenther, R. D., et al. (eds.),

[45] *Academic Press,* San Diego.

[46] Maruo, S., Nakamura, O., Kawata, S. (1997) Three-dimensional microfabrication with two-photon-absorbed photopolymerization. *Optics Letters.* Vol.22, Issue 2, pp.132-134.

[47]   Witzgall, G., Vrijen, R., Yablonovitch, E., Doan, V., Schwartz, B. (1998) Single-shot two-photon exposure of commercial photoresist for the production of three-dimensional structures. *Optics Letters*. Vol. 23, Issue 22, pp.1745-1747.

[48]   Campagnola, P. J., Delguidice D. M., Epling G. A., Hoffacker, K. D., Howell, A. R., Pitts, J. D., Goodman, S. L., (2000) 3-dimensional submicron polymerization of acrylamide by multiphoton excitation of xanthene dyes. *Macromolecules*. Vol.33(5), pp.1511–1513.

[49]   Baldacchini, T., Sun, Y., Naughton, M. J. LaFratta, C. N., Baldacchini, T., Fourkas, J. T., Stewart, J., Saleh, B. E. A., Teich, M. C. (2005) Polymer microcantilevers fabricated via multiphoton absorption polymerization. *Appl. Phys. Letter*. Vol.86, 064105; doi:10.1063/1.1863414 (3 pages)

[50]   Serbin, J., Egbert, A., Ostendorf, A., Chichkov, B. N., Houbertz, R., Domann, G., Schulz, J., Cronauer, C., Fröhlich, L., Popall, M. (2003) Femtosecond laser-induced two-photon polymerization of inorganic organic hybrid materials for applications in photonics. *Optics Letters*. Vol.28, Issue 5, pp.301-303.

[51]   Wang, I., Bouriau, M., Baldeck, P., Martineau, C., Andraud, C. (2002) Three-dimensional microfabrication by two-photon-initiated polymerization with a low-cost microlaser. *Optics Letters*. Vol.27, Issue 15, pp.1348-1350.

[52]   Belfield, K., Ren, X., Van Stryland, E., Hagan, D., Dubikovsky, V. (2000) Near-IR Two-Photon Photoinitiated Polymerization

[53]   Using a Fluorone/Amine Initiating System, J. Miesak. *J. Am. Chem. Soc*. Vol.122, pp 1217

[54]   Yang, D., Jhaveri, S., Ober, C. (2005) Three-Dimensional Microfabrication by Two-Photon Lithography. *MRS Bull.* Vol.30, pp.976-982

[55]   Baldacchini, T., Fourkas, J. T. (2004) Three-Dimensional Nanofabrication Using Multiphoton Absorption. In Encyclopedia of Nanoscience and Nanotechnology, J. A. Schwarz, C. I. Contescu, and K. Putyera, eds. (*Marcel Dekker*, New York) pp.3905-3915.

[56]   Sun, H.-B., Kawata, S. (2003) Two-Photon Laser Precision Microfabrication and Its Applications to Micro-Nano Devices and Systems. *Journal of Lightwave Technology*. Vol.21, Issue 3, pp.624.

[57]   Juodkazis, S., Mizeikis, V., Seet, K., Miwa, M., Misawa, H. (2005) Wo-photon lithography of nanorods in SU-8 photoresist. *Nanotechnology*. Vol.16, pp.846

[58]   Sun, H.-B., Takada, K., Kim, M., Lee, K., Kawata, S. (2003) Scaling laws of voxels in two-photon photopolymerization nanofabrication. *Appl. Phys. Letter*. Vol.83, pp.1104

[59]   Tan, D. F., Li, Y., Qi, F., Yang, H., Gong, Q., Dong, X., Duan, X. (2007) Reduction in feature size of two-photon polymerization using SCR500. *Appl. Phys. Letter*. Vol.90, 071106

[60]   Sun, H.-B., Tanaka, T., Kawata, S. (2002) Three-dimensional focal spots related to two-photon excitation*, Appl. Phys. Letter*. Vol.80, pp.3673

[61]   DeVoe, R. J., Purlys, V., Rutkauskas, M., Gadonas, R. (2003) Two-photon polymerization for fabrication of three-dimensional micro- and nanostructures over a large area. *Proc. SPIE* Vol.4797, pp.7

[62]   Deubel, M., Freymann, G., Wegener, M., Pereira, S., Busch, K., Soukoulis, C. (2004) Direct laser writing of three-dimensional photonic-crystal templates for telecommunications. *Nat. Mater*. Vol.3, pp.444-447.

[63] Serbin, J., Ovsianikov A., Chichkov, B. (2004) Fabrication of woodpile structures by two-photon polymerization and investigation of their optical properties. *Optics Express*. Vol.12, Issue 21, pp.5221-5228.

[64] The, W. H., Dürig, U., Salis, G., Harbers, R., Drechsler, U., Mahrt, R., Smith, C., Güntherodt, H. (2004) SU-8 for real three-dimensional subdiffraction-limit two-photon microfabrication. *Appl. Phys. Letter*. Vol.84, pp.4095

[65] Teh, W. H., Dürig, U., Drechsler, U., Smith, C., Güntherodt, H. (2005) Effect of low numerical-aperture femtosecond two-photon absorption on (SU-8) resist for ultrahigh-aspect-ratio microstereolithography. *J. Appl. Phys*. Vol 97, 054907

[66] Yu, T., Ober, C., Kuebler, S., Zhou, W., Marder, S., Perry, J. (2003) Chemically amplified positive resists for two-photon three-dimensional microfabrication. *Adv. Mater*. Vol.15, pp.517

[67] Klein, S., Barsella, A., Leblond, H., Bulou, H., Fort, A., Andraud, C., Lemercier, G., Mulatier, J., Dorkenoo, K. (2005) One-step waveguide and optical circuit writing in photopolymerizable materials processed by two-photon absorption. *Appl. Phys. Letter*. (2005) Vol.86, 211118

[68] Guo, R., Xiao, S., Zhai, X., Li, J., Xia, A., Huang, W. (2006) Micro lens fabrication by means of femtosecond two photon photopolymerization. *Opt. Express*.Vol.14, pp.810

[69] Sherwood, T., Young, A. C., Takayesu, J., Jen, A., Dalton, L., Chen, A. (2005) Microresonator on Side-Polished Optical Fiber. IEEE Photon. *Technol. Letter*. Vol.17, pp.2107

[70] Yokoyama, S. (2003) Fabrication of three-dimensional microstructure in optical-gain medium using two-photon-induced photopolymerization technique. *Thin Solid Films.* pp.438-439, 452

[71] Sun, H.-B., Takada, K., Kawata, S. (2001) Elastic force analysis of functional polymer submicron oscillators. *Appl. Phys. Letter.* Vol.79.

[72] Duan, X.-M., Suna, H., Kanekoa, K., Kawataa, S. (2004) Two-photon polymerization of metal ions doped acrylate monomers and oligomers for three-dimensional structure fabrication. *Thin Solid Films*. pp.453-454, 518

[73] Ledermann, A., Cademartiri, L., Hermatschweiler, M., Toninelli, C., Ozin, G., Wiersma, D., Wegener, M., Freymann, G, (2006) Three-dimensional silicon inverse photonic quasicrystals for infrared wavelengths. *Nat. Mater*. Vol.5, pp.942.

[74] Tetreault, N., von Freymann, G., Deubel, M., Hermatschweiler, M., Pérez-Willard, F., John, S., Wegener, M., Ozin, G. (2006) New Route towards Three-Dimensional Photonic Bandgap Materials: Silicon Double Inversion of Polymeric Templates. *Adv. Mater.* Vol.18, pp.457.

[75] Bayindir, Z., Sun, Y., Naughton, M., Loretta, C., Baldacchini, T., Fourkas, J., Stewart, J., Saleh, B., Teich, M. (2005) Polymer microcantilevers fabricated via multiphoton absorption polymerization. *Appl. Phys. Letter.* Vol.86, 064105

[76] Sun, H.-B., Takada, K., Kawata, S. (2001) Elastic force analysis of functional polymer submicron oscillators. *Appl. Phys. Letter.* Vol.79, pp.3173

[77] Maruo, S., Korogi, H. (2003) Optically driven micromanipulation tools fabricated by two-photon microstererolithography Mater. *Res. Soc. Symp. Proc*. pp.739, 269

[78] Maruo, S., Ikuta, K., Korogi, H. (2003) Force-controllable, optically driven micromachines fabricated by single-step two-photon microstereolithography. *J. Microelectromech.* Syst. Vol.12, pp.533

[79] Maruo, S., Inoue, H. (2006) Optically driven micropump produced by three-dimensional two-photon microfabrication. *Appl. Phys. Letter*. Vol.89, 144101

[80] Pitts, J. D., Campagnola, P.J. , Epling, G.A. , Goodman, S.L. (2000) Submicron multiphoton free-form fabrication of proteins and polymers: studies of reaction efficiencies and applications in sustained release. *Macromolecules* Vol.33, pp.1514

[81] Basu, S., Wolgemuth, W., and P. J. Campagnola. (2004) Measurement of normal and anomalous diffusion of dyes within protein structures fabricated via multi-photon excited crosslinking. *Biomacromolecules*. Vol.5, pp.2347

[82] Basu, S., Campagnola, P. J. (2004) Enzymatic Activity of Alkaline Phosphatase inside Protein and Polymer Structures Fabricated via Multi-photon Excitation. *Biomacromolecules*. Vol.5, pp.572

[83] Basu, S., Lawrence P. Cunningham, George D. Pins, Katie, A. Bush, Rosa, Taboada, Amy R. Howell, Jun Wang, Paul J. Campagnola. (2005) Multi-photon Excited Microfabrication of Collagen Matrixes Cross-linked by a Modified Benzophenone Dimer: Bioactivity and Enzymatic Degradation. *Biomacromolecules*. Vol.6, pp.1465

[84] Kaehr, B., Shear, J. (2004) Multiphoton fabrication of chemically responsive protein hydrogels for microactuation. *Proc. Natl. Acad. Sci. USA*. Vol.101, 16104

[85] Kaehr, B., N. Ertas, R. Nielson, R. Allen, R. Hill, M. Plenert, and J. B. Shear. (2006) Direct-Write Fabrication of Functional Protein Matrixes Using a Low-Cost Q-Switched Laser. *Anal. Chem*. Vol.78, 3198

[86]   Basu, S., Terasaki, M., Rodionov, V., Campagnola, P. (2005) Multi-photon Excited Microfabrication in Live Cells via Rose Bengal Cross-linking of Cytoplasmic Proteins. *Opt. Letter*. Vol.30, pp.159

[87]   Allen, R., Nielson, D., Wise, D., Shear, J. (2005) Three-Dimensional Protein Architectures. *Anal. Chem*. Vol.77, pp.5089

[88]   Wu, P.-W., W. Cheng, I. B. Martini, B., Dunn, B. J. Schwartz and E. Yablonovitch. (2000) Two-Photon Photographic Production of Three-Dimensional Metallic Structures within a Dielectric Matrix. *Adv. Mater*. Vol.12, pp.1438

[89]   Stellacci, F., C. A. Bauer,T. Meyer-Friedrichsen, W. Wenseleers, V. Alain, S. M. Kuebler, S. J. K. Pond, Y. Zhang, S. R. Marder, J. W. Perry. (2002) 3D free-standing and embedded metallic structures. *Adv. Mater*. Vol.14, pp.194

[90]   Kaneko, K., Sun H.-B., Kawata, S. (2003) Two-photon photoreduction of metallic nanoparticle gratings in a polymer matrix. *Appl. Phys. Letter*. Vol.83, pp.1426

[91]   Baldacchini, T., Pons, A., Pons, J., LaFratta, C., Fourkas, J., Sun, Y., Naughton, M. (2005) Multiphoton laser direct writing of two-dimensional silver structures. *Opt. Express*. Vol.13, pp1275

[92]   LaFratta, C., Lim, D., O'Malley, K., Baldacchini, T., Fourkas, J. (2006) Direct Laser Patterning of Conductive Wires on 3-D Polymeric Microstructures. *Chem. Mater*.Vol.18, pp.2038

[93]   Formanek, F., Takeyasu, N., Tanaka, T., Chiyoda, K., Ishikawa, A., Kawata, S. (2006) Three-dimensional fabrication of metallic nanostructures over large areas by two-photon polymerization. *Opt. Express*. Vol.14, pp.800

[94] Ishikawa, A., Tanaka, T., Kawata, S. (2006) Improvement in the reduction of silver ions in aqueous solution using two-photon sensitive dye. *Appl. Phys. Letter*. Vol.89, 113102

[95] Formanek, F., Takeyasu, N., Tanaka, T., Chiyoda, K., Ishikawa, A., Kawata, S. (2006) Selective electroless plating to fabricate complex three-dimensional metallic micro/nanostructures. *Appl. Phys. Letter*. Vol.88, 083110

[96] Farrer, R. A., LaFratta, C., LiL., Praino, J., Naughton, M., Saleh, B., Teich, M., Fourkas, J. (2006) Selective Functionalization of 3-D Polymer Microstructures. *J. Am. Chem. Soc*. Vol.128, pp.1796

[97] Chen, Y., Tal, A., Torrance, D., Kuebler, S. (2006) Fabrication and characterization of three-dimensional silver-coated polymeric microstructures. *Adv. Funct. Mater*. Vol.16, pp.1739

[98] Campbell, M., Sharp, D., Harrison, M., Denning, R., Turberfield, A, (2000) Fabrication of photonic crystals for the visible spectrum by holographic lithography. *Nature*. Vol.404, pp.53

[99] Shoji, S., Kawata, S. (2000) Photofabrication of three-dimensional photonic crystals by multibeam laser interference into a photopolymerizable resin. *Appl. Phys. Letter*. Vol.76, pp.2668

[100] Shoji, S., Zaccaria, R., Sun, H., Kawata, S. (2006) Multi-step multi-beam laser interference patterning of three-dimensional photonic lattices. *Opt. Express* Vol.14, pp.2309

[101] Jeon, S., Menard, J.-U. Park, J. Maria, M. Meitl, J. Zaumseil, and J. A. Rogers. (2004) Three-dimensional nanofabrication with rubber stamps and conformable photomasks. *Adv. Mater*. Vol.16, pp.1369

[102] Jeon, S., J.-U. Park, R. Cirelli, S. Yang, C. E. Heitzman, P. V. Braun, P. J. A. Kenis, and J. A. Rogers. (2004) Fabricating complex three-dimensional nanostructures with high-resolution conformable phase masks. *Proc. Natl. Acad. Sci.* USA. Vol.101, 12428

[103] Jeon, S., Malyarchuk, V., Rogers, J., Wiederrecht, G. (2006) Fabricating three-dimensional nanostructures using two photon lithography in a single exposure step. *Opt. Express.*Vol.14, pp.2300

[104] Kato, J.-I., Takeyasu, N., Adachi, Y., Sun, H., Kawata, S. (2005) Multiple-spot parallel processing for laser micronanofabrication. *Appl. Phys. Letter.* Vol.86, 044102.

[105] LaFratta, C., Baldacchini, T., Farrer, R., Fourkas, J. (2004) Replication of Two-Photon-Polymerized Structures with Extremely High Aspect Ratios and Large Overhangs. *J. Phys. Chem. B*. Vol.108, 11256.

[106] Xia, Y., Whitesides, G. M. (1998) Soft lithography. *Angew. Chem. Int. Ed*. Vol37, pp.550

[107] LaFratta, C., Li L., Fourkas, J. (2006) Soft-lithographic replication of 3D microstructures with closed loops. *Proc. Natl. Acad. Sci. USA*. Vol.103, 8589

[108] Pal, R., Yang, M., Lin, R., Johnson, BN., Srivastava, N., Razzacki, SZ., Chomistek, KJ., Heldsinger, DC., Haque, RM., Ugaz, VM., Thwar, PK., Chen, Z., Alfano, K., Yim, MB., Krishnan, M., Fuller, AO., Larson, RG., Burke, DT., Burns, MA (2005) An integrated microfluidic device for influenza and other genetic analyses. *Lab Chip Miniaturisation Chem Biol.* Vol.5. 10, pp.1024-1032.

[109] Shah, L., Arai, A.Y., Eaton, S.M., Herman, P.R. (2005) Waveguide writing in fused silica with a femtosecond fiber laser at 522 nm and 1 MHz repetition rate. *Opt. Express*. Vol.13. 6, pp.1999-2006.

[110] Liu, X., Du, D., Mourou, G. (1997) Laser ablation and micromachining with ultrashort laser pulses. *IEEE J Quantum Electron.* Vol.33. 10, pp.1706-1716.

[111] Venkatakrishnan, K., Tan, B. (2002) Femtosecond pulsed laser direct writing system. *Opt Eng.* Vol.41. 6, pp.1441-1445.

[112] Simon, G., Grotzke, U., Kross, J. (1993) Analysis of heat conduction in deep penetration welding with a time-modulated laser beam. *J Phys D: Appl Phys* Vol.26, pp.862.

[113] Holma, J. (1986) Heat Transfer. 6th edition. *McGraw-Hill*, New York.

[114] Reddy, J., Gartling, D. (2000) The Finite Element Method in Heat Transfer and Fluid Dynamics. *CRC Press,* London.

[115] Fischer, P., Locher, M., Romano, V., Weber, H.-P., Kolossov, S., Glardon, R. (2004) Temperature measurements during selective laser sintering of titanium powder. *International Journal of Machine Tools and Manufacture.* Vol.44, pp.1293.

[116] Kolossov, S., Boillat, E., Glardon, R., Fischer, P., Locher, M. (2004) 3D FE simulation for temperature evolution in the selective laser sintering process. *International Journal of Machine Tools and Manufacture*. Vol.44, pp.117.

[117] Malian, P. (1993) Regulation of Flowering Time by Arabidopsis Photoreceptors. *J Mat Sci*. Vol. 28, pp.1738.

[118] P´erez del Pino, A., Serra, P., Morenza, J. (2002) Review about laser nitriding of titanium alloys. *Appl. Surf. Sci.* pp.197/198, 887.

[119] Roy, B., Ahrenkiel, S., Fuierer, P. (2008) Controlling the Size and Morphology of TiO2 Powder by Molten and Solid Salt Synthesis. *J. Am. Ceram. Soc.* Vol.91, pp.2455.

[120] Mazza, T., Barborini, E., Piseri, P., Milani, P., Cattaneo, D., Bassi, A., Bottani, C., Ducati c. (2007) Raman spectroscopy characterization of TiO_2 rutile nanocrystals. *Phys. Rev. B*. Vol.75, 045416.

[121] Venkatakrishnan, k., Tan, B., Stanley, P., Lim, L., Ngoi, B. (2002) Laser writing techniques for photomask fabrication using a femtosecond laser. *Opt. Eng*. Vol.41, pp.1441.

[122] Tan, B., Venkatakrishnan, K. (2009) Synthesis of fibrous nanoparticle aggregates by femtosecond laser ablation in air. *Opt Express*. Vol.17 (2), pp.1064.

[123] Jee, Y., Becker, M., Walser, R. (1988) Laser-induced damage on single-crystal metal surfaces. *J Opt Soc Am B*. Vol.5 (3) pp.648.

[124] Colchero, J., Luna, M., Baro, A. (1996) Lock-in technique for measuring friction on a nanometer scale. *Appl Phys Letter*. Vol.68 (20), pp.2896.

[125] Xu, H., Zhai, J. (2001) Energy-filtering TEM imaging of ZrB2/SiC composite – an ultrahigh temperature ceramic for thermal protection. *Microscopy and Microanalysis*. Vol.7 (S2), pp.262-263..

[126] Bulgakova, N., Bourakov, J. (2002) Phase explosion under ultrashort pulsed laser ablation: modeling with analysis of metastable state of melt. *Appl Surf Sci*. Vol.41. pp.197-198.

[127] Eidmann, K., Meyer-ter-Vehn, J., Schlegel, T., Huller, S. (2000) Hydrodynamic simulation of subpicosecond laser interaction with solid-density matter. *Phys Rev E*. Vol.62, pp.1202.

[128] Patil, R., Yadava, V. (2007) Finite element analysis of temperature distribution in single metallic powder layer during metal laser sintering. *Int J of Machine Tools & Manufacture*. Vol.47, pp.1069.

[129] Cui, B., Wu, L., Chou, S. (2008) Fabrication of high aspect ratio metal nanotips by nanosecond pulse laser melting. *Nanotechnology.* Vol.19 (34), 345303.

[130] Venkatakrishnan, K., Stanley, P., Sivakumar, N., Tan, B., Lim, L. (2003) Effect of scanning resolution and fluence fluctuation on femtosecond laser ablation of thin films. *Applied Physics A: Materials Science & Processing.* Vol.77(5), pp.655.

[131] Preuss, S., Demchuk, A., Stuke, M. (1995) Sub-picosecond UV laser ablation of metals. *Appl. Phys.* A Vol.61(1), pp.33.

[132] Bonse, J., Rudolph, P., Krueger, J., Baudach, S., Kautek, W. (2000) Ultrafast thin-film laser-induced breakdown spectroscopy of doped oxides. *Appl Surf Sci*.Vol.659 pp.154–155,

[133] Denney, D. 1982 Dictionary of spectroscopy. New York : *Wiley.*

[134] Odian, G. (1981) Principles of Polymerization. New York : *J.Wiley & Sons*.

[135] Yu, A., Akimov, K., Ostrikov, E., Li, P. (2009) Surface Plasmon Enhancement of Optical Absorption in Thin-Film Silicon Solar Cells. *Plasmonics* Vol.4, pp.107–113

[136] Bohren, F., Donald, H. (1998) Title Absorption and scattering of light by small particles. New York , *Wiley*

[137] Johnson, P., Christy, R. (1972) Optical Constants of the Noble Metals. *Phys. Rev. B.* Vol.6(12), pp.4370-4379.

[138] Alubaidy, M., Venkatakrishnan, K., and Tan, B (2010) Fabrication of a reinforced polymer microstructure using femtosecond laser material processing. *J. Micromech. Microeng.* Vol.20.

[139] Serbin, J., Egbert, A., Ostendorf, A., Chichkov, B .N., Houbertz, R., Domann, G., Schulz, J., Cronauer, J., Frohlich, L., Popall, M. (2003) Femtosecond laser-induced two-photon polymerization of inorganic organic hybrid materials for applications in photonics. *Opt. Letters*. Vol.28 pp.301.

[140] Song, J., Inoue, T., Kawazumi, H., Ogawa, T. (1999) Determination of Two Photon Absorption Cross Section of Fluorescein Using a Mode Locked Titanium Sapphire Laser. *Analytical Sciences*, Vol. 15(6), pp.601.

[141] Lakowicz, J. (2006) Principles of Fluorescence Spectroscopy. New York *: Springer.*

[142] Bass, M. (1994) Handbook of Optics. New York : *McGraw-Hill*.

[143] Alubaidy, M., Venkatakrishnan, K., Tan, B. (2011).On the formation of Titanium/Titanium oxide nanofibrous structures and nanoshperes using femtosecond laser in air. *Nano*. Vol.6(2), pp.123-130.

[144] Chang, C., Mar, A., Tiefenthaler, A., Wostratzk, D. (1992) Handbook of Coatings Additives. New York : *Marcel Dekker Inc*.

[145] Odian, G. (1981) Principles of Polymerization. New York : *J.Wiley & Sons*.

[146] Denney, D. (1982) Dictionary of spectroscopy. New York *: Wiley*.

[147] Lakowicz, J. (2006) Principles of Fluorescence Spectroscopy. New York : *Springer*.

[148] Bass, M. (1994) Handbook of Optics. New York *: McGraw-Hill*.

[149] Alubaidy, M., Venkatakrishnan, K., Tan, B. (2011) On the formation of Titanium/Titanium oxide nanofibrous structures and nanoshperes using femtosecond laser in air. *Nano*. Vol.6(2), pp.123-130

[150] Gu, B., Ji, W. (2008) Two-step four-photon absorption. *Optics Express*. Vol.16, 10208-10213.

[151] Sutherland, L., Brant, M., Heinrichs, J., Rogers, J., Slagle, J., McLean, D., Fleitz, P. (2005) Excited-state characterization and effective three-photon absorption model of two-photon-induced excited-state absorption in organic push–pull charge-transfer chromophores. *Opt. Soc. Am. B*. Vol.22, pp.1939-1948.

[152] Carusotto, S., Fornaca, G., Polacco, E. (1968) Multiphoton Absorption and Coherence. *Phys. Rev.,* Vol.165, pp.1391–1398.

[153] 149. Padon, K., Scranton, A. (2000) The Effect of Oxygen on the Three-Component Radical Photoinitiator System: Methylene Blue, NMethyldiethanolamine,and Diphenyliodonium Chloride. *Journal of Polymer Science Part A: Polymer Chemistry*. Vol.38, pp.3336–3346.

[154] Oliver, W., Pharr, G. (1992) technique for determining hardness and elastic modulus using load and displacement sensing indentation experiments. *J. Mater. Res.* Vol.7 pp:1564–1566.

[155] Tan, E., Lim, C. (2006) Mechanical characterization of nanofibers – A review. *Composites Science and Technology* Vol. 66, pp:1102–1111

[156] International Organisation for Standarisation (2001) ISO 14577-1.2: 1–27.

[157] Doraiswamy, A., Jin, Narayan R., Mageswaran, P., Mente, P., Modi, R., Auyeung R., Chrisey, D., Ovsianikov, A., Chichkov, B. (2006) Two photon induced polymerization of

organic–inorganichybrid biomaterials for microstructured medical devices, *Acta Biomaterialia* Vol. 2, pp: 267–275.

[158] Bhushan, B., Li, X. (1997) Micromechanical and tribological characterization of doped single-crystal silicon and polysilicon films for microelectromechanical systems devices. *Journal of Materials Research* Vol. 12 (1), pp: 54-63.

[159] Mallick, P. (1993) Fiber-reinforced composites: materials, manufacturing, and design, M. Dekker, New York.

[160] Cadek, M., Coleman, J., Barron, V., Hedicke, K., and Blau, W. (2002) Morphological and mechanical properties of carbon-nanotube-reinforced semicrystalline and amorphous polymer composites. *Appl. Phys. Lett.* Vol. 81: 1523.

[161] Starr, F., Schrode, T., Glotzer, S. (2002) Molecular Dynamics Simulation of a Polymer Melt with a Nanoscopic Particle. *Macromolecules* Vol: 35, pp:4481-4492.

[162] Smith, G., Bedrov, D., Li, L., and Byutner, O. (2002) A molecular dynamics simulation study of the viscoelastic properties of polymer nanocomposites. *J. Chem. Phys.* Vol. 117, pp: 9478-9490.

[163] György, I. (2008) Conducting Polymers *Springer,* Berlin, Heidelberg.

[164] Bethune, D.S., Kiang, C.H., de Vries, M.S., Gorman, G., Savoy, R., Vazquez, J., and Beyers, R., (1993) Cobalt-catalysed growth of carbon nanotubes with single-atomic-layer walls *Nature* Vol. 363(6430), pp: 605–607.

[165] Hou, Y.H., Zhang, M.Q., and Rong, M.Zh. (2003), Performance stabilization of conductive polymer composites *J. Appl. Polym. Sci.* 89, pp: 2438-2445.

[166] Chekanov, Y., Ohnogi, R., Asai, S., and Sumita, M. (1999) Electrical properties of epoxy resin filled with carbon fibers *J. Mater. Sci.* Vol. 34, pp:,5589-5592.

[167] Tan, B., and Venkatakrishnan, K. (2009) Synthesis of fibrous nanoparticle aggregates by femtosecond laser ablation in air *Opt. Express* Vol. 17(2), pp; 1064–1069.

[168] Tuinstra, F., and Koenig, J.L. (1970) Raman Spectrum of Graphite *J. Chem. Phys.* Vol. 53(1970), pp: 1126-1131.

[169] Chieu, T.C., Dresselhaus, M.S., and Endo, M. (1982) Raman studies of benzene-derived graphite fibers *Phys. Rev.* B Vol. 26, pp: 5867-5877.

[170] Alubaidy, M., Venkatakrishnan, k., and Tan, B, (2010) Fabrication of reinforced polymer microstructure using femtosecond laser material processing *J. Micromech. Microeng.* Vol. 20, pp: 55012-55017.

[171] Mahmood, A., Sivakumar, M., Venkatakrishnan, K., and Tan, B. (2009) Enhancement in optical absorption of silicon fibrous nanostructure produced using femtosecond laser ablation *Applied physics letters* Vol. 95 pp: 34107-3.

[172] Sheng, P., Sichel, E.K., and Gittleman, J.I. (1978)Fluctuation-Induced Tunneling Conduction in Carbon-Polyvinylchloride Composites *Phys. Rev. Lett.*, Vol. 40, pp: 1197-1200.

[173] Kodama, R.H., A.E. Berkowitz, E. J. McNiff, Jr., S. Foner. (1996) Surface spin disorder in NiFe2O4 nanoparticles. *Physical Review Letters* Vol. 77, pp: 394-397.

[174] Kruus, P., M. O'Neill, D. Robertson. (1990) Ultrasonic initiation of polymerization *Ultrasonics* Vol. 28 (5), pp: 304-309.

[175] Lee, G.J., S.H. Lee, K.S., Ahn, K.H. Kim (2002) Synthesis and characterization of soluble polypyrrole with improved electrical conductivity. *Journal of Applied Polymer Science* Vol. 84 (14), pp: 2583-2590.

[176] Li, J.R., J.R., Xu, M.Q., Zhang, M.Z. Rong. (2003) Carbon black/ polystyrene composites as candidates for gas sensing materials. *Carbon* Vol. 41, pp: 2353-2360.

[177] Li, J.X., M., Silverstein, A. Hiltner, E. Baer. (1994) The ductile-to-quasi-brittle transition of particulate-filled thermoplastic polyester *Journal of Applied Polymer Science* Vol. 52 (2), pp: 255-267.

[178] Loshaek, S. (1955) Crosslinked polymers. II. Glass temperatures of copolymers of methyl methacrylate and glycol dimethacrylates *Polymer Science* Vol. 15, pp: 391–404.

[179] Matyjaszewski, K. (1996) Cationic Polymerizations: Mechanisms, Synthesis, and Applications. *Marcel Dekker, Inc.* New York,

[180] Moskowitz, B.M., Hitchhiker's Guide to magnetism .http://www.geo.umn.edu/orgs/irm/hg2m/hg2m_index.html

[181] Murphy, O.J., G.D., Hitchens, D., Hodko, E.T., Clarke, D.L., Miller, D.L., Parker. (1999) Method of manufacturing passive elements using conductive polypyrrole formulations. *U.S. Patent*: 5,855,755 by Lynntech, Inc.

[182] Nayfeh, M., M. Brussel. (1985) Electricity and Magnetism *John Wiley & Sons, Inc.* New York.

[183] Nam, J.D., H.R. Choi, Y.S., Tak, K.J., Kim(2003) Novel electroactive, silicate nanocompoosites prepared to be used as actuators and artificial muscles *Sensors and Actuators A* Vol. 105, pp:83-90.

[184] Orefice, R.L., J.A.C. Discacciati, A.D., Neves, H.S., Mansur, W.C., Jansen. (2003) In situ evaluation of the polymerization kinetics and corresponding evolution of the mechanical properties of dental composites *Polymer Testing* Vol. 22, pp: 77-81.

[185] O'Rourke Muisener, P.A., L. Clayton, J. D'Angelo, J.P. Harmon, A.K. Sikder, A. Kumar, A.M. Cassell, B. Chen, M (2002) Meyyappan. Effects of gamma radiation on poly(methyl methacrylate)/single-wall nanotube composites *Journal of Materials Research* Vol. 17 (10), pp: 2507-2513.

[186] Park, C., Z.Ounaies, K.A. Watson, R.E. Crooks, J. Smith Jr., S.E. Lowther, J.W. Connell, E.J. Siochi, J.S. Harrison, T.L. St. Clair. (2002) Dispersion of single wall carbon nanotubes by in situ polymerization under sonication *Chemical Physics Letters* Vol. 364, pp: 303-308.

[187] Patnode, W., W.J. Scheiber. (1939) The density, thermal expansion, vapor pressure, and refractive index of styrene, and the density and thermal expansion of polystyrene *Journal of the American Chemical Society* Vol. 61, pp: 3449-3451.

[188] Poddar, P., J. L. Wilson, H. Srikanth, S. A. Morrison, and E. E. Carpenter. (2004)Magnetic properties of conducting polymer doped with manganese zinc ferrite nanoparticles. *Nanotechnology* Vol 10, pp: 1323-1344.

[189] Ramakrishna, S., J. Mayer, E. Wintermantel, K.W. Leing. (2001) Biomedical applications of polymer-composite materials: a review. *Composites Science and Technology* Vol. 61, pp: 1189-1224.

[190] Reding, F.P., J.A. Faucher, R.D. Whitman. (1962) Glass transitions in ethylene copolymers and vinyl homopolymers and copolymers *Journal of Polymer Science* Vol. 57 (165), pp: 483-498.

[191] Wilson, J.L., P. Poddar, N.A. Frey, H. Srikanth, K. Mohomed, J.P. Harmon, S. Kotha, J. Wachsmuth. (2004) Synthesis and magnetic properties of polymer nanocomposites with embedded iron nanoparticles *Journal of Applied Physics* Vol. 95 (3), pp: 1439-1443.

[192] Nuzzo, R., Allara, D. (1983) Adsorption of bifunctional organic disulfides on gold surfaces *J. Am. Chem.* Soc., vol. 105, pp. 4481-4483..

[193] Taft, B., O'Keefe, M., Fourkas, J., Kelley, S. (2003) Engineering DNA-electrode connectivities: manipulation of linker length and structure *Anal. Chim. Acta,* vol. 496, pp. 81-91.

[194] Liu, G., Wan, Y., Gau, V., Zhang, J., Wang, L., Song, S., Fan, C. (2008) An Enzyme-Based E-DNA Sensor for Sequence-Specific Detection of Femtomolar DNA Targets. *J. Am. Chem. Soc.* 130, 6820–6825.

[195] Lapierre, M., O'Keefe, M., Taft, B., Kelley, S. (2003) Electrocatalytic Detection of Pathogenic DNA Sequences and Antibiotic Resistance Markers. *Anal. Chem.* 75, pp: 6327-6333.

[196] Li, F., Han, X., Liu, S. (2011) Development of an electrochemical DNA biosensor with a high sensitivity of fM by dendritic gold nanostructure modified electrode. *Biosensors and Bioelectronics* 26(5), pp: 2619-2625.

146